Experimental Validation of Lattice Boltzmann Method for Prediction of Strut Braced Wing Aeroacoustics

Mustafa Sabri Güverte

Delft University of Technology

TU Delft

Experimental Validation of Lattice Boltzmann Method for Prediction of Strut Braced Wing Aeroacoustics

by

Mustafa Sabri Güverte

To be defended publicly on Wednesday, November 20th, 2024 at 10:00
for the degree of Master of Science
at the Delft University of Technology

Thesis Supervisors:	F. de Prenter
	E. Sticchi
Thesis Committee:	F. de Prenter
	A. Sciacchitano
	R. Schmehl
Project Duration:	November, 2023 - November, 2024
Faculty:	Faculty of Aerospace Engineering, Delft

TU Delft

Summary

Strut-braced wings have recently garnered renewed interest in the aerospace industry due to their potential to improve aerodynamic efficiency and reduce structural weight. However, current Computational Fluid Dynamics (CFD) software tools face significant challenges in accurately predicting the unsteady flow phenomena associated with such designs, particularly in junction flow dynamics. This thesis aims to validate the capabilities of a Lattice Boltzmann Method (LBM) solver in predicting both the aerodynamic and aeroacoustic features of a model strut-braced wing. To achieve this, a series of wind tunnel tests were conducted to provide experimental data for comparison with the CFD results. Results showed partial agreement between numerical and experimental steady measurements. The numerical solver could predict correct surface pressure distributions for the wing pressure side and a correct pressure coefficient was attainable for an adjusted angles of attack. Furthermore, the numerical method matched wake rake results to a high degree. However, the CFD transitional model was less sensitive to the transition strips, unable to transition the boundary layer at the location of the transition trips when in the wind tunnel, the trips successfully transitioned the boundary layer. The numerical model struggled to capture the unsteady phenomena due to the junction flow at the strut wing intersection. Unsteady pressure measurements showed that the LBM solver overpredicted surface pressure fluctuations near the junction region, affecting the accuracy of the acoustic analogy employed by the CFD software and, ultimately, misrepresenting the junction as the primary acoustic noise source. As such, the solver in question struggles to accurately predict the noise of a strut-braced wing. Moreover, further investigation must be done to improve the wind tunnel anechoic performance, as the tunnel diffusor and test section were identified as the dominant noise sources, thus hindering the analysis.

Contents

List of Figures

Nomenclature

Abbreviations

Abbreviation	Definition
CFD	Computational Fluid Dynamics
FW-H	Ffowcs William Hawkings
IR	Infrared Thermography
LES	Large Eddy Simulation
LIC	Line Integral Convolution
LBM	Lattice Boltzmann Method
LTT	Low-Turbulence Tunnel
PSD	Power Spectral Density
RANS	Reynolds Averaged Navier Stokes
RDP	Raymer Douglas Peucker
SPL	Sound Pressure Level
URANS	Unsteady Reynolds Averaged Navier Stokes
VLES	Very Large Eddy Simulation

Symbols

Symbol	Definition	Unit
BF	Bluntness Factor	[-]
MDF	Momentum Deficit Factor	
R_o	Leading Edge Radius	[m]
T	Maximum Thickness	[m]
V	Velocity	[m/s]
X_T	Chordwise location of maximum thickness	[m]
α	Angle of Attack	[°]
ρ	Density	[kg/m^3]

1

Introduction

The European Union's 2050 climate neutrality target is a significant call for change in the aviation industry. This overarching goal underscores the critical need for sustainable practices across various sectors, placing the European aviation industry under the spotlight. To that, the HERWINGT project is a European Union-supported initiative to develop a Hybrid Electric Regional aircraft which plays a role in this mission. This aircraft, designed to accommodate up to 100 passengers and operate within a range of 500 to 1000 kilometres, is a significant step towards achieving this goal.

Achieving these ambitious goals necessitates reconsidering conventional aircraft design, particularly in developing aerodynamically efficient structures. One such design innovation is incorporating higher aspect ratio wings, which are critical for enhancing aerodynamic performance. However, these wings require additional support, which, in the case of HERWINGT is provided by supporting struts, leading to a strut-braced wing configuration.

However, as climate pollution is a significant industry concern, so is the impact of noise pollution. To that effect, the understanding of noise due to wing junctions needs to be better understood, and the ability to model them in Computational Fluid Dynamics (CFD) solvers has not been extensively validated. Therefore, this thesis centres on junction flow, the aerodynamic phenomenon associated with the strut-braced wing design and a topic that is still being researched. Junction flow occurs when a boundary layer interacts with protruding surfaces, such as the intersection between the strut and the wing in the HERWINGT design. Therefore, understanding the impact of junction flow is vital for optimising the design of the hybrid aircraft.

1.1. Thesis Objective

The primary objective of this thesis is to validate the efficacy of a Lattice Boltzmann Method (LBM) CFD solver in predicting the flow characteristics of a strut-braced wing. Prior research, such as the work by Ding et al. [12], has highlighted the limitations of traditional Reynolds-Averaged Navier-Stokes (RANS) models in accurately predicting the transient behaviour of aerodynamic flows.

Moreover, conventional RANS and Unsteady RANS (URANS) models must be reconsidered in simulating the acoustics of complex wing configurations. These models generally struggle to capture the fluctuating flow patterns responsible for noise generation, which is critical in assessing an aircraft's aeroacoustic performance [26]. The pressure fluctuations that generate noise are significantly smaller than those influencing aerodynamic performance [44]. Such simulations require highly refined computational meshes and large domains, resulting in substantial computational resources.

LBM solvers emerge as an alternative to traditional Navier-Stokes solvers. Their more straightforward parallelisation capabilities, low dissipativity and dispersivity [41] make them more suitable for deploying high-performance computer clusters and propagating sound waves over large distances. This thesis will focus on assessing the PowerFLOW LBM solver's ability to accurately predict the junction flow and its implications for the aerodynamic and aeroacoustic performance of the strut-braced wing.

2

Background Information

In this chapter, several pertinent topics will be introduced. First, context will be provided on the junction flow phenomena, including its governing parameters. Following this, the framework for the Ffowcs-Williams and Hawkings (FW-H) analogy, which will serve as a tool for the acoustic analysis, will be discussed. Additionally, an overview of the LBM model will be provided, along with justification for its application in this context. Finally, the wind tunnel methodologies relevant to the study will be briefly outlined, offering insight into the validation techniques employed.

2.1. Junction Flow Phenomena

Junction flows occur when a boundary layer encounters an obstacle attached to the same surface. Due to the adverse pressure gradient in the streamwise direction produced by the presence of the obstacle, a roll up of the incoming fluid occurs which creates multiple horseshoe vortices just upstream of the junction [25]. These horseshoe vortices come in the form of a single primary vortex that shares the same vorticity direction as the boundary layer, and multiple smaller secondary horseshoe vortices, which have opposing vorticity directions (as presented in Figure 2.1) [45].

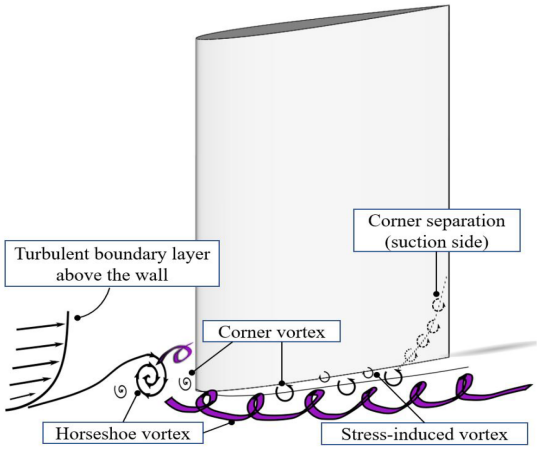

Figure 2.1: Flow-field of rood wing junction flow, showing primary horseshoe vortex and opposing secondary vortices [21]

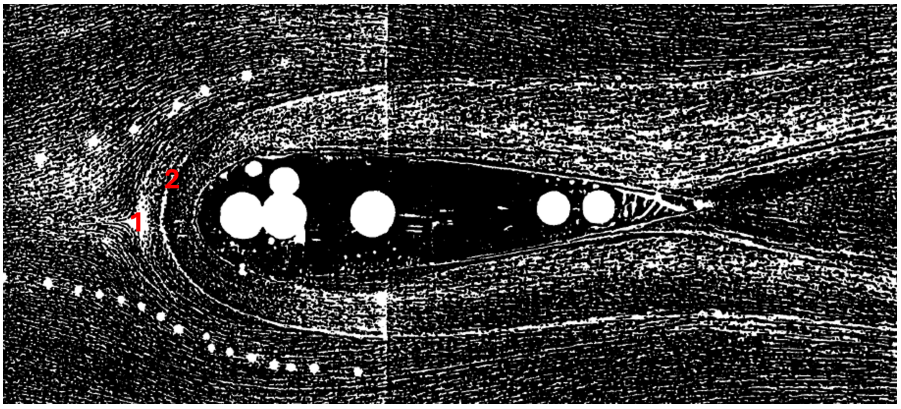

Figure 2.2: Oil flow visualisation of leading edge Horseshoe Vortex region, 1 designates the saddle point, 2 designations the transition line from the region of low shear stress to the region of high shear stress (close to the wing walls)[33]

Figure 2.2 Shows how as the incoming flow approaches the junction obstacle, a saddle point occurs which is where the Horseshoe Vortex is created, furthermore, one can see the region is separated into a low and high shear stress region which the streamlines are able to cross.

Finally, another phenomena associated with junction flow are that corner vortices are present in the region between the leading edge corner and the horseshoe vortex, whose growth is related to the growth of the wing boundary layer [28]. These vortices are not steady, and they stretch, diffuse, and merge to form new vortices as they travel downstream [38]. [17] identified this separation is associated with the incoming boundary layer and the strength of the leading edge horseshoe vortex. Barber found that the separation area is inversely proportional to the strength of the primary horseshoe vortex and Reynolds number [17].

2.1.1. Parameters Influencing Junction Flow

Understanding the sensitivities of various junction flow phenomena when changing various aerodynamic parameters is essential. As such, the main parameters affecting the formation of junction flow are presented.

Airfoil Bluntness

Simpson collated that the bluntness of an airfoil influenced the mean vortex size and strength [45]. As such, the bluntness factor is introduced as the following:

$$BF = \frac{1}{2}\frac{R_o}{X_T}\left(\frac{T}{S_T} + \frac{S_T}{X_T}\right) \tag{2.1}$$

Where R_o is the leading edge radius, T is the maximum thickness, and X_T is the chord-wise location of the maximum thickness. S_T is the distance from the leading edge along the airfoil surface to the location of maximum thickness. It is later shown that increasing the bluntness factor increases the size and strength of the vortices [45][11]; furthermore, the vortex stretching rate can be described by the BF by the following equation:

$$VS = 10^b * (BF)^m \tag{2.2}$$

The values for the parameters b and m are set for specific angle of attack cases [21].

Reynolds Number and Momentum Deficit Factor

[14] discussed a subsequent influential factor on the strength of the horseshoe vortex: the Momentum Deficit Factor (MDF). This parameter, defined as $MDF_x = Re_T \times Re_{\theta_x}$, incorporates the effects of the oncoming boundary layer on the resulting junction flow. Here, Re_T represents the Reynolds number based on the maximum wing thickness, and Re_{θ_x} is the Reynolds number based on the undisturbed boundary layer momentum thickness.

A discernible trend was observed: an increasing value of MDF corresponds to a heightened strength in the horseshoe vortex [11]. Furthermore, larger MDF values brought the vortex cores closer to the junction surface.

2.1.2. Junction Flow Noise

Multiple studies have looked into noise induced by junction flow. Their findings revealed that junction noise emerges as a significant source in the context of aircraft wing noise, with some studies stating it as the dominating low-frequency broadband source. Notably, junction noise takes precedence within the frequency range of 2–13 kHz, and a Strouhal number range of 2.8–18.2 (depending on the angle of attack), being particularly dominant below 4 kHz [11]. The junction noise originates from the junction leading edge, with its magnitude depending primarily on its bluntness factor [21].

Furthermore, the influence of airfoil profiles was tested. Among those, the NACA 0012 profile stands out as a notable case, where junction noise emerges as a significant source across most of the frequency spectrum, which was not the case for the other airfoil shapes [11], giving further insight to the potential effects of the BF of a junction in its noise spectra.

Regarding sensitivities for the noise source, [11] finds that the noise source at the mid-chord position of the junction (where the corner vortex lies) remains relatively unchanged regardless of Reynolds number variations. However, for the noise source at the leading edge-wall junction, the strength of this noise source increases with higher Reynolds numbers. Moreover, for variations in angle of attack, sound maps for the NACA 0012 wing consistently identify the leading-edge junction as a dominant noise source across all angles of attack [11].

Though junction flow noise has been attributed as a major noise source, a key limitation in most of these studies are that they are testing rood wing geometries which do not accurately reflect a strut-braced wing. As such further research needs to be performed to compare the junction noise with other noise sources such as the wing trailing edge noise.

2.2. Acoustic Analogies

2.2.1. FW-H Equation

The Ffowcs-Williams & Hawking equation (FW-H) is the most general form of Lighthill's acoustic analogy [20] and the method that PowerFLOW will use to analyse the sounds emitted by the strut-braced wing. The differential expression for the FW-H equation is presented as:

$$\Box^2 \left[(\rho - \rho_0)\, c^2 H(f) \right] = \frac{\partial^2}{\partial x_i \partial x_j} \left[T_{ij} H(f) \right] - \frac{\partial}{\partial x_i} \left[V \delta(f) \right] + \frac{\partial}{\partial t} [Q \delta(f)] \tag{2.3}$$

With the wave operator defined as:

$$\Box^2 = \left(\frac{1}{\mathrm{c}^2} \frac{\partial^2}{\partial \mathrm{t}^2} - \nabla^2 \right) \tag{2.4}$$

Where Lighthill's stress tensor $\mathrm{T_{ij}}$ is defined as:

$$\mathrm{T_{ij}} = \rho \mathrm{u_i u_j} + \left(\mathrm{p'} - \mathrm{c}^2 \rho' \right) \delta_{\mathrm{ij}} - \tau_{\mathrm{ij}} \tag{2.5}$$

Looking back at the FW-H equation 2.3, one sees three differential terms on the right-hand side. The first term is a quadrupole source term (which accounts for flow non-linearities in the fluid domain, such as shock waves or highly turbulent wakes that produce noise). The second term represents the loading source (dipole) term, which accounts for an unsteady loading exerted by a body on a fluid. The final thickness source (monopole) term accounts for the displacement in the fluid by the body in motion. The loading source term and the thickness source term are distributed over the wing's surface, whereas the quadrupole source term is distributed over a volume. The combination of the sources provides a complete description of the noise a given domain produces. Within the context of junction flow, due to the low Mach numbers that will be tested and the lack of moving parts of the junction (like a propeller

blade), the only noise source that is expected are the dipoles produced by the unsteady loading source terms, therefore only the wing and strut surface will be sampled.

2.2.2. Solving the PDE & Green's Function

Recalling the rearranged wave equation

$$\Box^2 \left[(\rho - \rho_0) c^2 H(f) \right] = \frac{\partial^2}{\partial x_i \partial x_j} \left[T_{ij} H(f) \right] - \frac{\partial}{\partial x_i} \left[V \delta(f) \right] + \frac{\partial}{\partial t} [Q \delta(f)] = f(x) \tag{2.6}$$

The Green's function can be employed to solve this PDE. To explain the Green's function, consider any inhomogeneous linear differential equation operator L being performed on a function $\Phi(x)$:

$$L[\Phi(x)] = f(x) \tag{2.7}$$

For any linear operator L there exists a function $G(x)$ such that

$$L[G(x)] = \delta(x) \tag{2.8}$$

Where $\delta(x)$ is a Dirac delta function. Once such a function is obtained. It is possible to obtain all solutions of $\Phi(x)$ by the following convolution:

$$\Phi(\mathbf{x}) = \int f(\mathbf{x}') G(\mathbf{x} - \mathbf{x}') \, \mathrm{d}^3 \mathbf{x}' \tag{2.9}$$

In the context of acoustic analogy, L is the wave operator $\Box^2$. Φ is $(\rho - \rho_0) c^2 H(f)$ and $f(x)$ are the noise source terms which are sampled during the simulations.

2.2.3. Solving the Wave Equation in Retarded Time

When considering using Green's function on the wave equation. A distinction must be made on whether the function is in the reference frame of the emitter or the observer. To that, retarded time is introduced as the reference frame of the listener and is selected as the reference frame.

For the wave equation, the Green's function G is given by:

$$G = \frac{\delta(\xi)}{r}$$

where δ is the Dirac delta function, and ξ is defined as:

$$\xi = t - \tau - \frac{r}{c}$$

In these equations:

- t is the time when the observer listens.
- τ is the time when the source emits the noise.
- r is the distance between the source and the observer.
- c is the speed of sound.

The term $t - \tau$ represents the elapsed time between the emission of the sound by the source and the observation of the sound by the listener. The term $\frac{r}{c}$ accounts for the time it takes for the sound to travel from the source to the observer.

2.2.4. Applying the Green's Function

The Green's function allows for the effective solving of the wave equation by accounting for the propagation of sound waves from the source to the observer. The advantage of using such a function is that it corrects for noise sources other than those originating from the geometry of interest. In this thesis, the wing is the primary noise source of interest; however, noise can also arise from reflections off the wind tunnel walls, even when lined with noise-absorbing materials. Therefore, formulating a correct Green's function for the wind tunnel would be beneficial in isolating the noise of the wing; however, as of the time of the thesis, a tailored Green function for the LTT has not been made yet, and thus, further necessitates the need for the acoustic lining of the test section. Ideally, one would use both the tailored Green's function and the acoustic lining in tandem to minimise sound sources from the LTT walls.

2.3. Lattice Boltzmann Method

2.3.1. Boltzmann Equation Derivation

In order to discuss the LBM model, it is essential to consider kinetic theory first. In the kinetic theory of gases, the state of a mono-atomic gas is described by using a probability distribution function $f_N(x, \xi, t)$ of gas particles at location x and time t moving with velocity ξ. This specific description is only valid for mono-atomic gases since no internal degrees of freedom are considered. Considering that all particles have the same mass, these distributions can be represented as:

$$f(\boldsymbol{x}, \boldsymbol{\xi}, t) = m f_N(\boldsymbol{x}, \boldsymbol{\xi}, t) \tag{2.10}$$

where m is the mass of the particles. Using this notation, it is possible to describe the density as [9]:

$$\rho(\boldsymbol{x}, t) = \int_{\mathbb{R}^D} f(\boldsymbol{x}, \boldsymbol{\xi}, t) \mathrm{d}\boldsymbol{\xi} \tag{2.11}$$

The momentum is as follows:

$$\rho \boldsymbol{u}(\boldsymbol{x}, t) = \int_{\mathbb{R}^D} \boldsymbol{\xi} f(\boldsymbol{x}, \boldsymbol{\xi}, t) \mathrm{d}\boldsymbol{\xi} \tag{2.12}$$

And the total energy as:

$$\rho E(\boldsymbol{x}, t) = \int_{\mathbb{R}^D} \frac{\xi^2}{2} f(\boldsymbol{x}, \boldsymbol{\xi}, t) \mathrm{d}\boldsymbol{\xi} \tag{2.13}$$

Furthermore, one can take the distribution function and differentiate it to get the following relation:

$$\frac{\mathrm{d}f}{\mathrm{d}t} = \left(\frac{\partial f}{\partial t}\right) \frac{\mathrm{d}t}{\mathrm{d}t} + \left(\frac{\partial f}{\partial x_\beta}\right) \frac{\mathrm{d}x_\beta}{\mathrm{d}t} + \left(\frac{\partial f}{\partial \xi_\beta}\right) \frac{\mathrm{d}\xi_\beta}{\mathrm{d}t} \tag{2.14}$$

Which presents the general form of the Boltzmann equation

$$\frac{\partial f}{\partial t} + \xi_\beta \frac{\partial f}{\partial x_\beta} + \frac{F_\beta}{\rho} \frac{\partial f}{\partial \xi_\beta} = \Omega(f) \tag{2.15}$$

The first two terms describe the advection of particles, while the third term represents the forces affecting the velocity ξ. The source term $\Omega(f)$ is called the collision operator, which is responsible for accounting for the effect of a collision between particles on the distribution function[9] [29].

2.3.2. Lattice Boltzmann Equation Differentiation

The Boltzmann equation, as it stands, does not lend itself to computational solving. However, a numerical scheme for the Boltzmann equation is achievable and more easily and efficiently parallelizable [9, 16]. This numerical scheme consists of a similar distribution function $f(x, t)$; however, the function is not continuous but discrete both temporally and spatially, usually in lattice units. By discretizing the Boltzmann equation, one arrives at the lattice Boltzmann equation as shown below;

$$f_i(\mathbf{x} + \mathbf{c}_i \delta t, t + \delta t) - f_i(\mathbf{x}, t) = -\frac{1}{\tau}[f_i(\mathbf{x}, t) - f_i^{\mathsf{eq}}(\mathbf{x}, t)] \tag{2.16}$$

Here, the variables are defined as follows:

$f_i(\mathbf{x}, t)$ is the distribution function for particle i at position $\mathbf{x}$ and time t.
$\mathbf{c}_i$ is the discrete velocity vector associated with particle i.
δt is the time step.
τ is the relaxation time, a parameter related to the fluid viscosity.
$f_i^{\text{eq}}(\mathbf{x}, t)$ is the equilibrium distribution function.

Again, the right hand side $-\frac{1}{\tau}[f_i(\mathbf{x}, t) - f_i^{\text{eq}}(\mathbf{x}, t)]$ term, represents the collision operator derived from the Bhatnagar-Gross-Krook (BGK) model [34].

With this, one can also interchange between lattice units and real units as follows [29]:

property	conversion
velocity	$u^{\text{real}} = \frac{\Delta x}{\Delta t} u^{\text{LB}}$
density	$\rho^{\text{real}} = \frac{\Delta m}{(\Delta x)^3} \rho^{\text{LB}}$
relaxation time	$\tau^{\text{real}} = \Delta t \tau^{\text{LB}}$
speed of sound	$a = \frac{\Delta x}{\Delta t} c_s$
viscosity	$\nu^{\text{real}} = \frac{(\Delta x)^2}{\Delta t} \nu^{\text{LB}}$
pressure	$P^{\text{real}} = \frac{\Delta m}{\Delta x (\Delta t)^2} P^{\text{LB}}$
force	$F^{\text{real}} = \frac{\Delta m \Delta x}{(\Delta t)^2} F^{\text{LB}}$

Eventually, the macroscopic flow properties can also be reconstructed from the following equations:

$$\rho(\boldsymbol{x}, t) = \int_{\mathbb{R}^D} f(\boldsymbol{x}, \boldsymbol{\xi}, t) \mathrm{d}\boldsymbol{\xi} = \sum_{i=0} f_i \tag{2.17}$$

$$\rho \boldsymbol{u}(\boldsymbol{x}, t) = \int_{\mathbb{R}^D} \boldsymbol{\xi} f(\boldsymbol{x}, \boldsymbol{\xi}, t) \mathrm{d}\boldsymbol{\xi} = \sum_{i=0} f_i \boldsymbol{\xi} \tag{2.18}$$

2.3.3. Benefits of LBM Solvers

The pressure fluctuations attributed to noise are smaller than those attributed to aerodynamics [44]. Furthermore, due to the long propagation distances required to perform far-field noise analysis, the numerical scheme must have lowly dispersive and dissipative characteristics [47] while being computationally efficient enough to handle the expensive grids needed to capture the noise.

LBM solvers are based on the Lattice Gas Automata; whereas conventional solvers use mesoscopic fluid values, LBM functions on the microscopic scale. As such, whereas ordinary NS solvers often require the Poisson equation for incompressible fluids, which require global fluid data [10], LBM solvers require data strictly from its neighbouring nodes with the most expensive calculations such as collision being computed locally, within each node [47]. This allows for easier parallel computing of LBM simulations as the entire domain can be divided into subdomains and calculated independently [9]. The implications of this are relevant to this thesis. In aeroacoustic simulations, LBM solvers can handle the large meshes needed for computational aeroacoustics efficiently, and are comparable in accuracy between second and third-order Navier Stokes simulations when it comes to dispersive and dissipative errors while running faster than their counterparts [41].

2.3.4. PowerFLOW & Turbulence Model

PowerFLOW, which will be used to perform the CFD simulations, utilizes the LBM for simulating fluid flow and incorporates the Very Large Eddy Simulation (VLES) approach for turbulence modelling.

In VLES and LES, turbulence scales are classified into large and small scales. Large scales consist of energy-containing eddies that significantly influence the overall flow field and are shown to be highly

dependent on the individual problem case. VLES aims to resolve these eddies directly to capture their phenomena accurately. On the other hand, small-scale eddies are responsible for energy dissipation and are typically not resolved due to their universal behavior and computational cost [37]. Instead, these small-scale eddies are modelled using subgrid-scale models that approximate their effects on the resolved scales. In the LBM-VLES approach used by PowerFLOW, the effect of the unresolved scale is accounted for by adjusting the relaxation time in the BGK collision term operator [4]. An effective turbulent relaxation time is calculated using a variant of the RNG κ-ϵ model developed by [51] as shown below:

$$\tau_{\text{eff}} = \tau + C_\mu \frac{\kappa^2/\epsilon}{\sqrt{1+\eta^2}} \tag{2.19}$$

κ is the turbulent kinetic energy and ϵ is the rate of dissipation of κ. C_μ is set as 0.09 and η are a combination of local strain, vorticity, and helicity, mitigating sub-grid scale viscosity in large resolved vortices [3]. Notice that, although the relaxation time is computed using a two-equation transport model, it is not used to compute an equivalent eddy viscosity or Reynolds stresses, as in RANS models, but rather to re-calibrate the Boltzmann model to the characteristic time scales of turbulent flow motion. This constitutes the essence of the LBM-VLES approach, which contrasts with Detached Eddy Simulations, where a RANS model is employed to approximate small structures, such as boundary layers near surface walls [30], while Large Eddy Simulations (LES) are applied elsewhere [46]. Finally, PowerFLOW utilizes a pressure-gradient-extended law-of-the-wall as presented by [48] to capture wall effects and flow separation.

2.4. TU Delft LTT Wind Tunnel

The Low-Turbulence Tunnel (LTT) facility at Delft University of Technology operates as a closed-circuit wind tunnel with a contraction ratio of 17.8. The maximum wind speed achievable is 120 m/s. The turbulence intensity within the test section exhibits a variation, starting at 0.02% when the wind speed is 10 m/s and increasing to 0.07% at 70 m/s [49]. The tunnel layout is illustrated in figure 2.3.

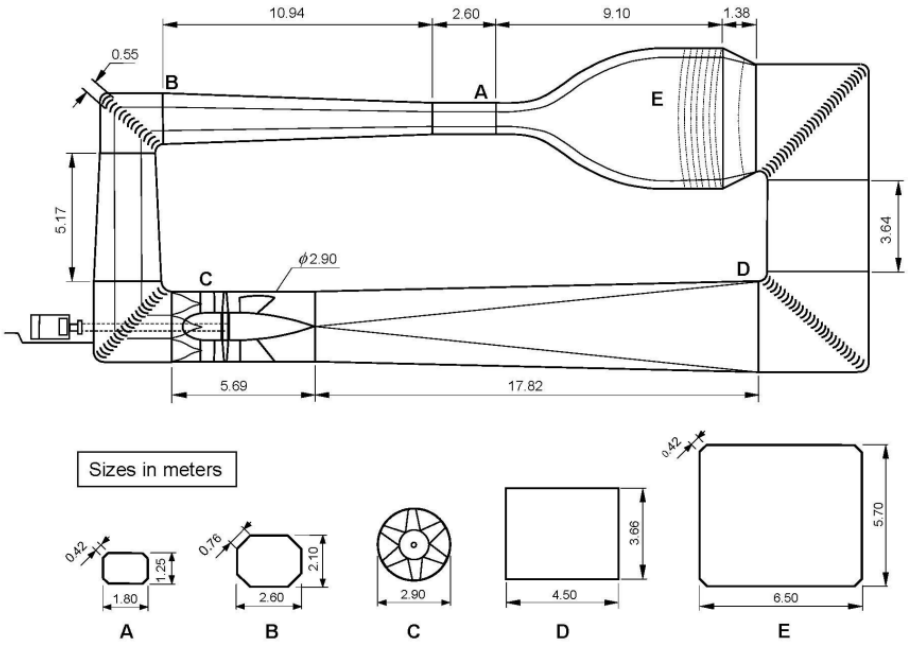

Figure 2.3: LTT Tunnel Layout and Test Section Cross Section [49].

2.5. Measurement Techniques

The measurement techniques were based on a compromise between measuring the relevant aerodynamic parameters, visualising the desired phenomena, and staying within the allocated time at the wind

tunnel. Therefore, some methods, though potentially helpful in validating the junction flow, such as Particle Image Velocimetry, were not selected as they were not feasible within the time constraints. The selected methods are oil flow visualisation, infrared Thermography (IR), wake-rake measurements, surface pressure Visualisation, and far-field acoustic analysis. The following section will provide an introduction and some considerations for each selected method.

2.5.1. Oil Flow Visualisation

A thin layer of a high-viscosity liquid, such as mineral oil, is coated on the wing surface. This film of oil is displaced due to the friction of the incoming air on the surface. Due to the no-slip conditions, the velocity of the oil at the wing surface is zero, while the velocity at the oil/air interface is constant. The oil has a much larger dynamic viscosity than the air, so the oil boundary layer velocity profile is of a less steep gradient than an air boundary layer profile. The motion of the oil layer on the model's surface reveals the airflow direction when the pressure gradient is minor compared to the wall shear stress, typically observed over flat plates or airfoils without flow separation. However, in cases where flow separation occurs and shear stress diminishes locally, the oil's motion is predominantly influenced by the pressure gradient. Under these circumstances, the oil flow visualisation method loses its reliability for accurately depicting surface skin-friction lines [42]. Particular care must be taken when preparing the oil as the thickness of the oil medium plays a role in the speed and ability to visualise the streaks on the wing surface [32].

2.5.2. Infrared Thermography

Infrared Thermography is another flow visualisation technique that helps visualise boundary layer progression and transition to turbulence. A wing made of a non-conductive material is heated in the wind tunnel. Furthermore, an infrared camera is pointed at the wing to observe the surface temperature. The incoming air can have a heating or cooling effect on the wing's surface through convection. The convection is caused by the surface shear stress, which is itself a function of the state of the boundary layer and is defined as such:

$$\frac{St}{c_f} = \frac{1}{2}\mathrm{Pr}^{-2/3} \tag{2.20}$$

- St: Stanton number, a dimensionless number that measures the ratio of heat transferred into a fluid to the thermal capacity of the fluid.
- c_f: Skin friction coefficient, a dimensionless number quantifying the resistance to movement (friction) between a fluid and a surface.
- Pr: Prandtl number, a dimensionless number characterising the relative thickness of a fluid's momentum and thermal boundary layers.

As the boundary layer progresses, it thickens, and the wall shear stress decreases; hence, the surface heat transfer will also decrease in the streamwise direction, increasing the surface temperature of the wing. Furthermore, when the boundary layer transitions from laminar to turbulence, the shear stress increases and thus increases the heat transfer; as such, the local surface cools down significantly. Furthermore, when the flow separates, the shear stress and heat transfer will go to zero [42]. These phenomena become visible when the IR camera is faced to the wing and allow for visualisation in cases of separation and transition.

2.5.3. Far Field Noise Analysis

A microphone array is positioned on the side of the test section to capture the noise produced by the wing. The acoustic data can then be transformed to the frequency domain to visualise the spectral characteristics of the noise. Moreover, further processing the microphone outputs makes it possible to perform a beamforming analysis (which visualises noise sources intersecting a user-defined scan grid). As such, beamforming analysis will be performed in this thesis using a Generalized Inverse Beamforming technique developed and validated by [7, 6, 39, 40].

2.5.4. Beamforming

Beamforming is a method that identifies and characterises different noise sources in the test section. A 2D microphone array is placed facing a stationary noise source. If the sound wave produced by the noise source is perpendicular to the array, all microphone elements will pick up an incoming wave in unison. However, due to the soundwaves' curved wavefront and the noise source's relative location to the array, the sound wave impinges each microphone at separate times. To account for this, one can introduce delays to the microphone responses in the frequency domain to maximise array output and "steer" the directivity of the array in the direction of the noise source. This output can then be processed to provide an analysed noise source heatmap of the scan grid, wherein a noise source emits a wave that propagates and intersects the scan grid. Particular care needs to be made in the array size and arrangements as considering the equations for angular and spatial resolution:

$$\theta_B = 1.22\frac{\lambda}{L} \tag{2.21}$$

$$\theta_B z_s = 1.22\frac{cz_s}{fL} \tag{2.22}$$

Where θ_B is the steering angle, λ is the wavelength, f is the frequency, c is the speed of light, L is the aperture of the array and z_s is the distance, of the scan grid. From the equation, the size of the array plays a role in determining not only what wavelengths can be observed but also the spatial resolution of the heat map. The equation for spatial resolution is also called the Rayleigh criteria; having a fine enough resolution is desired to reliably identify separate sources.

Furthermore, the Nyquist frequency is another factor in beamforming. It provides a frequency range that limits aliasing and ensures more accurate spatial and temporal resolution of sound waves. In this context, there are two Nyquist frequencies to consider: the temporal Nyquist frequency and the spatial Nyquist frequency, both of which influence the design and performance of a beamforming array.

The temporal Nyquist frequency represents the highest frequency that can be accurately sampled by the system and is defined as half the sampling frequency, calculated as $f_{\text{Nyquist}} = \frac{f_{\text{sampling}}}{2}$. Aliasing occurs if the signal frequency exceeds this limit, resulting in high-frequency components being summed back into lower frequencies in the recorded data.

In addition to the temporal Nyquist frequency, beamforming also considers the spatial Nyquist frequency, which relates to the microphone array's configuration. This spatial Nyquist frequency indicates the highest spatial frequency; the array can resolve that and depends on the spacing between adjacent microphones, d, and the speed of sound, c. It is given by:

$$f_{\text{Nyquist, spatial}} = \frac{c}{2d}$$

When the frequency of the incoming wave exceeds this limit, spatial aliasing occurs, causing the array to resolve the angle of arrival inaccurately. In beamforming exceeding this spatial Nyquist frequency can create spurious (ghost) sources in the heatmap.

2.5.5. Surface Pressure Visualisation

Another parameter used to validate PowerFLOW is the surface pressure of the junction wing. Specifically, two different pressure measurements will be discussed. The surface static pressure will be measured at three spanwise intervals, whereas Taipro MiniP sensors will be used to measure the dynamic fluctuation of surface pressure near the junction region.

Surface Pressure Taps

To measure the static pressure on the surface of the wings, holes are drilled perpendicular to the wing's surface. These holes are pressurised by the tangent (uniform) airflow. These pressure taps are connected with tubes to a pressure transducer, which measures the static pressure at the surfaces [24].

Surface Microphones

The static pressure taps capture the pressure distribution around an airfoil. However, acoustic noise is produced by the smaller pressure fluctuations, which the static pressure taps are not able to capture. Therefore, a seperate sensor would be required to measure and characterise the smaller unsteady pressure fluctuations near the junction region. The sensor in question are the TaiPRO MiniP_1,2_002_A_LT sensors. These 1.2mm diameter sensors can operate at a pressure range of 0-2 bar, accuracy of 1mBar and a sampling frequency of 50kHz. These pressure transducers have greater sensitivities than pressure taps and are sensitive to a wide range of frequencies making them applicable in measuring the frequencies in the junction region.

2.6. Reynolds Number Effects & Corrections

Wind tunnel corrections cover multiple domains. Effects such as blockage cause the lift and drag of the wing to deviate from free flight conditions. However, considering the goals of the thesis, recreating free flight conditions was not a priority for the wind tunnel tests. Thus, correcting for effects such as blockage was not considered. However, since the Reynolds number affects the horseshoe vortex formation at the junction, replicating the Reynolds number of free flight conditions was a requirement. Moreover, incorrectly scaling the Reynolds number can profoundly affect the wing's performance. For example, an incorrect Reynolds number would lead to an incorrect transition location of the boundary layer; the drag will be impacted due to the higher skin friction drag attributed to turbulent boundary layers. Furthermore, considerable deviations in the Reynolds number could cause the flow to separate undesirably, causing a stall. The Reynolds number of full-size wings cannot be replicated using the scaled wind tunnel models exactly. However, specific measures can be taken to mitigate the discrepancies.

2.6.1. Tripping

Adjusting the transition location to mimic the full-scale, free-flight case involves tripping the boundary layer at a specific location. Tripping can be achieved by adding roughness elements on the wing surface, destabilising the laminar flow. A well designed trip must not add additional effects to the flow other than transitioning the boundary layer, such as increasing the boundary layer thickness or producing additional vortices on the wing.

2.6.2. Trip Location

The trip location is determined by finding the transition location using lower-order CFD solvers. A combination of AVL and MSES is used to obtain this. MSES is a 2D airfoil design and analysis tool that employs an Euler flow model, which is solved using a low-order finite volume method. The MSES solver works by iterating between solving the Euler equations for the inviscid flow field and solving the boundary layer equations to account for viscous effects until convergence is obtained. The software is designed to analyse and design multi-element airfoils relevant to a wing strut system [36][23][31]. On the other hand, the Athena Vortex Lattice method is another CFD tool based on the Vortex Lattice Method. Like conventional panel methods, Vortex Lattice Method solve the Laplace equations by calculating the strength of singularities placed on the mean surface of a geometry of interest [2]. However, Vortex Lattice Method differ from panel methods as they are oriented explicitly towards thin lifting surfaces without accounting for airfoil thickness and small angles of attack. These surfaces and trailing wakes are represented as single-layer vortex sheets, discretised into horseshoe vortex filaments [22]. Finally, the Athena Vortex Lattice method assumes quasi-steady flow, meaning that unsteady vorticity shedding is neglected. To determine the local transition location, a global lift coefficient is imposed in the Athena Vortex Lattice method, which then calculates the lift distribution for the discrete panel locations. Finally, MSES uses this distribution to compute the transition location for each spanwise region.

2.6.3. Trip Roughness Height

To establish the critical height of the roughness elements required to trigger premature boundary-layer transition, the method developed by Braslow is selected [18]. For low-Mach-number flows over adiabatic surfaces, the nondimensional roughness height k is determined by the following equation:

$$Re_s = \frac{U \cdot s}{\nu_\infty}$$

$$Re_k = \frac{U_k \cdot k}{\nu} \quad \text{with} \quad U_k < U$$

Here, U_k is the velocity at the roughness height within the undisturbed laminar boundary layer, and is extracted through the CFD simulations. The absolute viscosity ν at the location is equivalent to the dynamic viscosity ν_∞ of the undisturbed flow, which holds for low-Mach-number flows over adiabatic surfaces [43].

Much literature has been published on experimental results regarding the critical value of the roughness Reynolds number, Re_k, over the past 50 years. As collated by Selle [43], the critical value of Re_k is on the order of 600 to 700. Additionally, [43] have demonstrated that for Re_s values below 100,000, the critical roughness height value increases from a constant value of approximately $Re_k = 600$ to as much as $Re_k = 1200$.

3

Experimental & Numerical Setup

This chapter presents the setup processes for both the CFD simulations and the wind tunnel tests conducted in this study. It provides a detailed overview of the CFD mesh configuration and boundary conditions, alongside the preparation of the wind tunnel tests, including the wing model, acoustic lining, and tripping protocol.

3.1. CFD Setup

3.1.1. Mesh Setup

The particle distribution function of the LBM solver is computed on a Cartesian mesh, formally referred to as a lattice. A simplified model of the test section of the LTT is utilized to define the mesh domain, within which the wing is positioned. Both the wing, strut and the LTT walls are prescribed as non-slip walls in order to analyse the effect of vortices at the wall wing junctions.

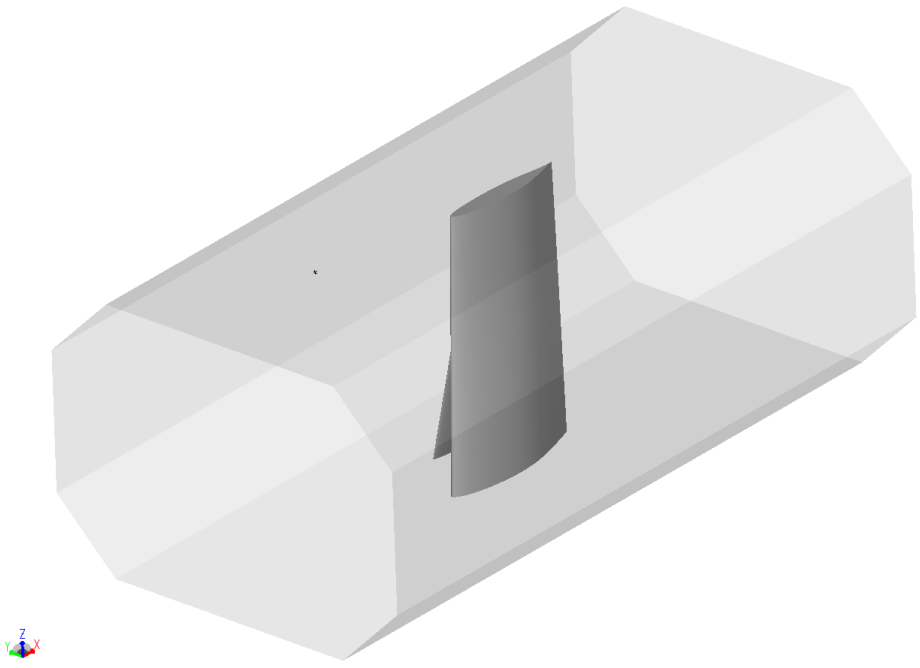

Figure 3.1: Wing Placement in LTT Test Section

Certain modifications were made to the LTT geometry. The geometry was reduced by 0.175% along

the z- and y-axes to eliminate gaps between the tunnel and the wings, as such gaps could introduce instabilities in the CFD simulations. Additionally, the tunnel was extended by 25% along the downstream x-axis to accommodate the wake-rake refinement and ensure consistent mesh resolution at the outlet. Specific regions were also selected for further refinement to locally elevate fidelity without increasing cost in the full domain. A cylindrical refinement illustrated in green in Figure 3.2, was defined to encapsulate the junction region, enabling higher fidelity of the expected horseshoe and corner vortices at the junction.

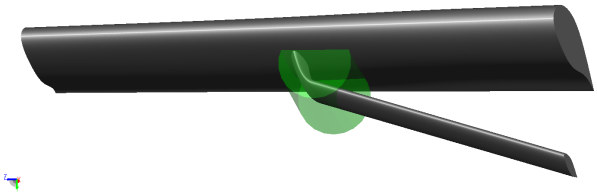

Figure 3.2: Junction Refinement Region

Furthermore, a wing and strut wake refinement region was defined that automatically rotates with the angle of attack as presented in Figure 3.4

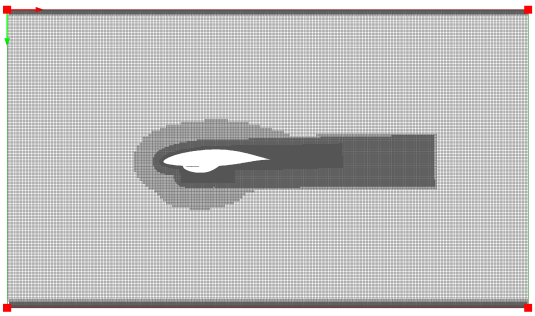

(a) Mesh at 50% span

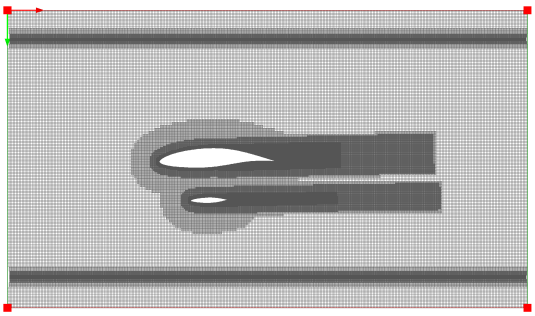

(b) Mesh at 10% span

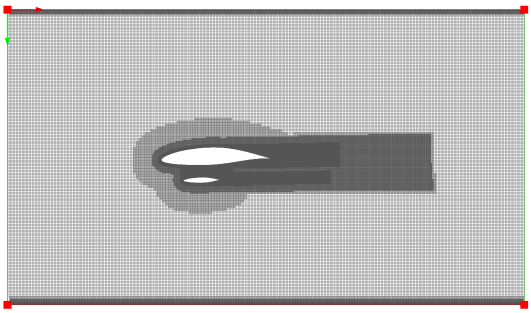

(c) Mesh at 40% span

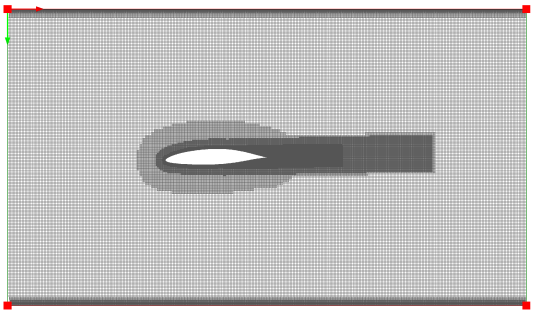

(d) Mesh at 75% span

Figure 3.3: Mesh Slices at Various Span Locations

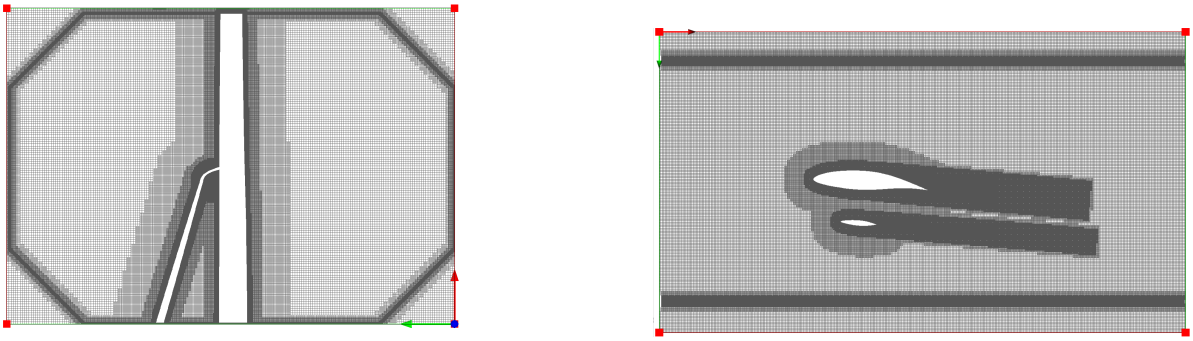

(a) Mesh in the x Orientation

(b) α = 6 Mesh For 10% Span

Figure 3.4: Mesh in Streamwise Direction and Mesh Rotation due to Angle of Attack

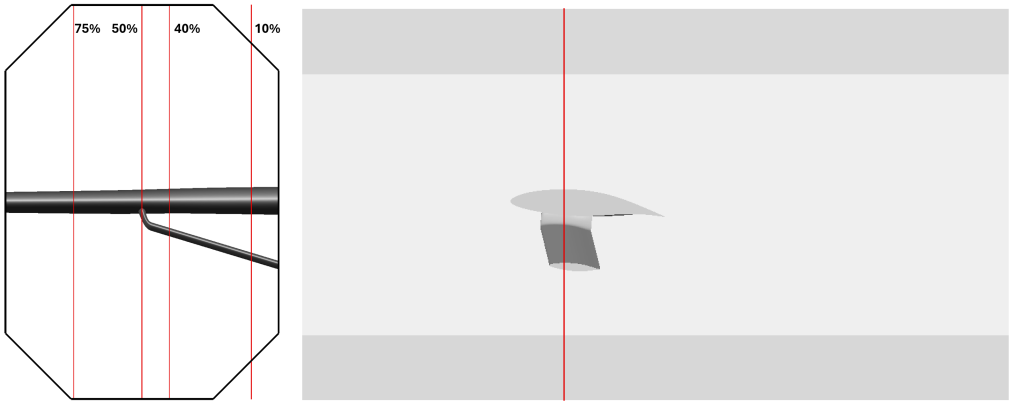

(a) Locations of spanwise slices

(b) Location of chordwise Slice for Mesh in x Orientation

Figure 3.5: Location of Slices for Mesh Visualisation

3.1.2. Mesh Refinement

Commonly, for mesh refinement, regions of interest, or walls with no-slip boundary conditions are meshed as finely as the desired y^+ values. Conversely, regions of lesser interest or the far field are typically meshed with a coarser resolution. While this approach remains applicable for this test case, an additional fidelity requirement is imposed. Due to the direct noise and FW-H computations being performed, limitations on the coarseness of the far field mesh were necessary to prevent excessive dissipative errors during the propagation of sound waves. As a result, the volume mesh resolution was constrained to have a coarsest resolution of $\frac{1}{4}^{th}$ of the shortest wavelength considered in the acoustic analysis. In addition to the constraint imposed by testing for acoustics, the surface mesh also had to be fine enough to keep the y^+ around 50, and such that the first cell layer is within the boundary log-layer, in accordance with the wall model used.

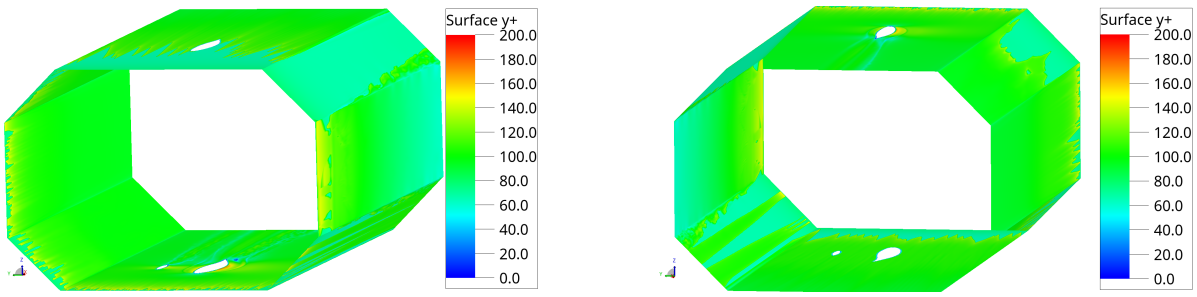

(a) LTT Floor y+

(b) LTT Ceiling y+

Figure 3.6: LTT Walls y+

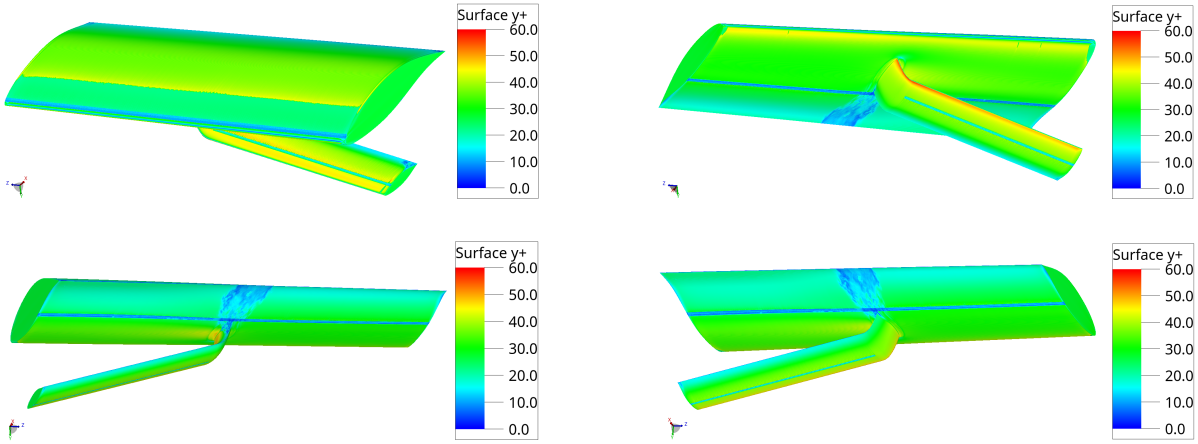

Figure 3.7: Wing y+

3.1.3. Final Mesh Parameters & Boundary Conditions

The final CFD setup had the following parameters. The mesh has the finest voxel size of 1.40×10^{-4} m in regions proximate to wing and strut boundary layer trips. Otherwise, at the wing and strut surface, the mesh has a finest voxel size of 2.80×10^{-4} m. The CFD simulation has in total 15 levels of variable resolution, of which 5 are offsets of the wing and strut at increasing variable resolution levels (getting coarser at each level), 2 are offsets of the wind tunnel walls, and the remaining is for regions of the wing wake or junction region.

For the junction refinement region between the wing and the strut (as seen in Figure 3.2), the voxel size was 5.60×10^{-4} m. The far-field regions of the domain use a coarser mesh, with voxel sizes reaching a maximum length of 8.96×10^{-3} m. Ultimately, the mesh comprises 646,625,121 voxels, with a fine equivalent voxel count of 177,621,517.

The wall model for the simulation options was set to automatic. Standard no-slip wall boundary conditions were assigned to the tunnel walls, wing, strut, and trip surfaces, with an automatic boundary layer type setting that dynamically adjusts to the flow conditions. The inlet boundary condition is defined as a velocity inlet with a streamwise velocity matching that of the wind tunnel for the specific test run the CFD simulation aims to replicate. The outlet is defined as a pressure outlet, specified according to the ambient pressure conditions in the LTT.

3.1.4. Stored Data and Measurements

All measurement recordings commence following an initialisation period spanning the first 0.154876 seconds to stabilise flow conditions before the primary data collection period. Distinct measurements were established for different simulation aspects. Firstly, a standard fluid measurement is implemented across the entire simulation volume for the duration of the runtime, capturing the steady state standard fluid variables, turbulence characteristics, and surface measurements. Additionally, a similar fluid snapshot is recorded for a single timeframe immediately post-initialisation.

Two composite measurement files were made to track forces and moments at the wing and strut surfaces. One of these files begins recording from timestep zero, while the other initiates after the completion of the initialisation period. These files are used to analyse simulation convergence.

A specialised surface measurement file was configured for the FW-H analysis, focusing exclusively on the wing and strut faces. This measurement captures pressure and velocity pressure data at a measurement interval of 2.083×10^{-5} s with a linear measurement cell width of 0.00721042 m, providing refined spatial resolution for aeroacoustic analysis. The values were obtained by defining an estimated frequency regime of interest (which was based on previous papers on Junction flow) and then using multiples (4) of constricting wave length and periods as the period and measurement intervals.

Nine probe measurements were established to monitor unsteady pressure at the location of the Taipro MiniP sensors. Finally, a standard fluid measurement was also conducted for the direct noise compu-

tation, focusing solely on pressure measurements. This direct noise measurement applies the same temporal and spatial resolutions as the FW-H setup, with a measurement interval of 2.083×10^{-5} s and a cell width of 0.00721042 m.

3.1.5. Simulation Parameters & Runtime

The simulations were conducted over a total of 497,558 timesteps, with each timestep set to 4.868×10^{-7} s, resulting in a cumulative simulation time of 0.221 seconds. Furthermore, the simulation was seeded using a coarser result, where the 3 finest mesh sizes were omitted. The simulations were run using 560 cores for a total of 29,850 CPU hours.

3.2. Experimental Setup

3.2.1. LTT Acoustic Lining

An acoustic lining was applied to enhance the acoustic performance of the LTT test section per [5]. Specifically, 3 cm melamine foam panels covered the top, bottom and diagonal panels. Furthermore, the diagonal walls and the panel opposite the microphone array were covered with Kevlar panels. The turntable was also be lined with melamine, including a precisely laser-cut melamine insert to ensure a seamless fit around the wing model. Additionally, melamine panels lined the diffuser as well, with a ramp positioned at the inlet to facilitate a smooth transition into the test section.

The microphone array, as pictured in Figure 3.8, consisted of 64 G.R.A.S. microphones embedded within a melamine array, which a kevlar panel also covered. To prevent acoustic leakage, all gaps between the test section and the diffuser and any other potential openings within the test section were sealed with aluminium tape.

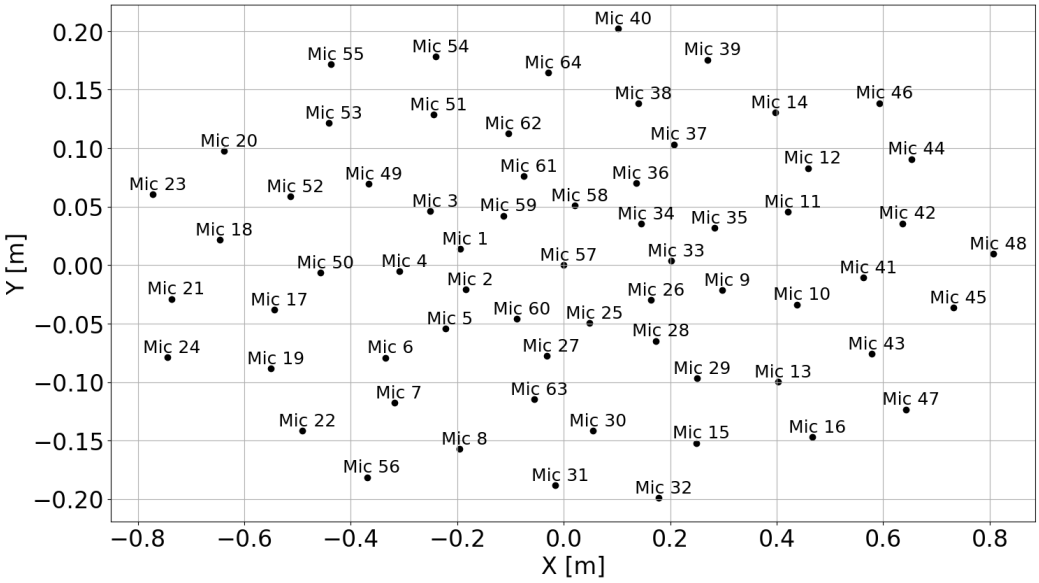

Figure 3.8: LTT Microphone Array Coordinates

3.2.2. Wing Model

The wing to be tested is a spanwise segment of an iteration of the HERWINGT wing. The wing design incorporates multiple airfoil profiles that blended along the span. Furthermore, the wing has spanwise variations in twist and sweep. The wing exhibits a root chord of 714.84 mm, tapering to a tip chord of 611.91 mm. In contrast, the supporting strut maintains a constant chord length of 235.01 mm. Thickness varies along the wing span, measuring 121.64 mm at the root and decreasing to 90.97 mm at the tip, while the strut has a uniform thickness of 35.85 mm. Modifications were made to the wing,

specifically involving the thickening of the trailing edge to accommodate pressure taps. The total span of the wing is 1.248 meters, and it is constructed from Carbon Fibre Reinforced Polymer. Additionally, the wing was constructed with a segmented design to facilitate the removal of the strut, allowing for future testing with various strut configurations.

3.2.3. Pressure Tap Locations

Though it is possible to extract surface static pressure values on any point on the surface using CFD, this is not practical for the wind tunnel model due to difficulties with installation. As such, it was decided to limit the number of pressure taps under 100, and only to analyse three spanwise locations on the wing. The pressure tap locations were selected based on CFD results. In the spanwise direction, locations at 75%, 40%, and 10% were chosen. This selection allows for an analysis of the wing where no wing-strut interference is present (75%), where the wing-strut is expected to have greater interference (40%), and where wing-strut interference exists but is far from the wing-strut intersection location while remaining unaffected by the wind tunnel walls (10%).

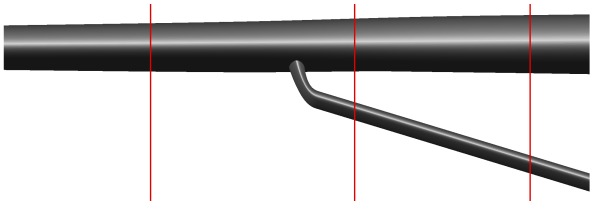

Figure 3.9: Spanwise Location of Static Pressure Taps

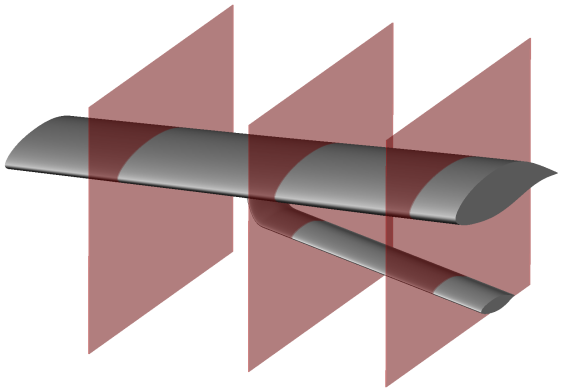

Figure 3.10: Spanwise Location of Static Pressure Taps

Using CFD results, the surface pressure for each spanwise location was extracted. These pressures were then processed through a script to determine pressure tap locations that could best replicate the original data with the minimum number of points. This was achieved using the Ramer–Douglas–Peucker algorithm. The primary objective of the Ramer–Douglas–Peucker algorithm is to approximate a curve with fewer points while preserving its general shape and fidelity within a specified tolerance. The algorithm recursively removes points that do not significantly contribute to the overall geometry of the curve, resulting in a simplified representation that minimizes information loss. By applying the algorithm and incorporating constraints such as minimum distances between taps (due to manufacturing limitations), it was possible to recreate the pressure graphs with the best fit given a specified number of taps per section as shown in Figure 3.11.

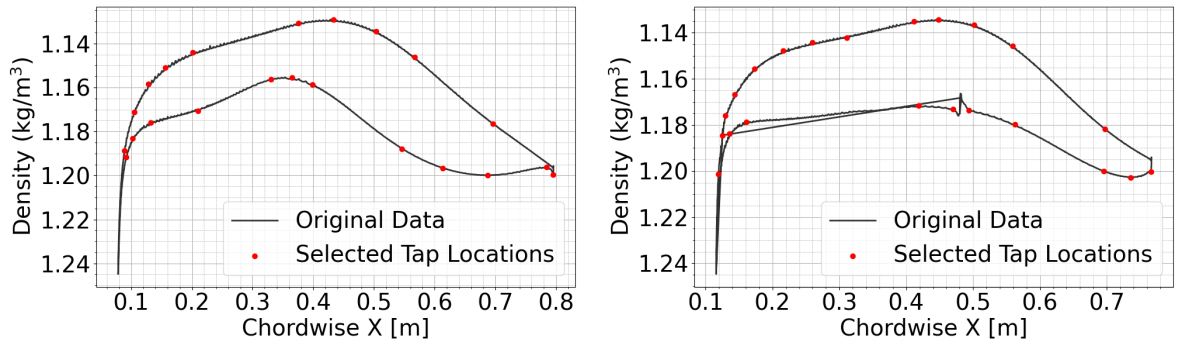

(a) Wing 10% Span Pressure Tap Locations

(b) Wing 75% Span Pressure Tap Locations

Figure 3.11: Pressure Tap Locations for Wing at 10% and 75% Span

3.3. Boundary Layer Transition and Tripping Methodology

3.3.1. Determining the Trip Location

The trip location is determined based on the predicted transition location obtained following the method of section 2.6.2. From the MSES analysis, a non-constant tripping distance was observed. However, in order to make the application of transition strips repeatable (such as to reduce potential for error during re-application of trips), it was decided to implement a constant trip location based on the average chord length calculated from the MSES results.

Figure 3.12 and Figure 3.13 present the location of the wing and strut trips. The blue lines represent the MSES-predicted transition locations for the entire HERWINGT wing, normalized to the chord length. The green vertical lines indicate the spanwise extent of the LTT model. The red line denotes the average transition location, which will be adopted as location for the transition strips for the analysis.

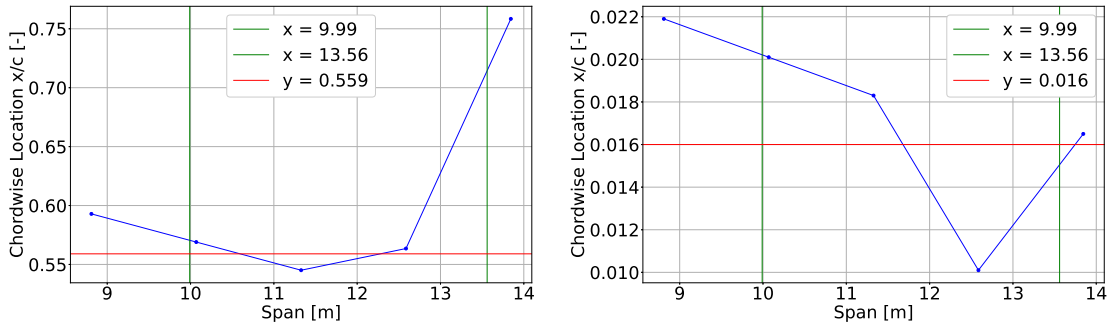

(a) Wing Pressure Side

(b) Wing Suction Side

Figure 3.12: Wing Trip Location

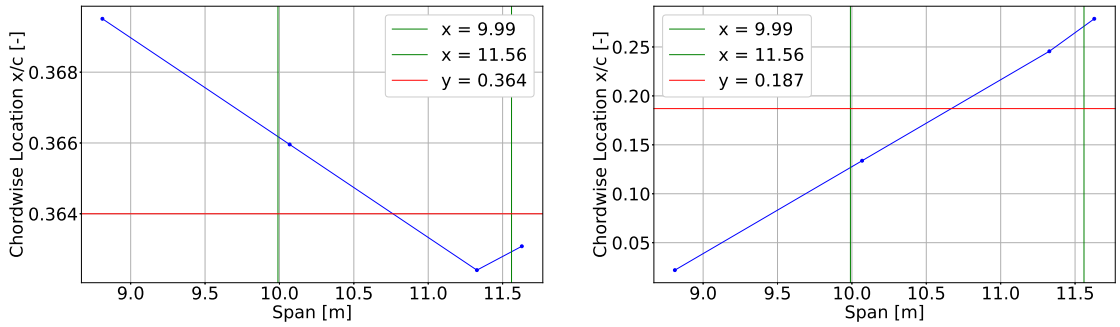

(a) Strut Pressure Side

(b) Strut Suction Side

Figure 3.13: Strut Trip Location

3.3.2. Determining Trip Roughness Height

Tripping height was calculated as per section 2.6.3. The selected Re_K value was 700, based on relevant literature, this produced a trip height of 0.4mm in the wing and 0.2mm at the strut. These trips were then simulated to validate their effectively.

However, given the large ranges in Re_k that were suggested by literature, it was important to verify the trip's effectiveness. Thus, to quantitatively understand whether the trips induce transition, the dimensionless turbulence intensity I is used which is defined as:

$$I = \sqrt{\frac{2}{3}\frac{k_{turb}}{|\mathbf{U}|^2}}$$

Where k_{turb} is the turbulent kinetic energy in m^2/s^2 and $\mathbf{U}$ is the velocity in m/s. Literature suggest a turbulence intensity values of 5% - 10% turbulent to be highly turbulent [27, 19, 15]. These values were tested in CFD simulations and verified to reach the required thresholds before being applied to the wind tunnel models.

3.3.3. Trip Implementation CFD

The trips were applied to the wing geometry using CATIA 3DEXPERIENCE R2024. However, due to the non-constant airfoil profile of the wing, along with its twist, sweep, and potential modifications to the wing design, simple transformations of an existing trip geometry were not feasible. Additionally, to ensure no gaps between the trip and the wing geometry, the trip application process needed to use the wing surface as an input and be repeatable in case of any iterations in the wing design. During this thesis, a CATIA macro instruction was developed, enabling a user to draw trips of any dimension directly onto the surface of any surface by specifying only the trip geometry and chordwise location. A user guide for the Macro is added to appendix A of this thesis. This approach resulted in a simple, repeatable workflow that produces geometric trips that lie perfectly flush on any wing (or strut) design.

3.3.4. CFD Trip Results

This section discusses the application of turbulent trips in PowerFLOW simulations and their impact on turbulence modelling. Despite the sufficient turbulence intensity on the boundary layer to cause transition to turbulence, an analysis of the instantaneous $\lambda 2$ isosurfaces (to gain a visual representation of the flow structures) revealed that PowerFLOW's turbulence model did not trigger the VLES model, which would allow for unsteady flow structures to be resolved.

As discussed in Section 2.3.4, in the context of the VLES model, resolved and modelled flow refers to two approaches for capturing the different scales of turbulent eddies. Resolved turbulence involves directly simulating the larger, energy-carrying eddies that influences the flow and are defined by the grid resolution and the numerical scheme. These larger structures are case-dependent (not universal), as specific flow conditions, geometry, and Reynolds number influence their behaviour and scale.

In contrast, modelled flow pertains to the smaller, subgrid-scale eddies that are not resolved by the computational grid due to their fine scale. Instead of directly simulating these smaller eddies, a traditional VLES model relies on the subgrid-scale model to approximate their effects on the larger, resolved eddies, which is discussed in equation 2.19. Unlike the resolved scales, these modelled scales are less dependent on case-specific conditions.

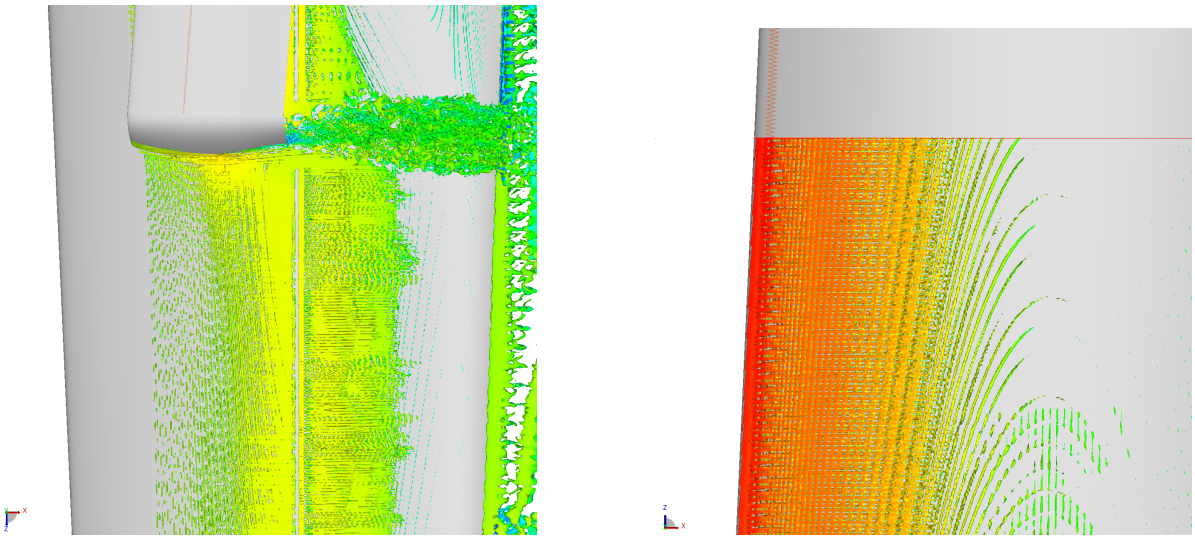

(a) Wing Pressure Side (Trip in Red)

(b) Wing Suction Side (Trip in Red)

Figure 3.14: $\lambda 2$ Isosurfaces at Wing Pressure and Suction Sides (Flow direction to the right, $\lambda 2$ threshold = -80,000)

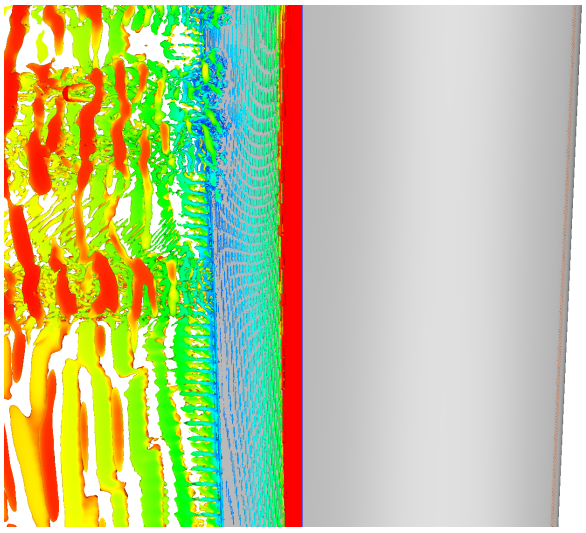

Figure 3.15: Wing Suction Side (Flow direction to the left, Trip near leading edge on the right side, $\lambda 2$ threshold = -80,000)

As seen in Figure 3.15, the region downstream of the trips does not display any unsteady flow structures typically associated with turbulent flow. Instead, the patterns observed correspond to flow structures expected from the subgrid scale model, which are more coherent, almost repeating flow structures; this is especially visible in Figure 3.14; on the wing suction, the turbulence model has not triggered the VLES model at any point, and the flow structures have a repeating pattern visual. Furthermore, at the trailing edge, as displayed in Figure 3.15, though a particular wake shedding exists, they are also repeating and not what would be expected had the VLES modell been triggered (where the flow structures would look chaotic and not unsteady). Specifically speaking, the only region that seems to have triggered the VLES model is seen in Figure 3.16, where the unsteady, non-repeating flow structures are visible at

the junction's region and its wake.

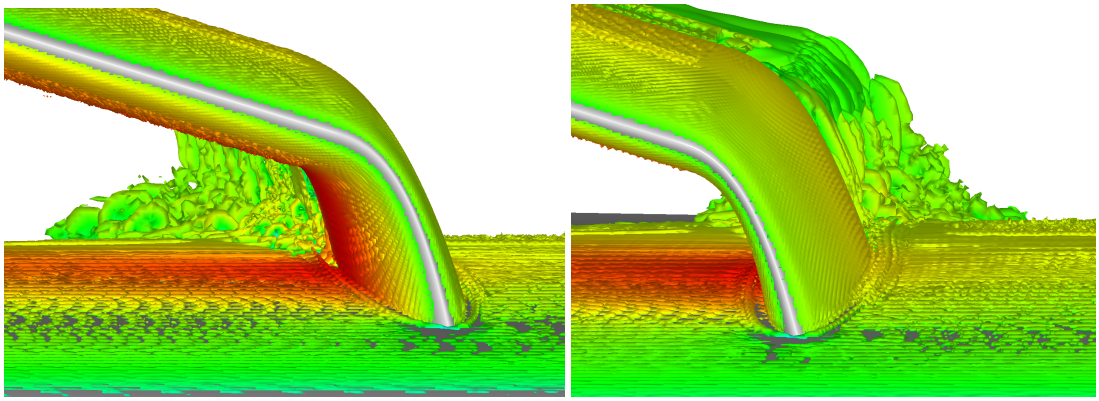

(a) $\lambda 2$ at Junction Region (2) **(b)** $\lambda 2$ at Junction Region

Figure 3.16: $\lambda 2$ Isosurfaces: Junction Region

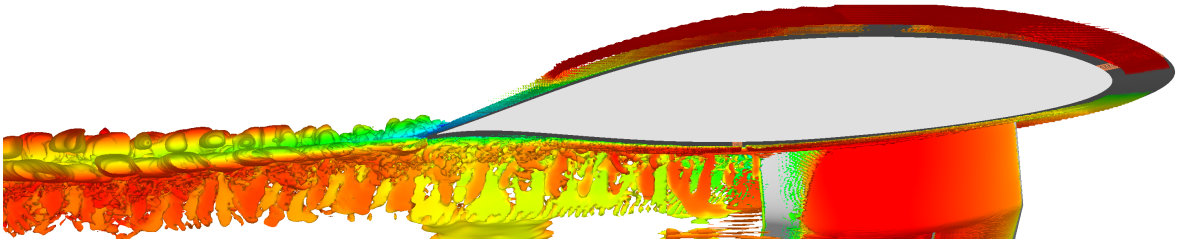

Figure 3.17: Profile of Wing Wake

The transition to the VLES model occurring only at specific spanwise locations—particularly in the junction region—may be attributed to the significant larger unsteady flow structures generated by the junction and the increased mesh refinement in that area. To assess the impact of mesh resolution on triggering the turbulence mode, trial runs were conducted with higher resolutions; however, this did not expand the region of the wing where the VLES model was activated.

As stated, the junction might have triggered the VLES model due to the larger vortices in that region; this might indicate that the trips may not be large enough to produce larger vortices that can trigger the turbulence model. The outcome of this analysis suggests potential gaps in understanding the turbulence model or simulation parameters within PowerFLOW. Considering the importance of validating the aeroacoustics of the strut-braced wing, the inability to resolve unsteady vortices implies that the unsteady flow structures responsible for surface pressure fluctuations may not exist in the CFD simulation, thereby risking inaccurate modelling or the complete absence of certain pressure fluctuations on the wing surface.

4

Steady State Results

This chapter compares results from the steady measurements—which are the oil flow visualization, IR, static pressure tap readings, and wake rake measurements. The oil flow and IR visualization results are examined alongside corresponding surface visualizations generated by PowerFLOW. Static pressure data from the pressure taps are compared with static pressure predictions from PowerFLOW, while wake rake measurements are evaluated against velocity probe data from PowerFLOW at similar locations. These comparisons will assess PowerFLOW's capability to predict the steady-state aerodynamic parameters of the strut-braced wing.

4.1. Wing Placement & Misalignments

During experimental testing, initial static pressure measurements revealed a considerable mismatch with the numerical predictions. Further investigation indicated that this discrepancy likely stemmed from differences in the angle of attack definitions and the centre of rotation between the CFD and LTT models. Using a laser-level tool, it was determined that the LTT model deviated from the CFD configuration by -1.13 degrees and was not perfectly aligned regarding position. Additionally, each model's centre of rotation was defined differently, contributing further to the misalignment. To mitigate the errors, adjustments were made to the CFD model to better match the experimental setup. However, as discussed in later sections, these corrections may not have completely aligned the LTT with the CFD model, leading to persistent deviations in both the angle of attack and wing positioning, which affected the consistency between the numerical and experimental findings.

4.2. Flow Visualisation

The flow visualisation techniques offer a qualitative perspective on the flow development along the wing, horseshoe vortices, and corner flow separation. Two measurement techniques were chosen: IR Thermography and oil flow visualization. IR Thermography was selected for its cost-effectiveness and speed, allowing for non-intrusive testing. It also provided an on-the-line method to check the effectiveness of the transition trips, which could be performed in tandem with wake rake and pressure measurements. The IR thermography results would also be used to validate the transition prediction of the CFD solver, as the skin friction drag will be compared with the IR images.

The oil flow Visualisation was also chosen to validate the flowfield of the CFD. While oil flow can also provide insights into flow transition and separation, its additional benefit is the visualisation of fluid streaks on the wing body; unlike IR thermography, where the camera position and heating lamp's strength limit the user, oil flow visualisation allows users to enter the test section after the wind tunnel stops and obtain images of oil streaks from any perspective they wish. This is especially useful because, as will be seen later, the IR camera's perspective does not allow for close inspection of the junction. Furthermore, it was only possible to extract IR images for the wing pressure side as the IR lamps were not strong enough to heat the wing suction side (which was not an issue for the oil flow visualisation). The oil flow images will then be compared with the Line Integral Convolution (LIC) surface images,

providing a point of comparison for the validation process.

4.2.1. 0° Angle of Attack

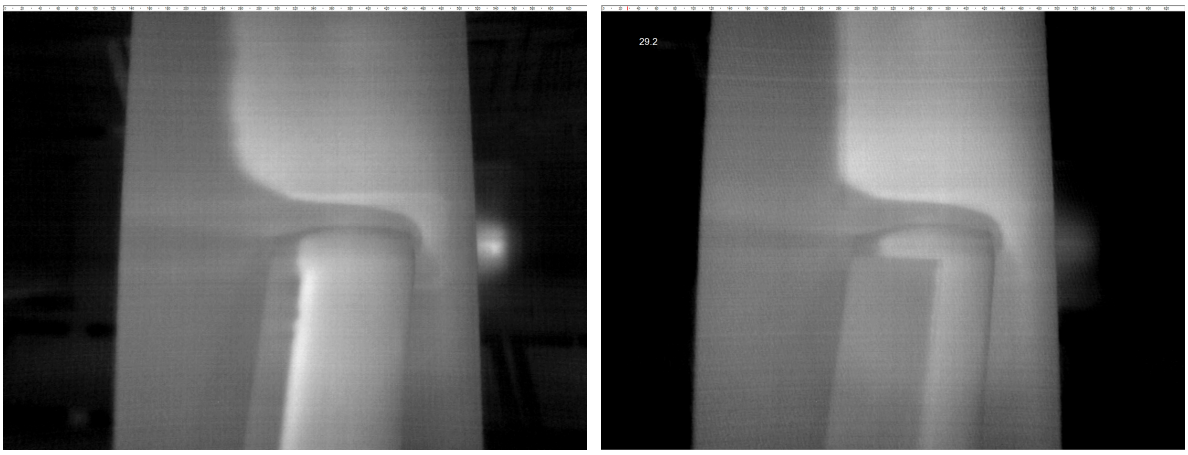

(a) Untripped IR

(b) Tripped IR

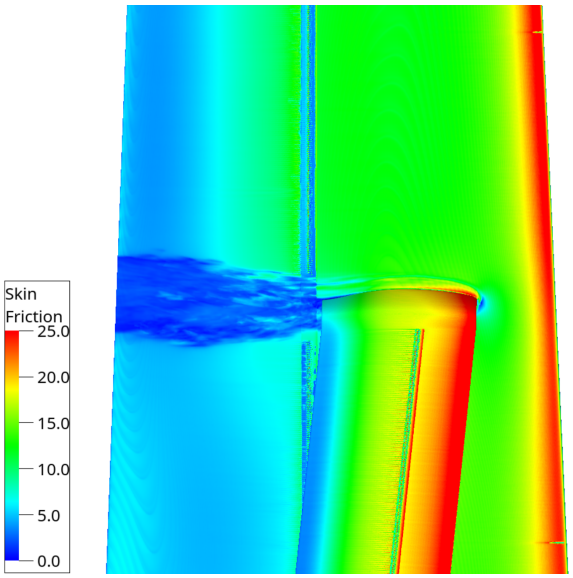

(c) CFD Tripped Skin Friction

Figure 4.1: Comparison of Untripped and Tripped Wing Boundary Layer for AoA = 0°

Figure 4.1 presents the clean (untripped), tripped and CFD skin friction wing boundary layer at 70ms^{-1}. Notice in subfigure 4.1a the consistent transition locations across the entire span of the strut. In order to maintain the consistency of trip locations, it was decided only to trip the horizontal segment of the strut; as such, the vertical section will always be untripped, leading to the changing transition location between the horizontal and vertical parts of the strut which are visible in Figure 4.1b. The experimental and numerical wings are tripped with identical transition strips and flow conditions. No interaction is observed between the tripped and untripped regions, and the location of transition from tripped to untripped changes instantly.

Comparing subfigures 4.1b and 4.1c, the numerical results do not seem to present such stark contrast between the tripped and untripped region, and in fact, appear to be untripped. Regarding the junction region, the saddle point and corner separation seem to be equally visible. From Figure 4.1, it appears that PowerFLOW seems to be less sensitive to the effects of the surface roughness element and is unable to correctly transition the boundary layer into turbulent.

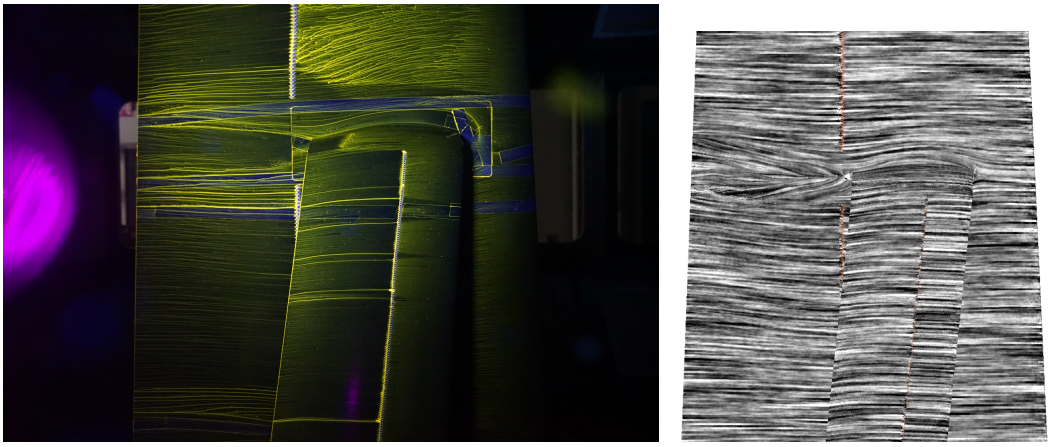

(a) LTT Oil Flow Visualisation **(b)** CFD LIC Visualisation

Figure 4.2: Flow visualization at 0° AoA, comparing the Wing pressure side

In Figure 4.2, the oil flow results show similar results of the Horseshoe Vortex and Corner separation region and their similarly sized wakes. The LIC images do not show a discernible transition point; however, looking at the corner vortex separations, the similar fishtail wake shape due to the corner separation seems to be visible in both numerical and experimental results.

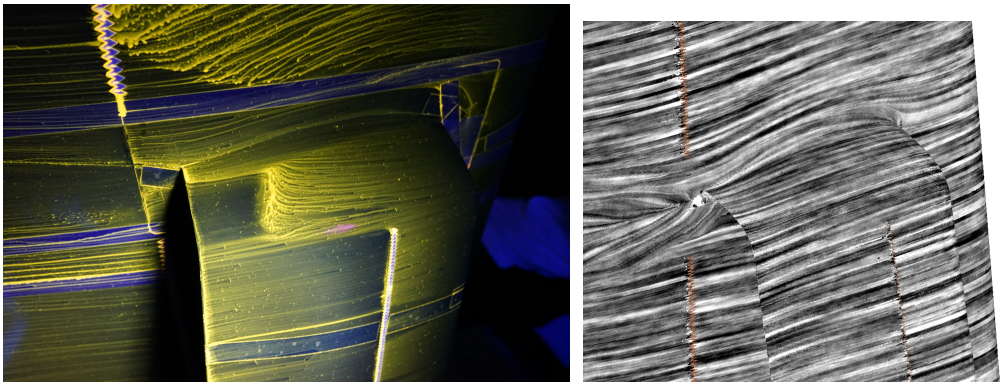

(a) LTT Oil Flow Visualisation **(b)** CFD LIC Visualisation

Figure 4.3: Flow visualization at 0° AoA, comparing the strut pressure side.

Looking at Figure 4.3, the effect of not tripping the vertical section of the strut is now clearly visible. In Figure 4.3a, the transition location moves from the tripped horizontal region to the untripped region just like in the IR results in Figure 4.1b, with the streamlines switching instantly between the tripped and untripped region; however, the region of the strut just adjacent to the wing, which is under the influence of the leading edge horseshoe vortex, does not appear to show the similar visuals of flow transition, the cause may be that the region is under the influence of the high shear stress of the leading edge Horseshoe Vortex and was turbulent since the leading edge of the strut. This phenomenon is absent in the numerical setup, as the strut appears to behave as if untripped.

On the other hand, the effect of the leading edge Horseshoe Vortex can be seen in both images; in both cases, the leading edge Horseshoe Vortex begins from the saddlepoint and continues until it attaches to the corner separation region. Both methods produced similar flow characteristics in capturing the junction phenomena. The findings follow previous analysis of the underlying discrepancy in the CFD models' ability to recreate effects due to junction flow and effects due to the transition strips.

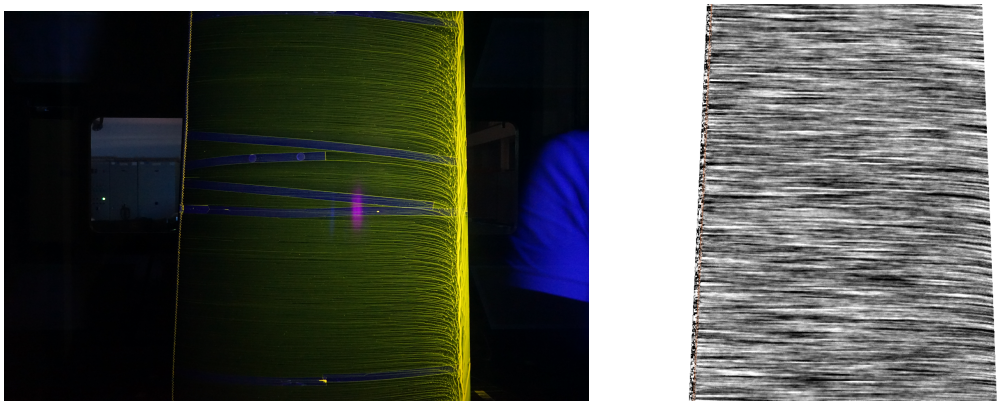

(a) LTT Oil Flow Visualisation **(b)** CFD LIC Visualisation

Figure 4.4: Flow visualization at 0° AoA, comparing the Wing suction side

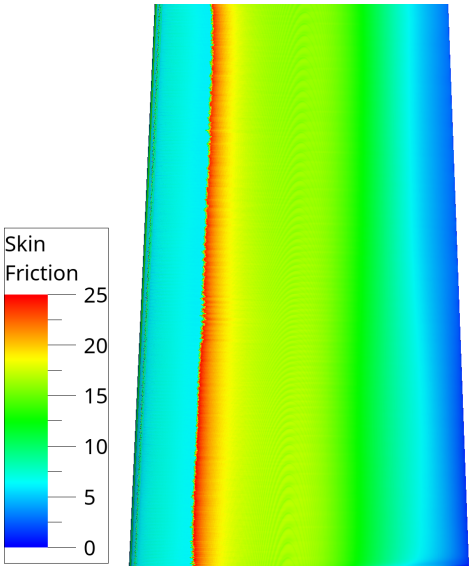

Figure 4.5: CFD Skin Friction of Tripped Wing Suction Side (Flow Direction to the Right)

The skin friction surface distribution from the CFD results is included in Figure 4.5 for more precise visualisation of the suction side. No IR equivalent is available due to the issues pertaining heating the suction side sufficiently. Furthermore, due to the oil flow images not clearly showing the transition location, a stethoscope was used to confirm that the boundary layer was turbulent. This method involved placing the microphone near the wing surface and distinguishing between the quieter sound of a laminar boundary layer and the distinctly louder white noise characteristic of a turbulent boundary layer. The distinct white noise was observed when the microphone transitioned from the untripped region of the suction side to the tripped surface, confirming that the transition strips correctly induced the transition.

Like the oil flow images, LIC images do not clearly distinguish between laminar and turbulent boundary layers. However, in Figure 4.5, the transition from the low skin friction (laminar) region to the high skin friction (turbulent region) region is observed to occur downstream of the transition strips, revealing that unlike in the experimental setup, the transition trips in the numerical model failed to trigger a transition the boundary layer from laminar to turbulent.

Additionally, near the trailing edge, the oil flow results in Figure 4.4a show vertical, downward streaks, indicative of very low velocities in this region. In low-velocity regions, such as near the trailing edge in this case, the streaks fall vertically under the influence of gravity, as the local shear forces are

insufficient to counteract gravitational effects. This behaviour is a clear visual indicator of reduced surface shear stress or potential flow seperation, which aligns with the near-zero skin friction coefficient observed in Figure 4.5, confirming low-velocity flow in that region. The LIC does not show similar downwards streaks in regions of separated or stagnant flow as the oil flow did, because it is a computational visualization technique that operates independently of physical forces such as gravity or surface tension.

4.2.2. 6° Angle of Attack

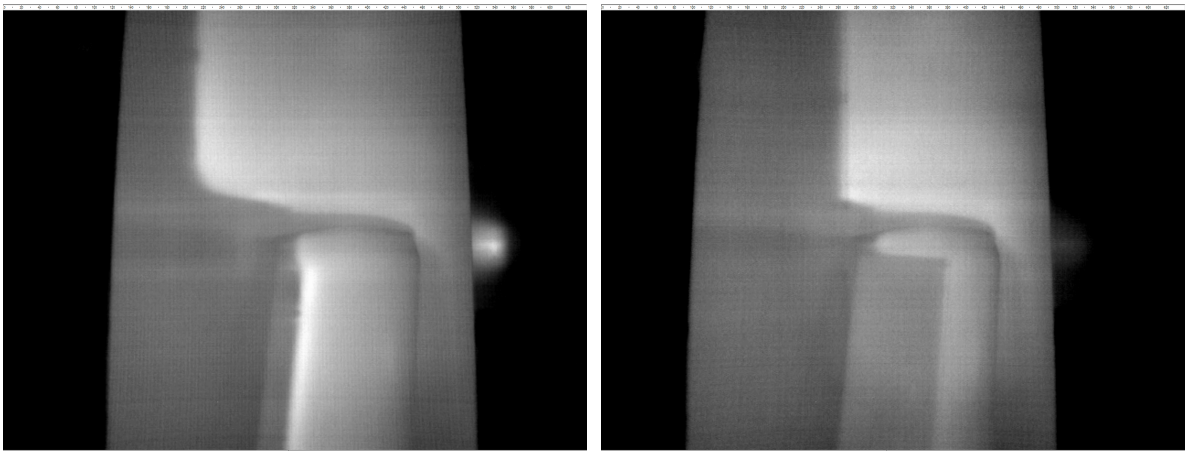

(a) Untripped IR

(b) Tripped IR

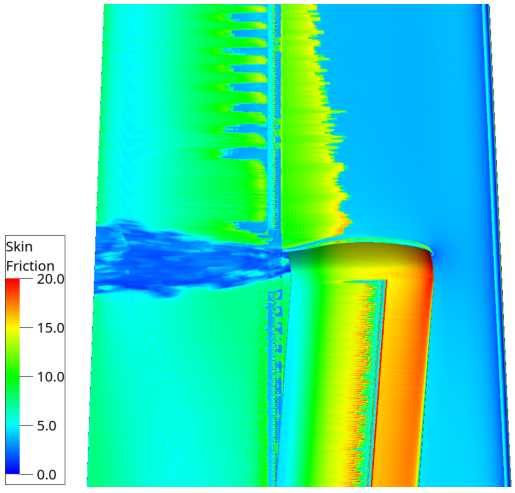

(c) CFD Tripped Skin Friction

Figure 4.6: Comparison of Untripped and Tripped Wing Boundary Layer for AoA = 6°

Figure 4.6 presents the wing boundary layer at six degrees for both numerical and experimental cases and the untripped experimental results. As from Figure 4.1, similar observations can be made again. The LTT boundary layer has been successfully tripped by the transition strips again. On the other hand, the transition location of the CFD boundary layer has moved upstream relative to the 0 angle of attack case. Transition of the boundary layer occurs now before the transition strips, meaning the wall model still incorrectly predicts the transition location. For both cases, the existence of a corner separation wake is evident, as well as the profile of the leading edge Horseshoe Vortex. What can be seen in both experimental and numerical simulations, however, is the effect of the corner separation; it is visible the region under the influence of the corner separation exhibits much higher vorticity than the boundary layer as the IR images present a darker tone, a phenomenon also captured in the CFD results. Moreover, one sees the pattern of the developing vortices in the wake of the corner separation

(for the numerical model) due to the VLES model being activated for the junction region. This time, though, unlike Figure 4.1, the CFD results do not match the untripped IR results. It is not clear what the sensitivity of the transitional model of PowerFLOW is. However, it can be seen that similar-sized transition strips are not being correctly modelled in the numerical model.

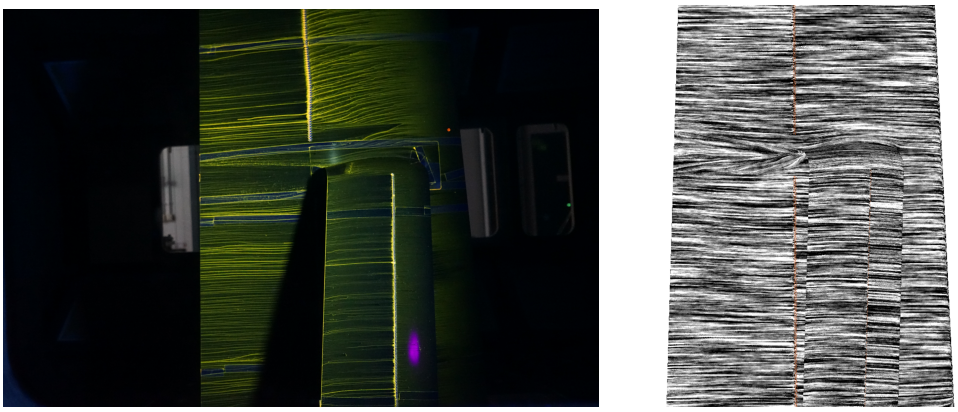

(a) LTT Oil Flow Visualisation **(b)** CFD LIC Visualisation

Figure 4.7: Flow visualization at 6° AoA, comparing the Wing Pressure side

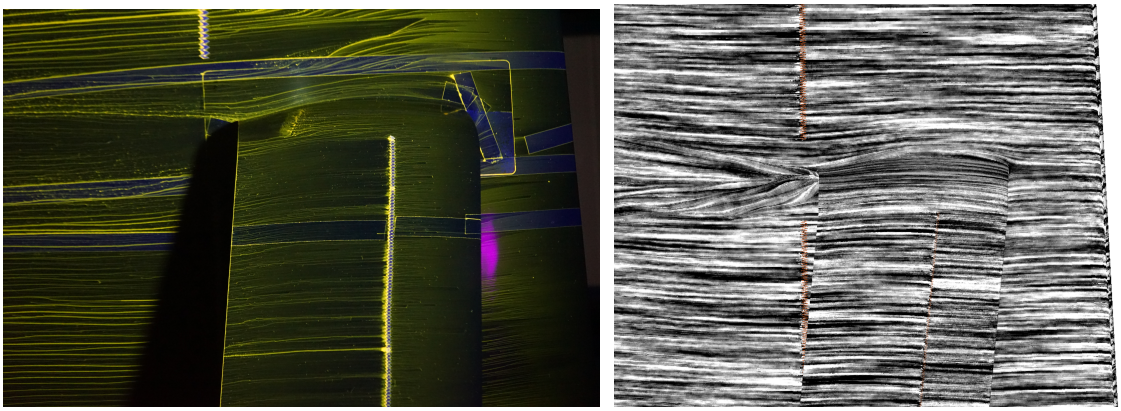

(a) LTT Oil Flow Visualisation **(b)** CFD LIC Visualisation

Figure 4.8: Flow visualization at 6° AoA, comparing the Wing junction region

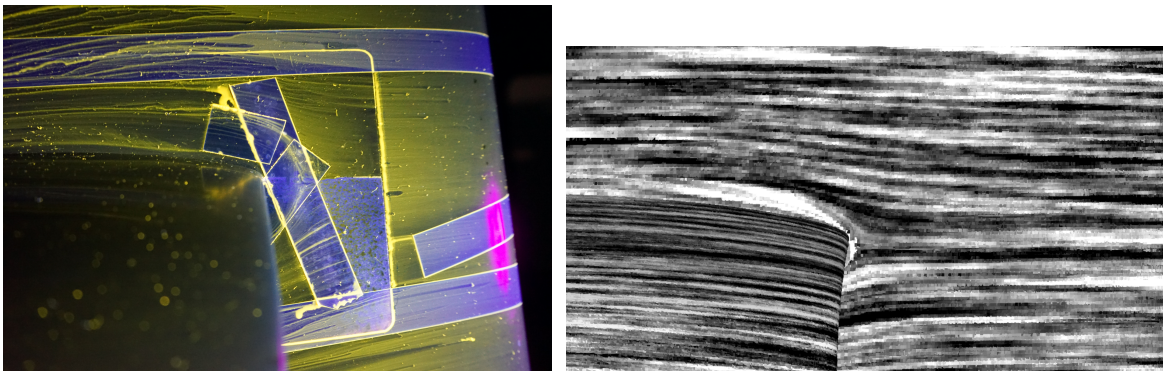

(a) LTT Oil Flow Visualisation **(b)** CFD LIC Visualisation

Figure 4.9: Flow visualization at 6° AoA, comparing the Leading Edge HSV

Figure 4.7, Figure 4.8 and Figure 4.9 all present similar findings as their zero angle of attack counter-

parts. The effect of an angle of attack of this magnitude does not have a perceivable effect on the CFD model's ability to replicate the junction model.

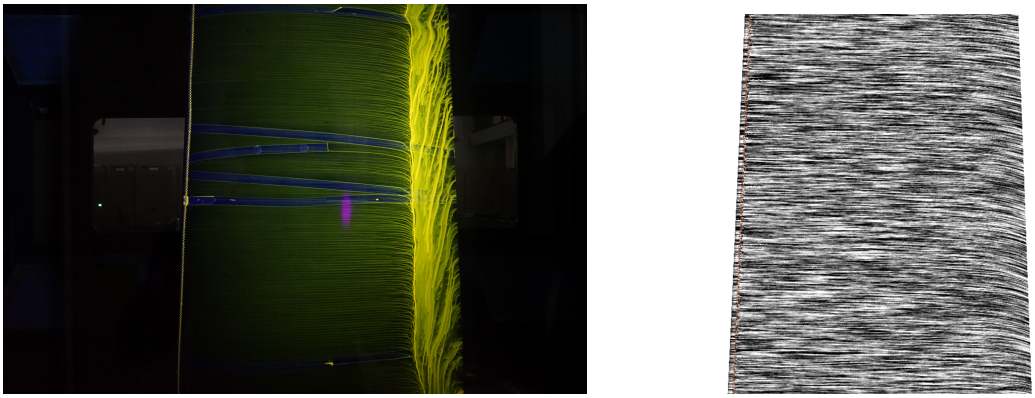

(a) LTT Oil Flow Visualisation **(b)** CFD LIC Visualisation

Figure 4.10: Flow visualization at 6° AoA, comparing the Wing Suction side

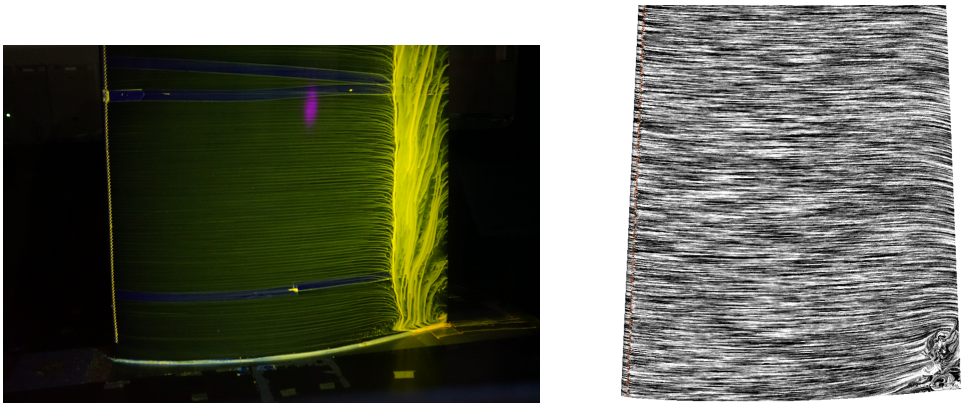

(a) LTT Oil Flow Visualisation **(b)** CFD LIC Visualisation

Figure 4.11: Flow visualization at 6° AoA, comparing the Wing Suction side

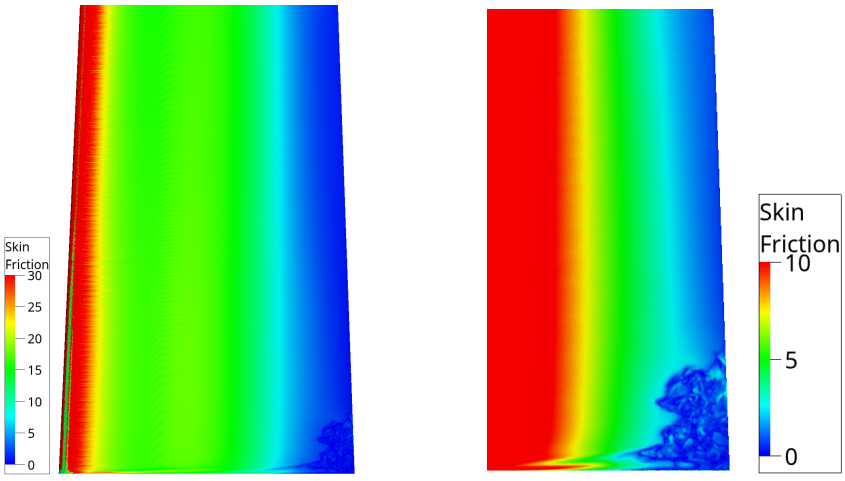

(a) CFD Skin Friction of Wing Suction Side (Flow Direction to the Right) **(b)** Closeup of Wing Tunnel Wall junction (Flow Direction to the Right)

Figure 4.12: Flow visualization at 6° AoA, comparing the root wing trailing edge at the suction side

For the suction side, the CFD results closely mimic the oil flow images for Figure 4.10 and Figure 4.11. Once again, the LIC imaging struggles to show the impact of flow transition and the potential low-shear region at the trailing edge. However, Figure 4.12a shows that at the trailing edge, the skin friction is near zero, complimenting the downward streaks observed in Figure 4.11a.

In summary, concerning PowerFLOW's ability to replicate the flow of the experimental setup, two conclusions can be drawn. Firstly, the LBM wall model struggles to correctly predict the location of the transition, and it seems that the effects of the transition trips are not being correctly realised, leading to different boundary layer states between the models.

Given that the CFD model predicts boundary layer transition occurring too far downstream at zero degrees angle of attack (relative to the LTT) and too far upstream at six degrees angle of attack, a likely source of these discrepancies is the wall model's difficulty in accurately transitioning to a turbulent boundary layer. However, due to the alignment issues discussed in Section 4.1, it is impossible to confidently attribute the flow visualisation errors solely to the wall model, as slight misalignments in the angle of attack would also impact the location of transition for the CFD.

The second conclusion is that with respect to the numerical model's ability to predict junction flow-related phenomena, the LBM solver could still visualise the leading edge Horseshoe Vortex and the corner separation to a high likeness of the numerical results. As such, PowerFLOW was able to capture the phenomena induced by junction flow. Further, the LBM model was observed to have similar zero-velocity flow conditions near the wing's trailing edge.

4.3. Static Pressure Surface Taps

As outlined in Section 3.2.3, pressure taps were installed on both the wing and strut to measure the static pressure distribution at three spanwise locations. This setup enables analysis of the effects and error sensitivities arising from wing-strut interactions and quantifies any interference effects attributable to the strut.

4.3.1. Pressure Coefficient 75% Span

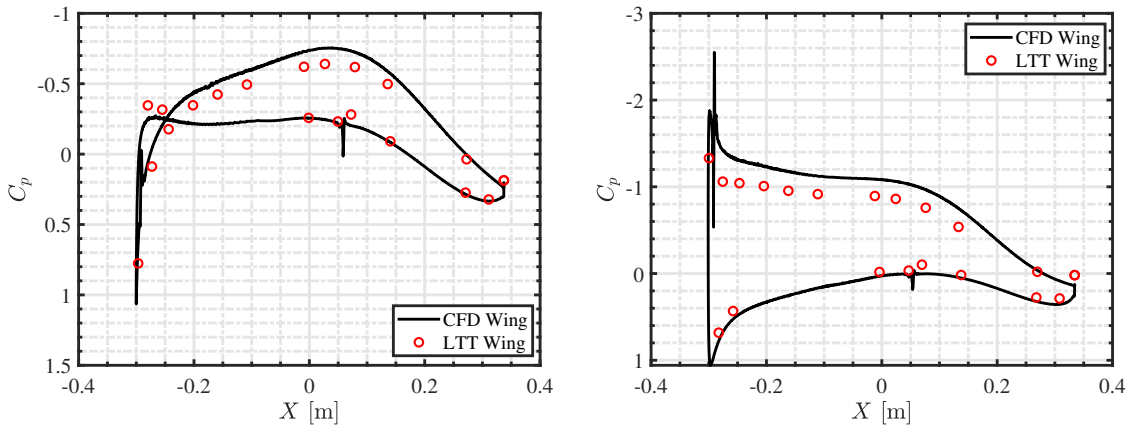

(a) $\alpha = 0°$ **(b)** $\alpha = 6°$

Figure 4.13: Pressure Coefficient Distribution for 75% Span

Figure 4.13 presents the Pressure Coefficient distribution of the wing at 75% span, outboard of the strut region and free from any strut wing interference effects. The first notable observation pertains to the impact of the trips on the pressure distribution of the CFD model, which shows an evident influence of the trips on the surface pressure distribution. Another observation can be made by looking at the trailing edge pressure coefficients; the observations from Section 4.2 was the low velocity, near zero skin friction region on the trailing edge, particularly visible in Figure 4.4, Figure 4.5, Figure 4.10 and Figure 4.12b. A key observation is that the pressure coefficient is nonzero, and no plateau is visible, pointing to a stagnated flow, rather than separated. The pressure coefficient smoothly rises towards a

slightly positive value near the trailing edge, indicating low speed flow with gradual pressure recovery.

The CFD model predicts lower pressure on the suction side of the wing in both zero-degree and six-degree cases, which could indicate that the flow in the CFD simulation experiences stronger suction effects, often associated with a higher effective angle of attack. Referring back to section 4.1, the angle of attack of the CFD model was reduced by 1.13 degrees to replicate the LTT setup better. However, having a more negative suction side indicates that this might have been an insufficient correction, and the angle of attack may need to be reduced further, potentially bringing the pressure distributions closer to the wind tunnel measurements. However, this correction might risk increasing the pressure coefficient on the pressure side of the wing, which would deviate it from the experimental results.

4.3.2. Pressure Coefficient 40% Span

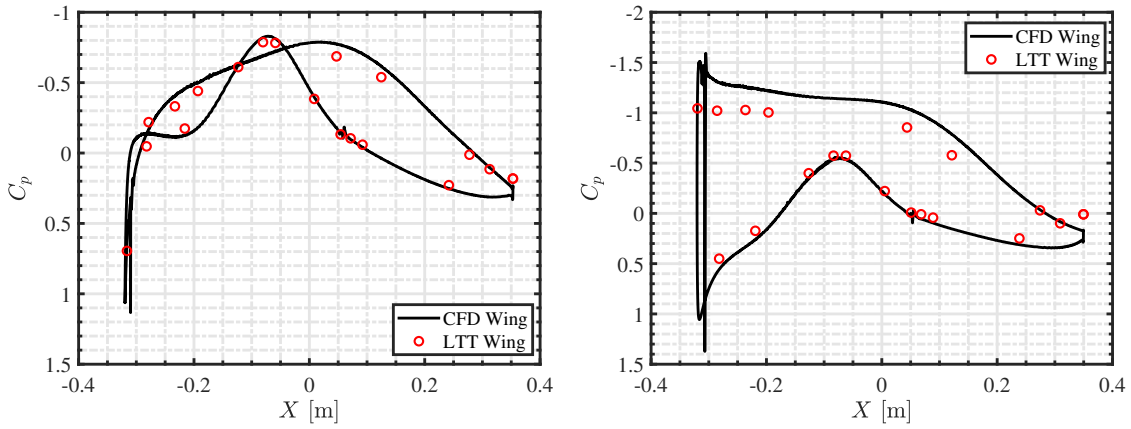

(a) $\alpha = 0°$ **(b)** $\alpha = 6°$

Figure 4.14: Wing Pressure Coefficient for 40% Span

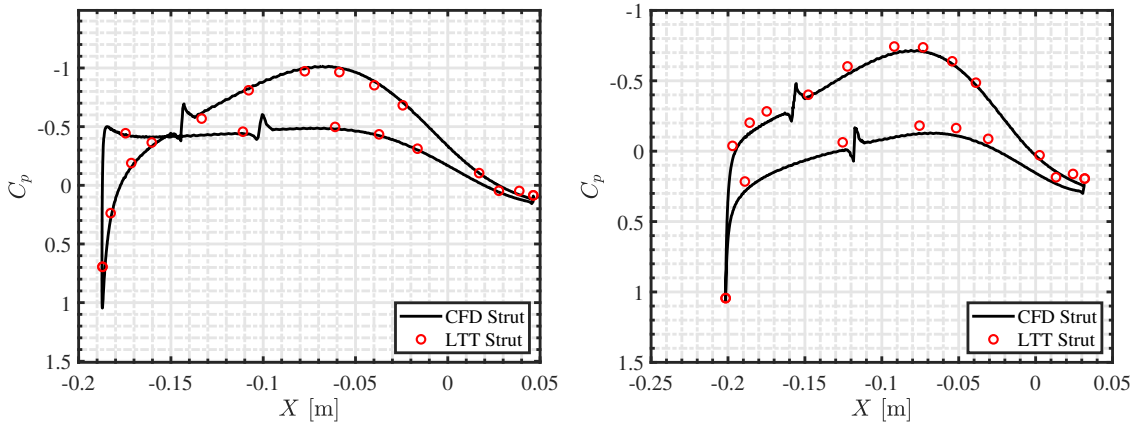

(a) $\alpha = 0°$ **(b)** $\alpha = 6°$

Figure 4.15: Strut Pressure Coefficient for 40% Span

Looking at Figure 4.14 and Figure 4.15, there are fewer pressure points in the LTT pressure distributions due to multiple faulty pressure taps. Figure 4.14 and Figure 4.15 present the wing's and strut's pressure distributions at 40% span, thus near the junction and in the region influenced by the strut. An observation that was visible in Figure 4.13b but is especially prevalent in Figure 4.14b is that the pressure levels do not match at the trailing edge for six degrees angle of attack. This error does not seem observable for the zero degrees angle of attack subfigures. This might be an extention of the

numerical model seeming to be under-predicting the suction side pressure, an observation for the 75% section, too.

Another observation is the effect of the strut, which caused a decrease in pressure on the pressure side of the wing. This is because when a strut is introduced, it creates a blockage effect and locally accelerates the airflow around its surface. According to Bernoulli's principle, an increase in flow velocity leads to a decrease in static pressure. As the airflow accelerates around the strut, the pressure decreases in the region adjacent to the strut, lowering the overall pressure coefficient on the wing's pressure side.

4.3.3. Pressure Coefficient 10% Span

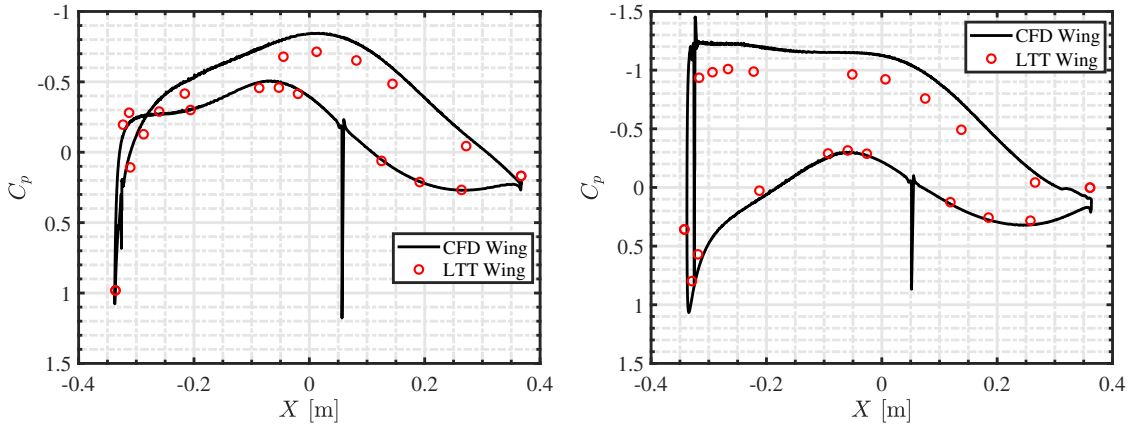

(a) $\alpha = 0°$ **(b)** $\alpha = 6°$

Figure 4.16: Wing Pressure Coefficient for 10% Span

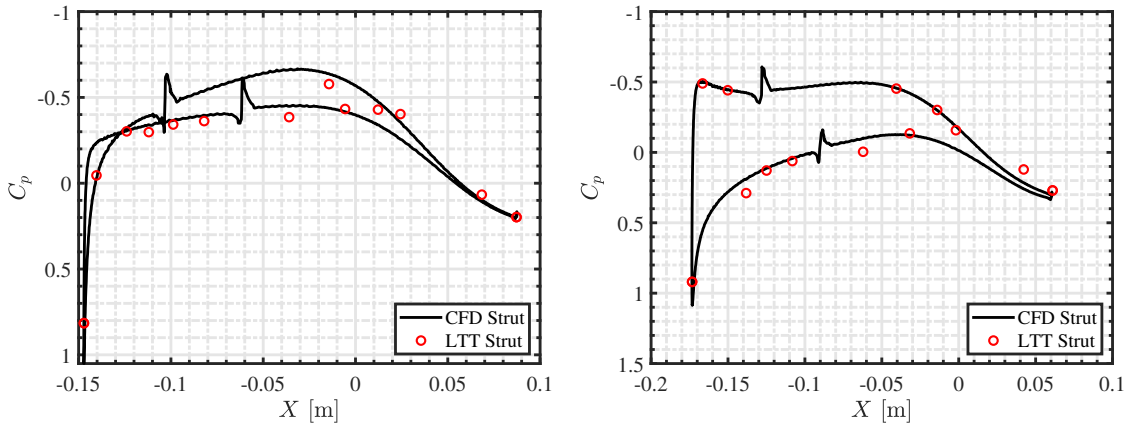

(a) $\alpha = 0°$ **(b)** $\alpha = 6°$

Figure 4.17: Strut Pressure Coefficient for 10% Span

Figures 4.16 and Figures 4.17 present pressure coefficient distributions for the section at 10% of the span (near the wind tunnel walls). Once again, similar observations are made concerning the trips and the trailing edge; however, now, the interference effects of the strut have diminished. Furthermore, the discrepancies in the wing suction side are still present. The faulty pressure taps at the strut make judging the CFD simulation capability in replicating the wind tunnel results difficult.

The general results show that the CFD simulations' static pressure tap results closely follow the wind tunnels' results. However, validation is limited due to practical errors such as model placement misalignments and faulty taps.

4.3.4. Comparison between Different Spanwise Locations

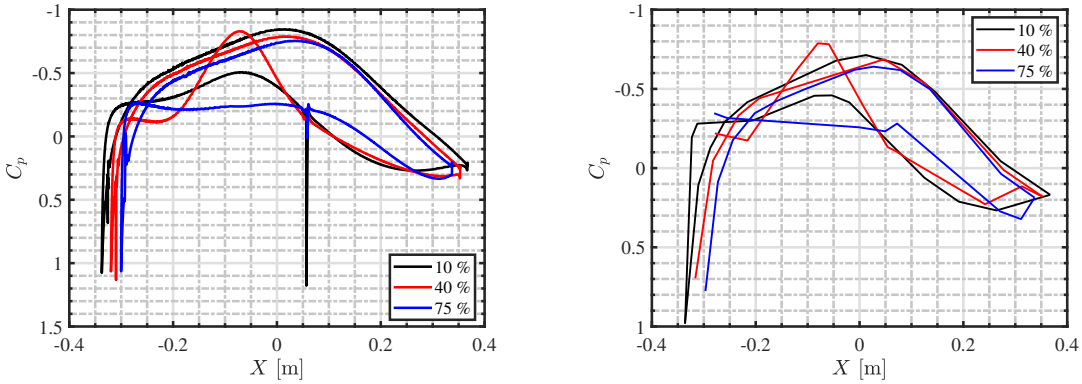

(a) CFD Wing Sections

(b) LTT Wing Sections

Figure 4.18: 0° Pressure Coefficient Distribution Comparison for Wing Sections

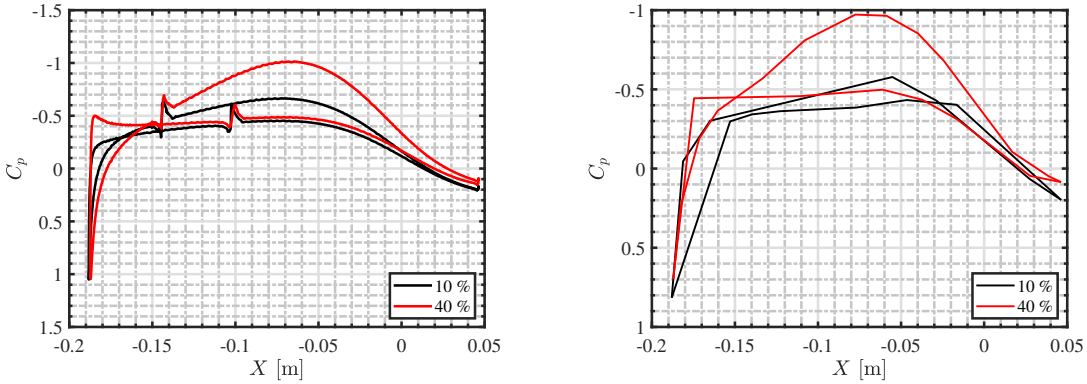

(a) CFD Strut Sections

(b) LTT Strut Sections

Figure 4.19: 0° Pressure Coefficient Distribution Comparison for Strut Sections

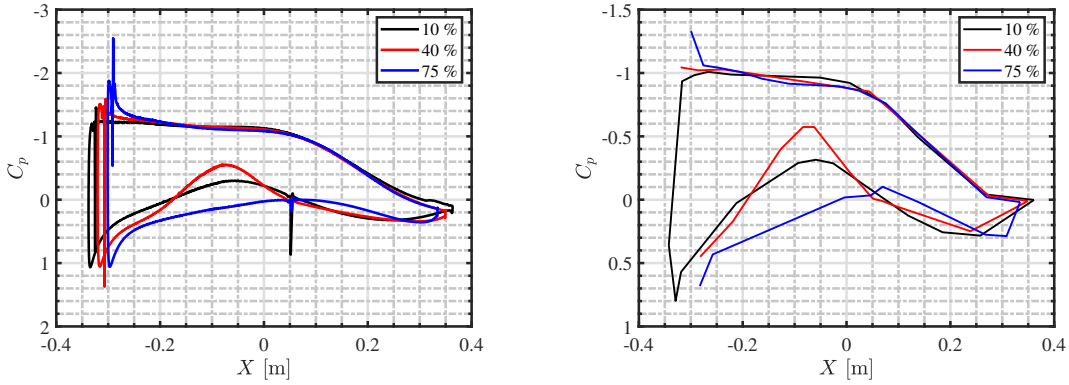

(a) CFD Wing Sections

(b) LTT Wing Sections

Figure 4.20: 6° Pressure Coefficient Distribution Comparison for Wing Sections

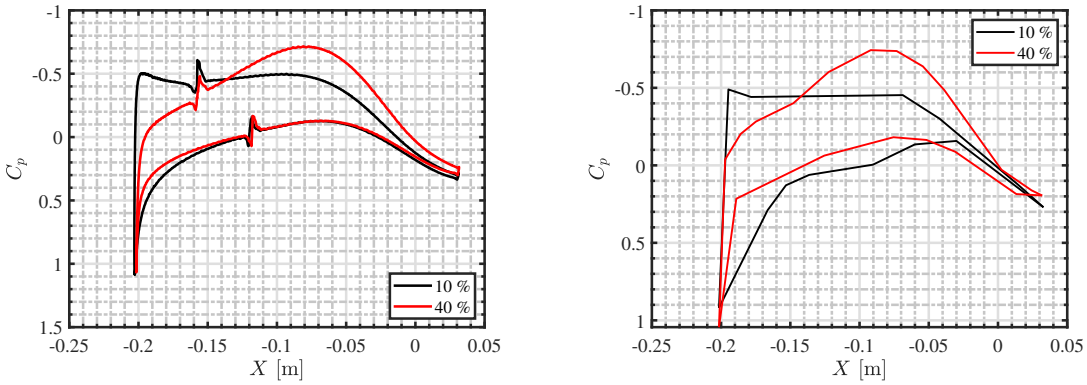

(a) CFD Strut Section

(b) LTT Strut Sections

Figure 4.21: 6° Pressure Coefficient Distribution Comparison for Strut Sections

An examination of Figures 4.18, Figure 4.19, Figure 4.20 and Figure 4.21 further reveals a clear correlation between the proximity of the strut to the wing and the resulting interference effects. As anticipated, the interference effect is most pronounced near the junction, reaching its maximum at approximately 40% of the span and in general, the numerical and experimental results are in agreement.

In summary, the static pressure analysis reveals that the CFD model underpredicts pressure on the wing's suction side, potentially due to model placement discrepancies. Conversely, the pressure distribution on the wing's pressure side aligns closely with experimental results. The strut's pressure distributions are well-matched between CFD and LTT data. Notably, the CFD model accurately captures the interference effects of the strut on both the wing's pressure side and the strut's suction side.

4.4. Wake Rake Results

In this chapter, the wake rake measurements conducted in the wind tunnel will be compared to corresponding data obtained from CFD simulations. The wake rake in the wind tunnel was positioned to traverse vertically across the span of the wing, recording dynamic pressure at various spanwise locations, with the rake being set up that the probes are concentrated at the junction region. This experimental setup allowed for measuring flow characteristics in the wake region behind the wing, offering further insight into the effectivity of PowerFLOW in capturing the vortices produced by the junction. A fluid slice was positioned at the same location as the wake rake probes (46.3cm behind downstream the wing root trailing edge) to replicate the LTT experimental setup. The virtual slice captured the time averaged fluid velocity data (to compute the dynamic pressure) comparable to that of the experimental probes, enabling a direct comparison between the two datasets. The chapter will present both the pressure coefficient fields captured by the wake rake and the corresponding simulated CFD dynamic pressure fields. Additionally, the integrated pressure coefficient, will be presented to gain a quantitative understanding of the CFD accuracy.

Examining Figure 4.22 and Figure 4.24, it becomes evident that the wake rake used in the wind tunnel experiments possesses considerably lower resolution than the CFD model. This disparity in resolution is particularly pronounced in Figure 4.24, where the CFD simulation more accurately captures the finer details of the wake structure (at 130mm and 180mm), whereas for the wind tunnel data, the effects of the wake vortices are completely washed out. The lower resolution of the wind tunnel data limits its ability to fully visualize the more minor flow features present in the wake.

A key observation from the experimental and CFD results is the discrepancy in the velocity deficit within the strut region. The CFD model consistently predicts a lower velocity deficit in the wake compared to the wind tunnel measurements. Specifically, the CFD results show a lower integrated pressure across the wake region, as illustrated in Figure 4.25 and Figure 4.23. This discrepancy could be attributed to an incorrect inlet velocity specification, which may also explain the deviations in trailing edge static pressures observed in Figure 4.14b.

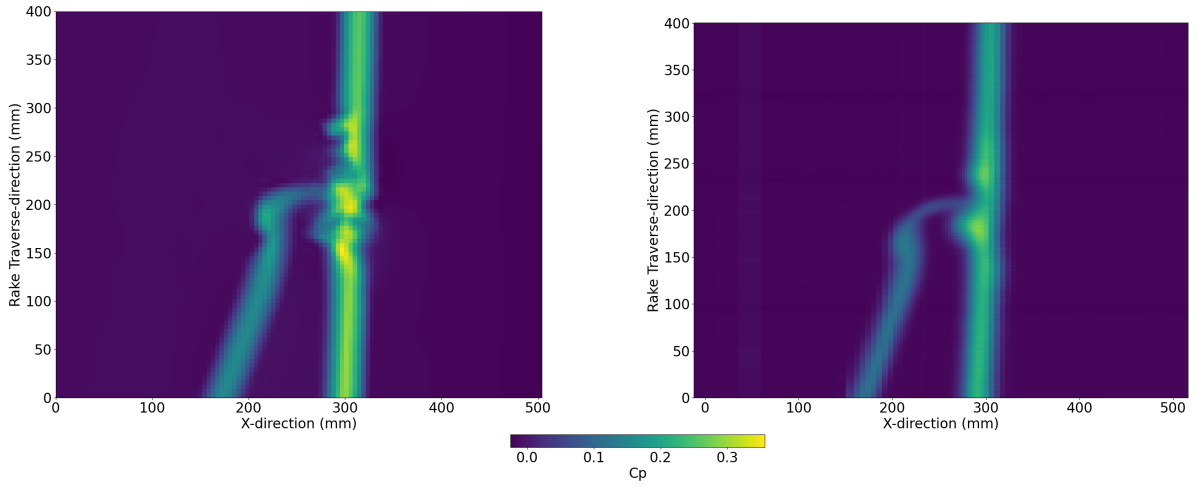

Figure 4.22: Heatmap of Wake Rake at 0 Degrees AoA (Left CFD, Right LTT)

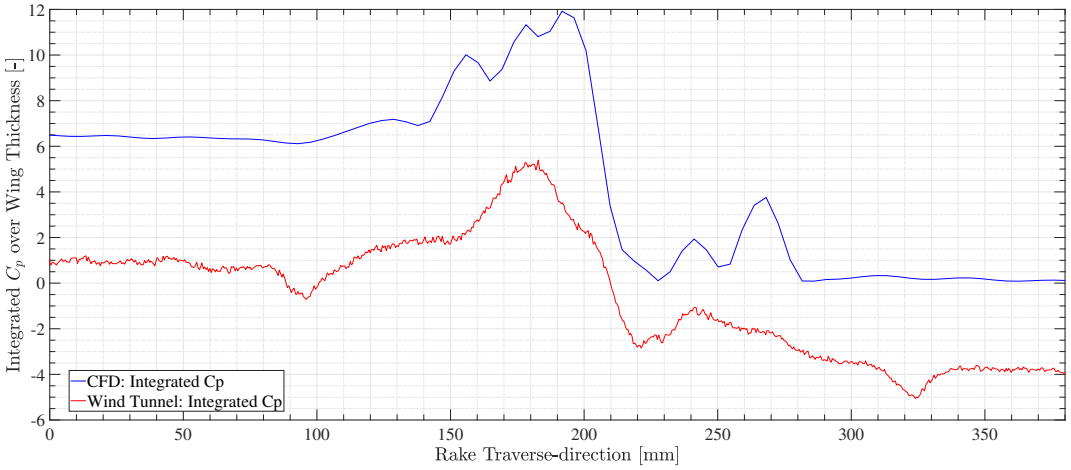

Figure 4.23: Pressure Coefficient integrated over wing thickness at 0 Degrees AoA

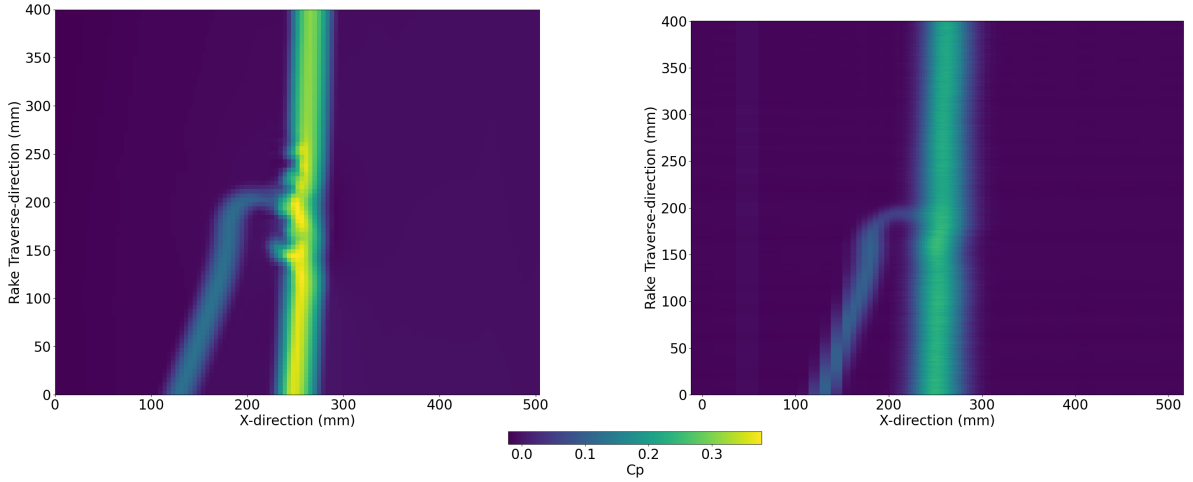

Figure 4.24: Heatmap of Wake Rake at 6 Degrees AoA (Left CFD, Right LTT)

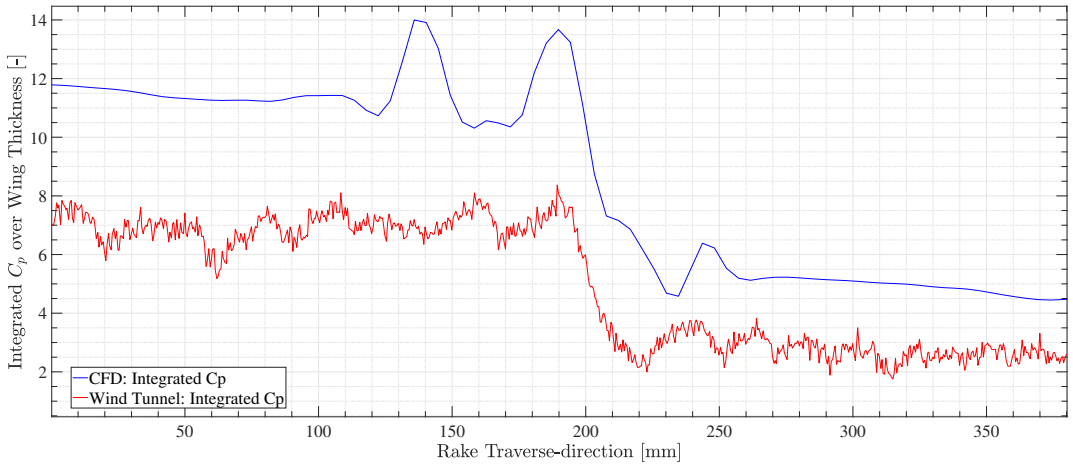

Figure 4.25: Pressure Coefficient integrated over wing thickness at 6 Degrees AoA

To quantify the differences in velocity deficit, consider the wing tip region. In the wind tunnel measurements, the maximum C_p was 0.19, corresponding to a local velocity of $u \approx 62.97\,\text{m/s}$, resulting in a velocity deficit of $7.03\,\text{m/s}$. In contrast, the CFD simulation produced a maximum C_p of 0.29, yielding a lower local velocity of $u \approx 59.17\,\text{m/s}$ and a larger velocity deficit of $10.83\,\text{m/s}$. This translates to a 10.04% velocity reduction from the freestream velocity in the wind tunnel, compared to a more significant 15.47% reduction in the CFD simulation. These findings suggest that the CFD model overpredicts wake effects relative to the wind tunnel results, or underpredicts the wake dissipation. This could be potentially due to the turbulence modelling discussed in Section 3.3.4. The trailing edge in the CFD model has not triggered the unsteady VLES mode, leaving the wake region predominantly characterized by the subgrid-scale model. Thus, the discrepancy may arise from modelling errors introduced by the subgrid-scale model.

Another important distinction between the two sets of results is the presence of vorticity effects in the wing's wake, particularly in the junction region. When comparing Figure 4.22 and Figure 4.24, it becomes apparent that the effects of vorticity in the junction wake are not as discernible in the wind tunnel data. However, in the CFD results, a clear spanwise region downstream of the junction exhibits significant vorticity effects. These effects play a role in developing the wake downstream of the wing, highlighting the increased sensitivity of the CFD simulation in capturing complex flow phenomena that may not be resolved in the experimental data. The vorticity in the wake region are under 3mm in diameters, however at its finest region, the rake spacing is also 3mm which does not make it fine enough to capture such effects, in regions more out of center, the wake reak spacing goes up to 24mm.

In summary, while the wind tunnel and CFD results demonstrate overall agreement, discrepancies in the magnitude of the velocity deficit, integrated pressure, and the apparent absence of vorticity effects in the wind tunnel data highlight the potential impact of interpolation on the accuracy of wake measurements and the modelling limitations of PowerFLOW. Although the higher resolution of the CFD model offers a more detailed representation of the wake, the accuracy of these results remains uncertain due to the reliance on the subgrid-scale model.

5

Unsteady Results

This chapter presents the unsteady results from the experimental and numerical tests. Specifically, the Taipro MiniP pressure sensors, the far field acoustic array output, and their beamformed results will be presented. The following results were obtained by operating the wing at a velocity of 50 ms^{-1}, chosen to mitigate the risk of failure of the melamine adhesive, at an angle of attack of six degrees.

5.1. Taipro Frequency Response

An experiment was conducted to determine the appropriate frequency range for analyzing the Taipro sensors under ambient conditions and with applied signal input. The signal input was generated using pressurized air, directed near the microphones to produce a measurable response without risking sensor damage. The recorded signal was subsequently processed to compute the relative frequency response. This analysis was performed using the following Python script.

The frequency domain for analysis was defined according to the sampling frequency; a frequency resolution was defined as 2 Hz for frequencies below 300 Hz and 50 Hz for those above 2000 Hz. These resolution values were chosen based on visual inspection to enhance the clarity of the Power Spectral Density (PSD) graphs. With these frequency resolutions, the necessary nfft values for Welch's method were computed to facilitate spectral analysis. Welch's method was then applied to each microphone dataset, computing the PSD separately for low- and high-frequency ranges.

The frequency resolution was incrementally adjusted within the transitional range of 300 to 2000 Hz to achieve a smooth transition between low and high frequencies, thereby ensuring a continuous spectrum. Following the analysis, the results from the low-, transitional-, and high resolution ranges were merged to produce a single PSD graph. The PSD values were then converted to decibel (dB) levels and normalized by subtracting each signal with its mean to align all microphones to provide a consistent baseline for straightforward comparison.

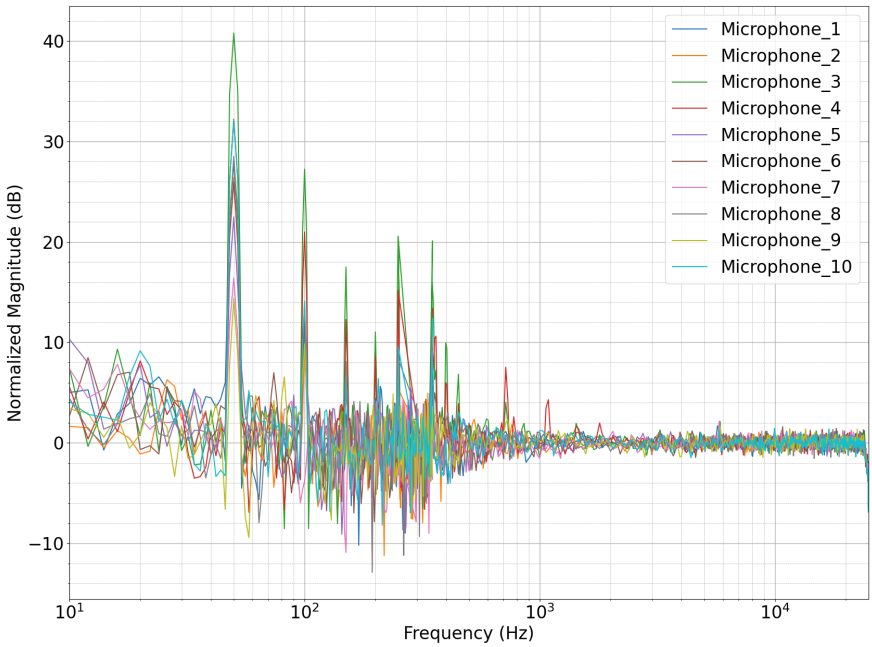

Figure 5.1: Frequency Response of Taipro sensors in Ambient Conditions

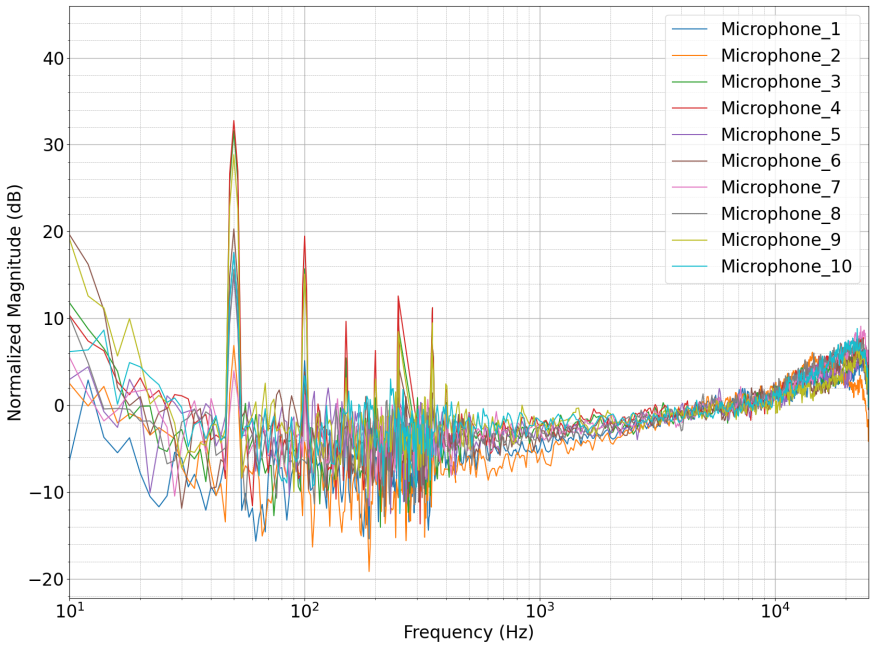

Figure 5.2: Frequency Response of Taipro sensors in Pressurized air conditions

Analyzing the frequency response, distinct harmonics were identified at 100, 150, 200, and 250 Hz. These peaks likely indicate electromagnetic interference from the electrical grid. The primary power frequency in the Netherlands is 50 Hz [50]. Nearby electronic equipment can emit electromagnetic noise at harmonics of this frequency, which the Taipro sensors may detect. These microphones can inadvertently act as antennas, introducing interference into the recorded signal. Furthermore, direct interference may arise through the power supply if insufficient filtering is not applied, allowing fluctuations

or harmonics of the power line frequency to propagate into the data.

Subsequent spectral analyses must account for these interference sources to prevent the misidentification of acoustic peaks unrelated to the strut-braced wing. Consequently, the Taipro sensors analysis focused on the frequency range of 100–2000 Hz. Although this range includes some of the aforementioned interference peaks, their presence does not preclude meaningful analysis, provided they are correctly identified and accounted for during data interpretation.

5.2. Unsteady Surface Pressure Measurements

9 Taipros surface sensors were employed to visualise the unsteady pressure fluctuations responsible for noise generation in the junction region that under the influence of the leading edge Horseshoe Vortex and the corner seperation. These regions were identified by the standard deviation of pressure extracted from the CFD simulations. Five sensors (of which sensor one was found to be faulty during wind tunnel tests) was placed along the leading edge of the junction to capture fluctuations associated with the leading edge horseshoe vortices. The last four sensors were positioned at the wake of the corner separation to monitor the associated pressure variations.

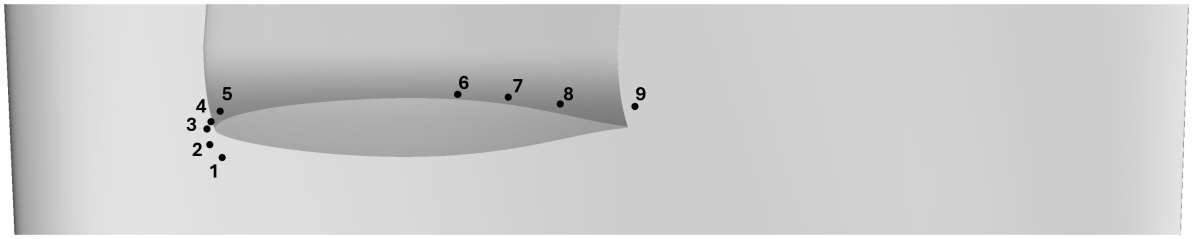

Figure 5.3: Taipro Pressure Sensor Locations (Flow Direction to the Right)

The CFD simulations replicated the Taipro sensors setup by having surface probes positioned at the exact locations of the physical sensors. The CFD results obtained pressure measurements, whereas the experimental sensors measured volts, which were converted to pressure using conversion charts provided by the manufacturer. These data were converted into Sound Pressure Level (SPL) graphs. Additionally, the Overal Sound Pressure Level (OSPL) was analysed to measure the total acoustic energy for each sensor. It represents the cumulative sound pressure level across the entire frequency range of interest. The importance of comparing the surface pressures lies in the FW-H analogy. As the wing surface is designated as the sampled surface, the surface pressure fluctuations are the direct sources of the junction noise sound. As such, for the CFD simulations to replicate the surface pressure distribution is essential in replicating the noise produced by the wing and, by extension, the noise propagated and received by the observer (microphone array).

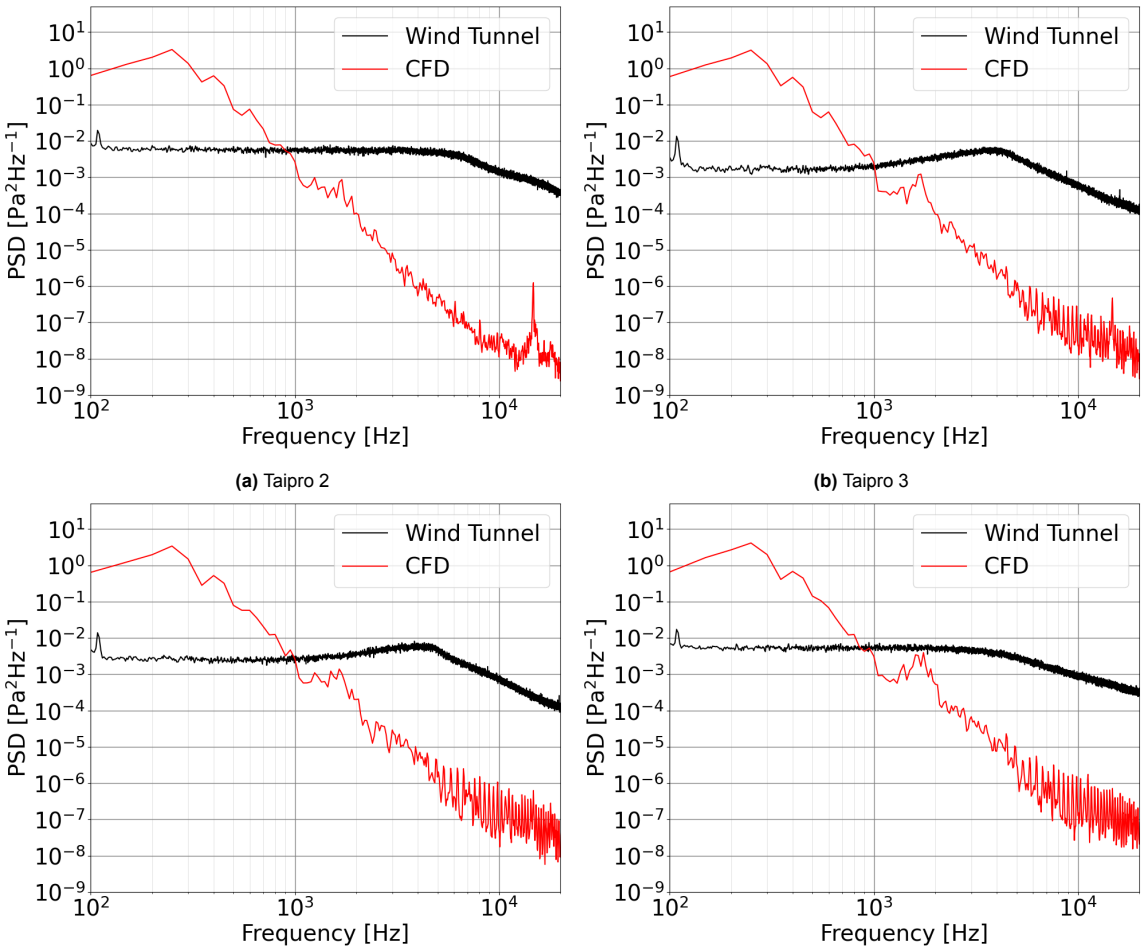

(a) Taipro 2

(b) Taipro 3

(c) Taipro 4

(d) Taipro 5

Figure 5.4: Spectral Density for Taipros at Stagnation Point

Figure 5.4 presents the sensors localized around the leading edge Horseshoe Vortex, revealing a stark contrast between numerical and experimental results. Firstly, a peak at 100 Hz is observed; the source of this peak remains uncertain. However, considering the findings from the microphone frequency response study, this may be an effect of electromagnetic interference, which could explain the absence of such a peak in the CFD results. Furthermore, for sensors 2 to 5, a noticeable hump is apparent at 4000 Hz for the experimental sensors, especially pronounced at sensors 3 and 4. This does not seem to be observed in the numerical data, nor is there any corresponding effect in the frequency response of the microphones in case it was due to a sensor response. The numerical data exhibits distinctly different SPD distributions compared to the experimental results. A peak is observed below 2 kHz and another at 15 kHz, especially for microphone 2. Such peaks seem absent in the experimental data; a clear explanation cannot be derived from them yet.

Additionally, the general PSD distribution of the CFD and LTT results diverge significantly, suggesting that the numerical model fails to accurately replicate the flow conditions near the strut surface. These differences may indicate distinct boundary layer characteristics between the CFD and LTT at the leading edge Horseshoe Vortex region. Thus, while the steady state results showed that the numerical model effectively captured the influence of the junction, this conclusion might not extend to the unsteady measurements.

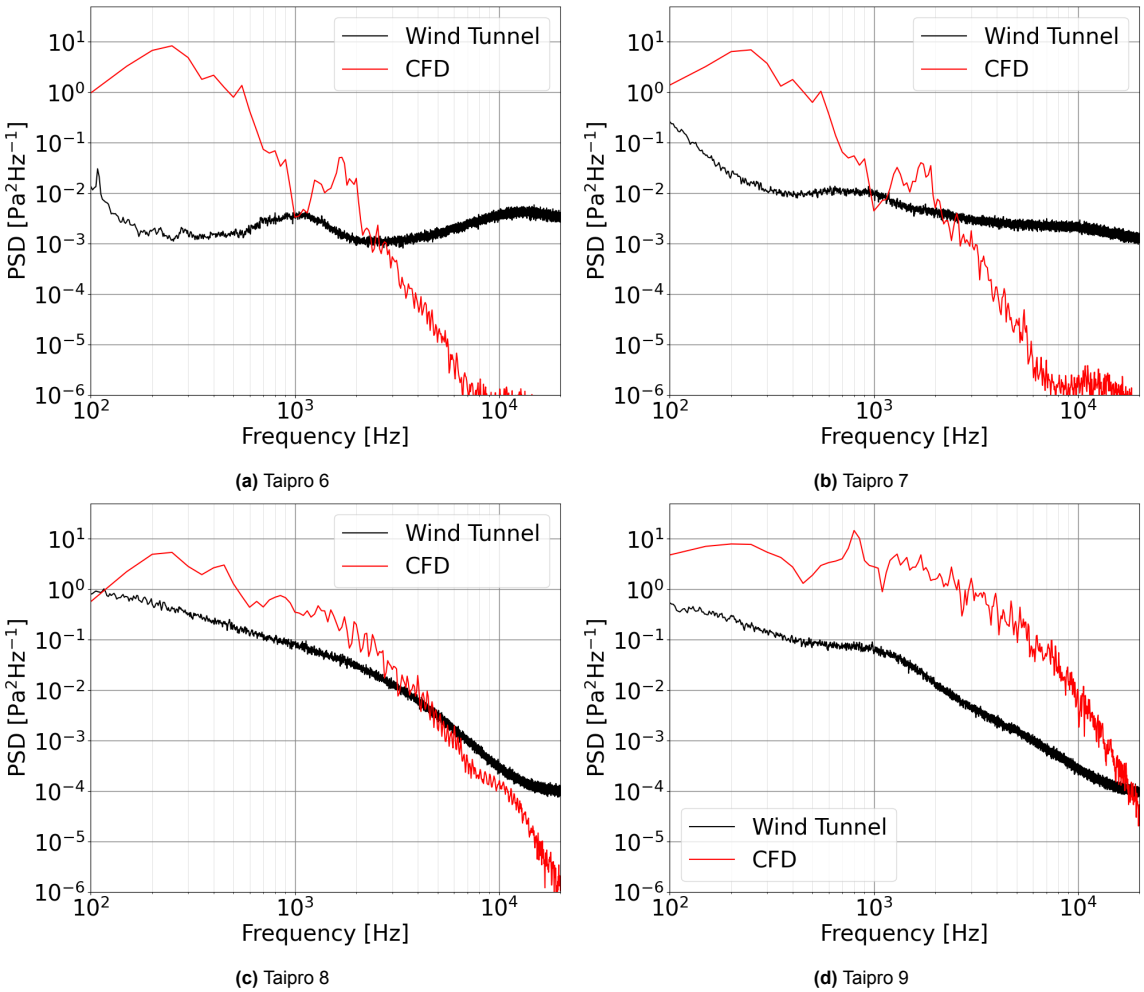

(a) Taipro 6

(b) Taipro 7

(c) Taipro 8

(d) Taipro 9

Figure 5.5: Spectral Density for Taipros at Corner Seperation

Figure 5.5, which shows the PSD of the sensors localized around the corner separation and wake region, displays a markedly different spectral characteristic compared to Figure 5.4. The area influenced by the corner separation shows larger magnitudes of pressure fluctuations. Furthermore, the 100 Hz peak observed in sensors 2 to 6 is no longer present for sensors 7 to 9, as the PSD values are greater. Interestingly, for the numerical results, the PSD profiles of sensors 6 and 7 closely resemble those of Figure 5.4, whereas sensors 8 and 9 exhibit a different spectral profile. This contrasts with the experimental results, where all sensors, except the last two, show markedly different spectral profiles. Among all sensors, 8 and 9, located in the wake of the corner separation, demonstrate the best agreement between CFD and LTT results. This might suggest that the boundary layer profiles of both methods align most closely in the wake of the corner separation, consistent with the flow visualization findings.

5.3. Spectral Analysis for Boundary Layer Characterization

A more detailed PSD spectral analysis is required better to understand the discrepancies between the numerical and experimental models. Specifically, semi-empirical models have been developed to characterise the turbulent boundary layer wall pressure spectra, offering insights into the PSD characteristics of turbulent flows. Notably, [13] compiled the findings of several semi-empirical models and established characteristic slopes for the PSD of turbulent boundary layers. Additionally, [1, 35] compared the PSD spectra of laminar and turbulent boundary layers, confirming similar characteristic slopes while highlighting differences between the two flow regimes. These findings provide a framework for identifying and comparing the boundary layer characteristics of both the numerical and experimental models.

A critical distinction between laminar and turbulent boundary layers is that they exhibit a more broadband nature, covering a wider frequency range in their PSD compared to laminar boundary layers, where most energy is concentrated within a narrower frequency band. This behaviour is evident in the PSD spectra of Taipro 2–7, as shown in Figure 5.4 and Figure 5.5. Generally, except Taipro 6 and 7, the experimental Taipros display fully broadband characteristics, indicative of a turbulent boundary layer. In contrast, the numerical results for sensors 2-7 exhibit a PSD spectrum that peaks within the 100–1000 Hz range before rapidly decaying, suggesting different flow characteristics.

Secondly, a common feature of laminar boundary layers is the presence of Tollmien-Schlichting waves. These waves are small-amplitude, streamwise-traveling disturbances that arise due to viscous instability and play a critical role in the transition from laminar to turbulent flow. Tollmien-Schlichting waves typically appear as narrowband (covering a small frequency range) peaks in the PSD of surface pressure measurements. Such peaks can be observed in Figures 5.4a and 5.4b at approximately 15 kHz, which may point to the local boundary layer being laminar.

Finally, and most concretely, [13] describes how the turbulent boundary layer region can be divided into regions with characteristics PSD slopes as shown in Figure 5.6:

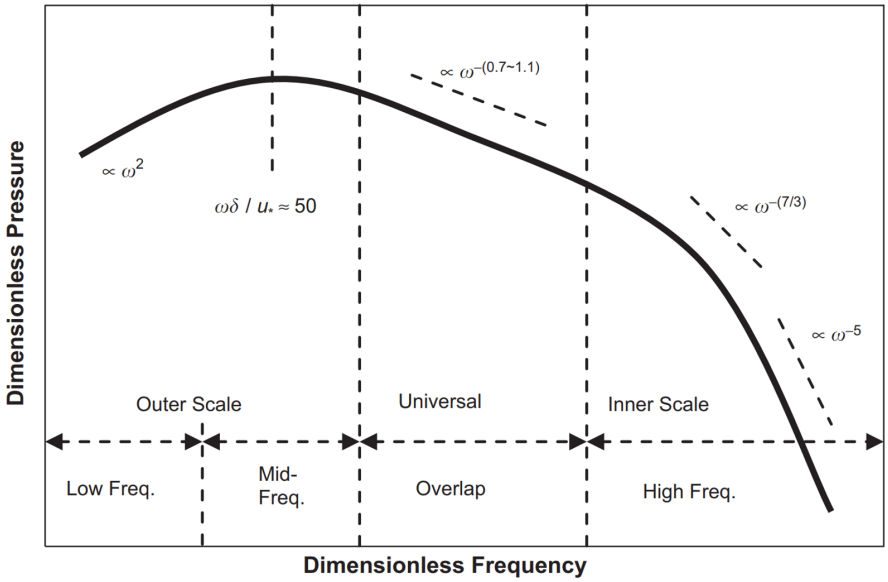

Figure 5.6: Overview of the spectral features of a turbulent boundary layer wall pressure spectrum across various frequency bands. [13]

The slopes observed in the Taipro findings, as presented in Figure 5.7, provide insights into boundary layer characteristics. Focusing first on Figure 5.7a, which corresponds to the region near the leading-edge Horseshoe Vortex, the experimental PSD aligns well with the characteristic spectral slopes, suggesting a turbulent boundary layer. In contrast, the CFD PSD does not conform to these characteristic lines; instead, it exhibits a steeper decay, approximately following a f^{-6} slope. This behaviour, combined with the potential presence of Tollmien-Schlichting waves discussed before, and the non-broadband nature of the PSD, indicates that the CFD boundary layer in proximity to the leading-edge Horseshoe Vortex might be laminar. In comparison, the experimental PSD, which does not show the presence of Tollmien-Schlichting waves and displays more broadband characteristics while conforming to the characteristic lines, might suggest a turbulent boundary layer.

In Figure 5.7b, which corresponds to the wake of the corner separation, the experimental results continue to conform to the characteristic spectral lines. In contrast to Figure 5.7a, the CFD results at this location do not exhibit any evidence of Tollmien-Schlichting waves. Additionally, the energy distribution in the CFD PSD is more broadly spread, consistent with the behaviour of a turbulent boundary layer. Moreover, the PSD of the numerical model aligns more closely with the characteristic lines compared to the results shown in Figure 5.7a (though still to a lesser degree compared to LTT results). These

observations might suggest that the boundary layer at the location of Taipro 8 is likely turbulent for both the numerical and experimental models.

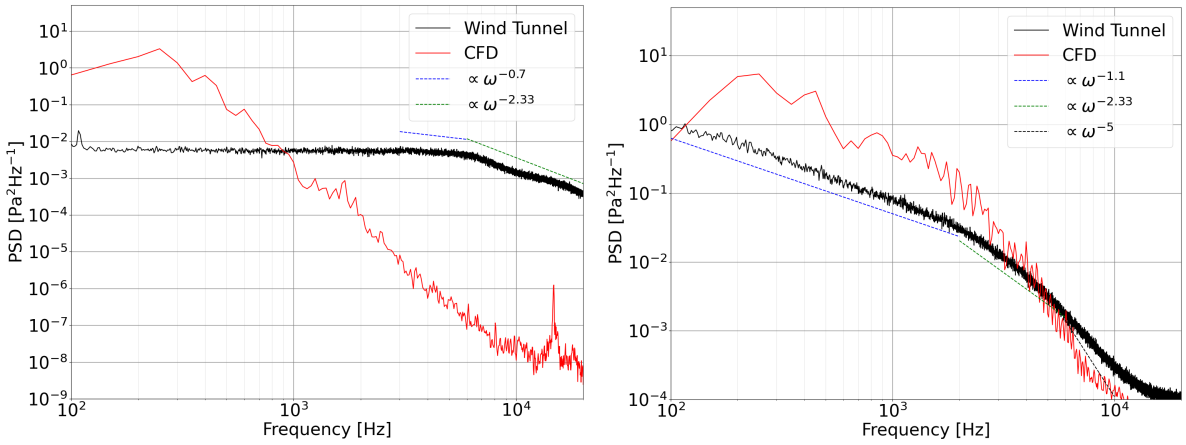

(a) PSD of Taipro 2

(b) PSD of Taipro 8

Figure 5.7: Comparison of PSDs for Taipro 1 and Taipro 8 With Turbulent Boundary layer characteristics slopes

To investigate the potential causes of the discrepancies at Figure 5.4a, refer to Figure 5.3. Sensors 2–5, which were positioned adjacent to the saddle point to maximize the likelihood of capturing data from the region around the saddle point. However, factors such as Reynolds number and angle of attack, the latter of which was adjusted post-testing as discussed in Section 4.1, influence the Horseshoe Vortex ”vortex core” location and the position of the saddle point, which is where the leading-edge Horseshoe Vortex effectively begins. Furthermore, Section 2.1, particularly Figure 2.2, highlights that the leading-edge Horseshoe Vortex region can be subdivided into low and high shear stress zones, each affecting boundary layer characteristics differently. Laminar boundary layers typically form in low-shear stress regions, while turbulent boundary layers arise in high-shear stress zones. These discrepancies may suggest that the vortex core in the numerical model may be positioned relatively closer to the junction surface than in the experimental model, resulting in the sensors being located in a low-shear stress region. This could explain deviations in how the junction flow is captured between the numerical and experimental results.

Sensors 8 and 9 are not directly influenced by the leading edge Horseshoe Vortex region and its distinct high- and low-shear zones. Moreover, as highlighted in Section 4.2, the numerical model visually aligns with the experimental results from IR and oil flow visualizations in accurately resolving the wake of the corner separation, which reduce doubts of placement errors. The results in Figure 5.7b further corroborate these observations as one would expect turbulent boundary layer in the wake of the corner separation.

The analysis, however, cannot be extended to all sensors. Specifically, Taipro 6 and 7, shown in Figure 5.5a and Figure 5.5b respectively, do not exhibit PSD spectra characteristic of a turbulent boundary layer. Therefore, their flow state cannot be conclusively identified as turbulent. Nor do they have PSD distributions characteristic of laminar flows. Positioned between the corner separation vortex and the leading-edge Horseshoe Vortex, these sensors display spectra that do not align with either laminar or turbulent flow behaviour, complicating and limiting the understanding of the behaviour of the junction surface.

5.4. OSPL Comparisons

To further investigate the discrepancies between the CFD and LTT results, one can examine the OSPL values. OSPL quantifies the total acoustic energy across a specified frequency range. Its calculation is based on a script similar to that used for Welch spectral analysis. The process began by loading and preprocessing time and pressure data from each Taipro sensor. The script then computed the PSD for each microphone’s signal using Welch’s method. A frequency mask was subsequently applied to

filter out energy outside the analyzed range of 200–20,000 Hz. Finally, OSPL values were calculated by integrating the PSD within the specified frequency range as seen in Figure 5.8.

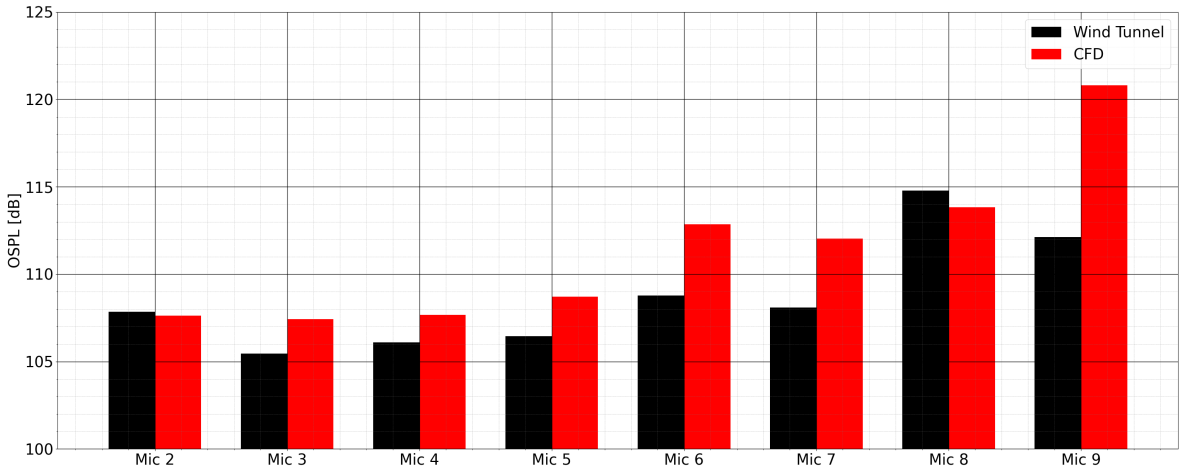

Figure 5.8: OSPL Values for each Taipro Sensor

The OSPL values in Figure 5.8 illustrate apparent differences between the wind tunnel and CFD results across sensors 2 to 9. In both datasets, sensors 8 and 9 consistently record the highest OSPL levels, indicating that the corner separation region might be a dominant acoustic energy source.

However, a notable distinction arises when comparing the trends between the wind tunnel and CFD data. In the wind tunnel measurements, there is a more abrupt increase in OSPL between sensors 7 and 8, emphasizing a sharp increase in noise intensities between the regions influenced by the leading edge Horseshoe Vortex and the corner vortex. Conversely, the CFD results show a more gradual increase in OSPL across all sensors, with less distinction between these two regions. This could be associated with the PSD characteristics of both models. In the experimental data, distinct differences in PSD behaviour are observed across sensor groups 2–6, 6–7, and 8–9. In contrast, the CFD PSD spectra for sensors 2–7 exhibit similar shapes, with notable differences only appearing for sensors 8 and 9. However, this does not fully explain why sensors 7 and 8 display comparable OSPL values, while sensor 9, which is expected to exhibit turbulent behaviour similar to sensor 8, records a significantly higher OSPL.

Furthermore, except for sensors 2 and 8, the CFD consistently predicts higher OSPL values compared to the wind tunnel data, with the most significant deviation being 8.6dB (which is a relative acoustic energy change of 7.26 times) at sensor 9, the best similarities are found in sensor 2 where the difference is -0.22dB (a relative change in acoustic energy of 1.05 times). This result contrasts the previous findings, where the PSD for sensor 2 indicated differing boundary layer characteristics between the experimental (laminar) and numerical (turbulent) models. In contrast, sensor 8, and to a lesser extent sensor 9 was predicted to have similar boundary layer behaviour. However, these observations imply that matching boundary layer characteristics do not necessarily correlate with acoustic intensity.

5.5. Far Field Acoustic Analysis

5.5.1. Computational Aeroacoustic Analysis Methods

As mentioned, two acoustic measurement techniques are available within PowerFLOW: Direct Noise Computation and the FW-H acoustic analogy.

The first method, Direct Noise Computation, involves directly sampling the pressure fluctuations in a fluid cell (voxel) generated by the wing and tunnel at specified microphone locations. This technique processes the sampled noise data without a seperate model that accounts or further processes propagation of noise from the noise source and nor does it allow the user to select the surfaces that emit noise. This is because the measurements are recorded in the listener's reference frame directly. This approach, which reduces the need for data transformations, imposes requirements on mesh resolution.

Specifically, a finer volume mesh is required to accurately capture the propagation of sound waves over large distances without a loss due to dissipative errors.

Conversely, the second method employs the FW-H acoustic analogy for Far-Field Analysis. Recalling section 2.2, pressure fluctuations on the surfaces of noise sources are sampled and subsequently propagated to the far field. This method alleviates the need for a fine-volume mesh. However, this method (along with the Direct Noise Computation method) necessitates a surface mesh of sufficient refinement to to make sure the correct noise is emitted by the sampled surface.

An important consideration of the method is the influence of the wall in the test section. Direct noise computations sample the noise of a voxel irrespective of its sources; therefore, receive produced by the walls. In contrast, using the FW-H analogy, the microphone captures noise generated by the sampled surface, including reflections from other surfaces of the original noise source.

To perform the direct noise computation, a volume covered the area of the microphone array, which is one voxel thick and offset from the tunnel walls by one voxel. This volume measured the pressure fluctuations and is sampled at the location of each respective microphone.

For the FW-H analysis, the solid formulation was used, and the wing and strut are the surfaces that got sampled. This surface measured the pressure fluctuations and was then processed using the PowerACOUSTICS far-field analysis tool.

5.5.2. Spectral Profile Analysis

This section will compare the spectral densities of each acoustic measurement method. The analysis focuses on microphone 57 of the array shown in Figure 3.8. Microphone 57 was centrally positioned within the microphone array and located directly in front of the wing-strut junction.

Figure 5.9 presents the SPL spectra for the LTT, Direct Noise Computation, and FW-H methods. Upon examining the LTT data, a distinct peak at 100 Hz is observed, which is absent in both numerical methods. The origin of this peak remains unclear and requires further investigation to determine whether it is due to instrumentation effects, flow phenomena or tunnel interference effects. Additionally, the LTT data consistently exhibits lower SPL levels than the numerical results across the frequency spectrum. Within the 200-1000Hz spectrum, both numerical models have consistently larger SPL values than the experimental model, at some points by a difference of 20dB, corresponding to a relative intensity change of 100 fold. The beamforming analysis in Section 5.6.2 will analyse where the noise source originates from.

The Direct Noise Computation and FW-H spectra exhibit consistent behaviour in the 200–3000 Hz frequency range, indicating similar noise predictions within this domain. However, the two methods diverge significantly above 4 kHz. While this could suggest that the observed deviations are wall-induced, noise from tunnel walls typically dominates in the low-frequency range, casting doubt on this explanation. Consequently, further analysis is required to understand better the discrepancies observed in the Direct Noise Computation results.

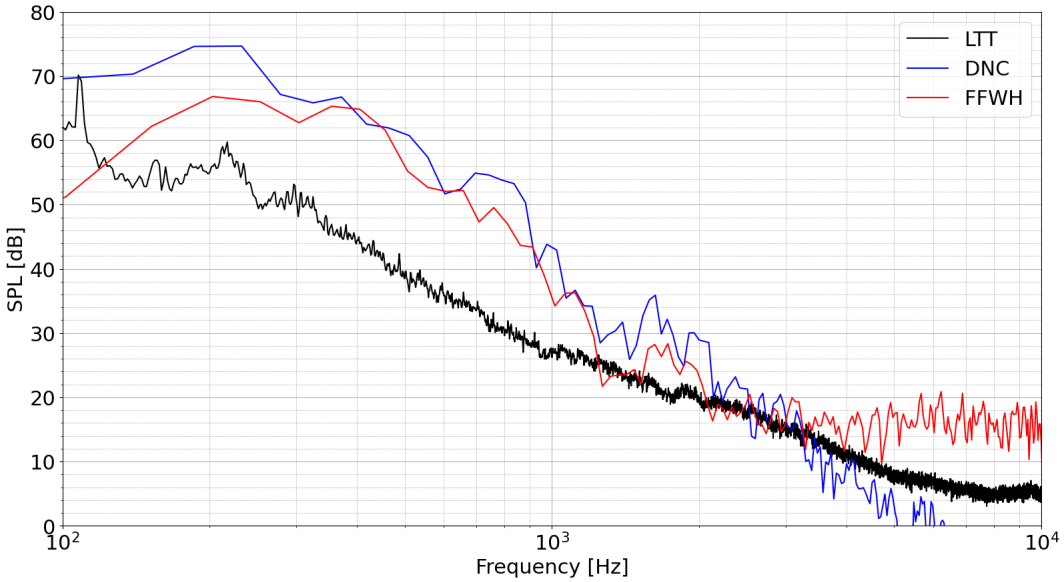

Figure 5.9: Comparison of SPL Values For Mic 57

5.6. Beamforming

5.6.1. LTT Array Resolution

Acoustic measurements were conducted in the LTT using a far-field microphone array to validate the CFD model's acoustic predictions. Beamforming analysis is presented to evaluate the acoustic results obtained during the wind tunnel tests. Before conducting this analysis, it is essential to understand the array's capabilities and the limitations that may influence the outcomes. A key consideration is the spatial resolution of the scan grid, which provides insight into the array's ability to separate distinct noise sources. This analysis determines whether closely spaced sources might be merged into a single source due to the array's size. To assess this, the Rayleigh criterion, as introduced in Section 2.5.4, is applied. The distance from the scangrid and speed of sound are known inputs, and the array aperture is portrayed in Figure 5.10.

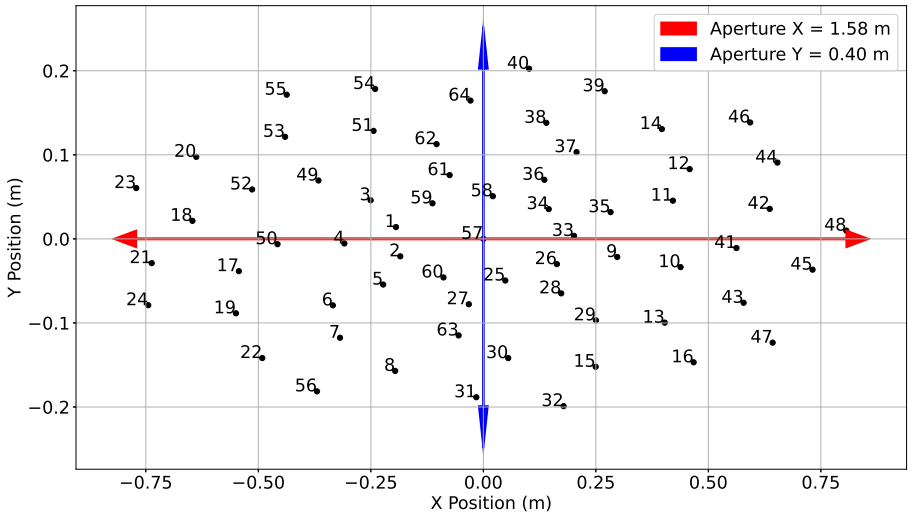

Figure 5.10: Array Aperture

With this the Rayleigh criterion for three different seperation lengths are computed as below

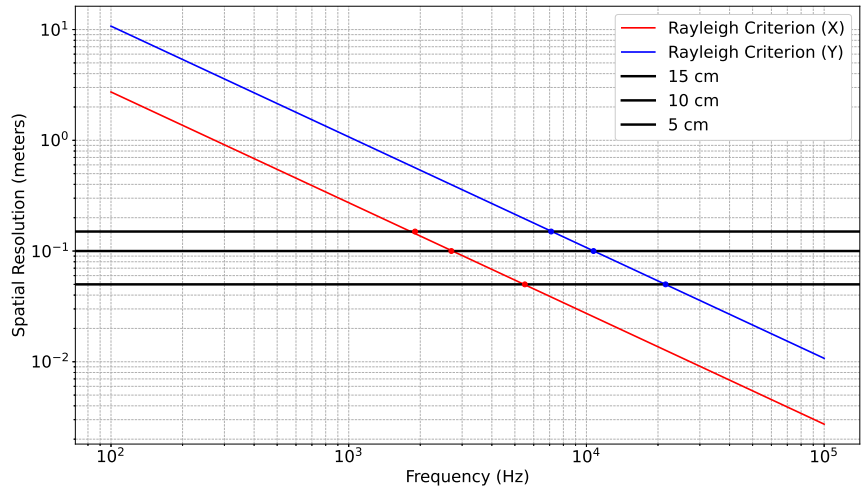

Figure 5.11: Rayleigh Criterion for Different Resolutions

The 15 cm resolution line's intersection occurs at 1901.80 Hz in the X direction and 7107.01 Hz in the Y direction. The intersection for the 10 cm horizontal line corresponds to a frequency of 2702.61 Hz in the X direction and 10710.62 Hz in the Y direction. Lastly, the 5 cm horizontal line intersection is observed at 5505.41 Hz in the X direction and 21521.44 Hz in the Y direction. It is important to note, however, that while the Rayleigh criterion indicates limited resolution at low frequencies (specifically below 1000 Hz), this does not preclude the possibility of conducting beamforming analysis at those frequencies. As shown in Section 5.6.3, it remains feasible to spatially locate noise sources within these frequency regimes, though the fidelity of the results is significantly reduced.

In addition, the spatial Nyquist frequency is calculated as per 2.5.4. This indicates the maximum frequency in order to avoid spatial aliasing during beamforming. As the LTT array microphone distribution is not evenly spaced, the array is subdivided into an inner and outer region:

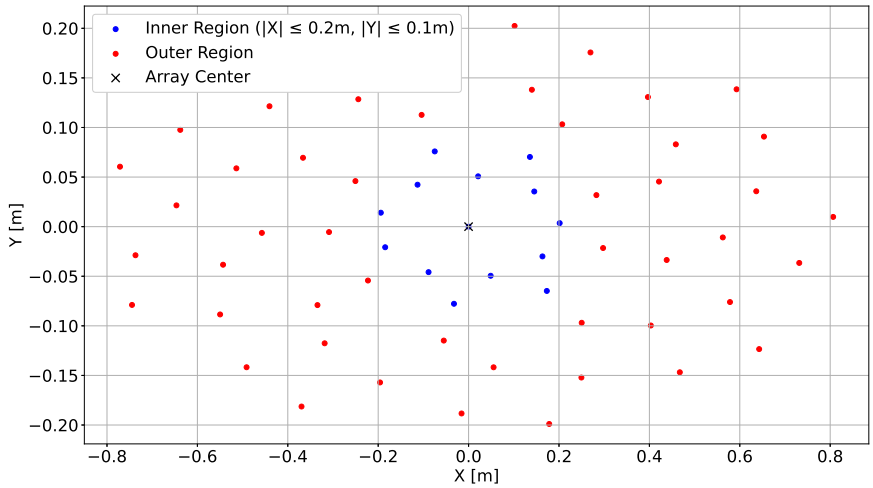

Figure 5.12: Division of Array For Nyquist Analysis

The average microphone spacing is computed for each region, and then the Nyquist frequency is calculated. The average microphone spacing in the inner region (which encompasses the wing strut interface) is 0.048 m, while in the outer region, it is 0.072 m. The maximum Nyquist frequency for the inner region is 3555.17 Hz, with an associated minimum wavelength of 0.096 m, representing the finest spacing that can be achieved. In the outer region, the maximum Nyquist frequency is 2387.40 Hz, corresponding to a minimum wavelength of 0.144 m.

From this, it can be seen that it is unattainable to beamform the acoustic measurements without either the production of sidelobes or the merging of separate acoustic sources. However, except for the junction region, most acoustic sources are separated by large distances, and the production spatial aliasing does not impede on analysis. As such, though the Rayleigh and Nyquist criterion makes it impossible to produce a true noise heatmap without aliasing or sources merging, it is still possible to perform beamforming analysis while being aware of the error sources.

5.6.2. Beamforming Results

The signal response of the 57 microphone array was further processed to obtain further insight into the acoustic field of the test section. This process was only applied for the FW-H model, as the direct noise computation model did not have the acoustic lining, rendering the model not reflective of the testing conditions.

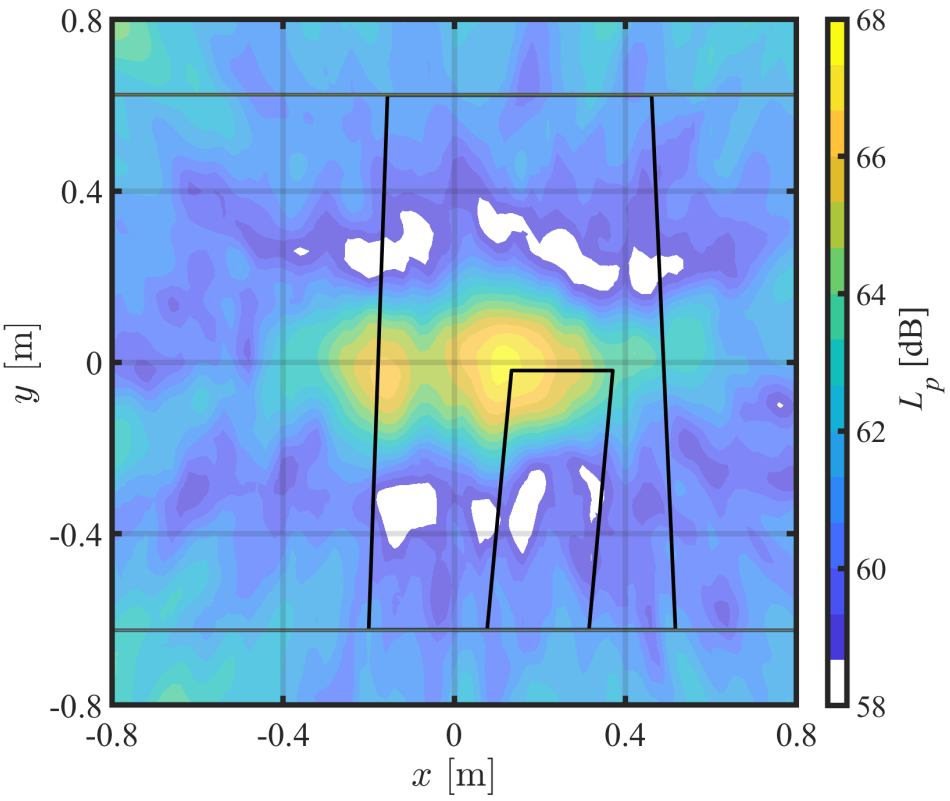

Figure 5.13: FW-H Beamformed Heatmap For Junction Region (f = [2080,10000] Hz)

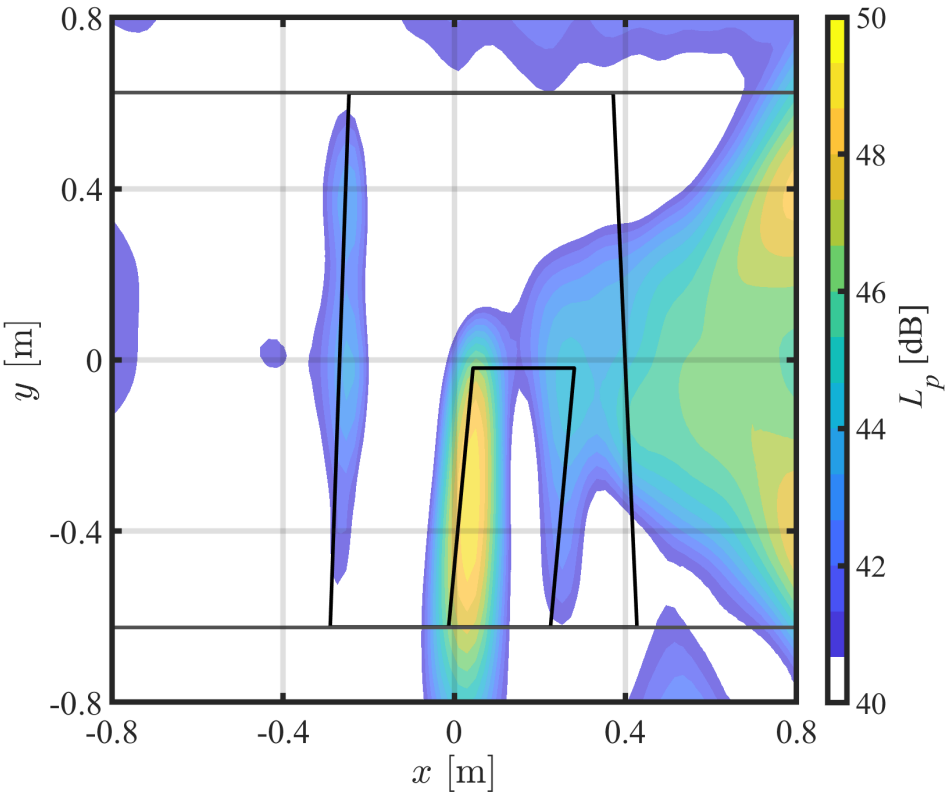

Figure 5.14: LTT Beamformed Heatmap For Junction Region (f = [2080,10000] Hz)

Analysis of the wind tunnel results reveals that noise from the wind tunnel heavily influences the test section. This noise dominates the low-frequency range, where wing trailing edge noise is typically expected. However, in the beamforming code, its possible to not include this frequency range during the calculation of the heatmap, and as a result, trailing edge noise from the strut and the wing can be recognized at higher frequencies, where the harmonics of this noise source become visible without interference from the tunnel noise. However, further analysis should be performed to isolate the wing and strut trailing edge noise from the tunnel walls.

Additionally, the wind tunnel data indicates that noise generated by the strut's trailing edge dominates the 2080–10,000 Hz frequency range. At these frequencies, it is the only clearly identifiable noise source within the strut-wing system, with the wing's trailing edge contributing significantly less acoustic energy. This starkly contrasts the CFD results, where the FW-H analysis identifies the junction region as the primary noise source and fails to capture noise contributions from the trailing edges of the wing and strut.

A potential explanation for the observed discrepancies lies in the limitations of the VLES model employed by PowerFLOW discussed in Section 3.3.4. Consequently, the junction refinement region remains the only area with resolved unsteady flow in the simulation, corresponding directly to the dominant noise source identified in the CFD beamforming data. The inability to resolve large turbulent structures near the strut and wing trailing edge might cause an underrepresentation of surface pressure fluctuations and critical acoustic sources sampled on the wing's surface using the FW-H analogy. These large-scale structures generate unsteady aerodynamic loads, driving pressure oscillations that radiate as sound. When these scales are not adequately resolved, the simulation becomes overly reliant on the subgrid-scale model, which dissipates the vortices and may underestimate surface pressure fluctuations, leading to a loss of essential acoustic source information. This limitation likely contributes to the CFD overestimating noise in the junction region while underestimating it at the wing's trailing edge.

Furthermore, as illustrated in Figure 5.8, the beamformed CFD data aligns with the Taipro surface pressure measurements, consistently exhibiting higher OSPL values compared to the wind tunnel data. While this may not contribute as significantly to the discrepancies as the turbulence modeling limitations, it shows that the FW-H model propagates surface pressure fluctuations of greater intensity than those observed in the experimental setup, leading to a louder predicted noise signal at the junction region.

5.6.3. Isolating Wing & Strut Trailing Edge Noise

Based on the findings from the beamformed data, it is interesting to conduct a sensitivity test on the impact of noise originating from the strut and wing trailing edges. Noise generated by the wing and strut typically emanates from the trailing edge and dominates specific frequency ranges, depending on each component's geometric size and flow structures. To support this analysis, the beamforming code includes functionality that defines a specific region within the scan grid (called integrated scan grid) and calculates a weighted SPL for that area. As illustrated in Figure 5.15, the integrated scangrid can be isolated to enable localized spectral analysis. By examining multiple integrated scan grids that progressively encompass larger spans of the wing and strut trailing edges, it becomes possible to isolate the contributions of individual noise sources. As the integrated scan grid size increases, the overall contribution of trailing edge noise sources is expected to become more prominent, thereby aiding in identifying the frequency domain of the locally dominant noise source.

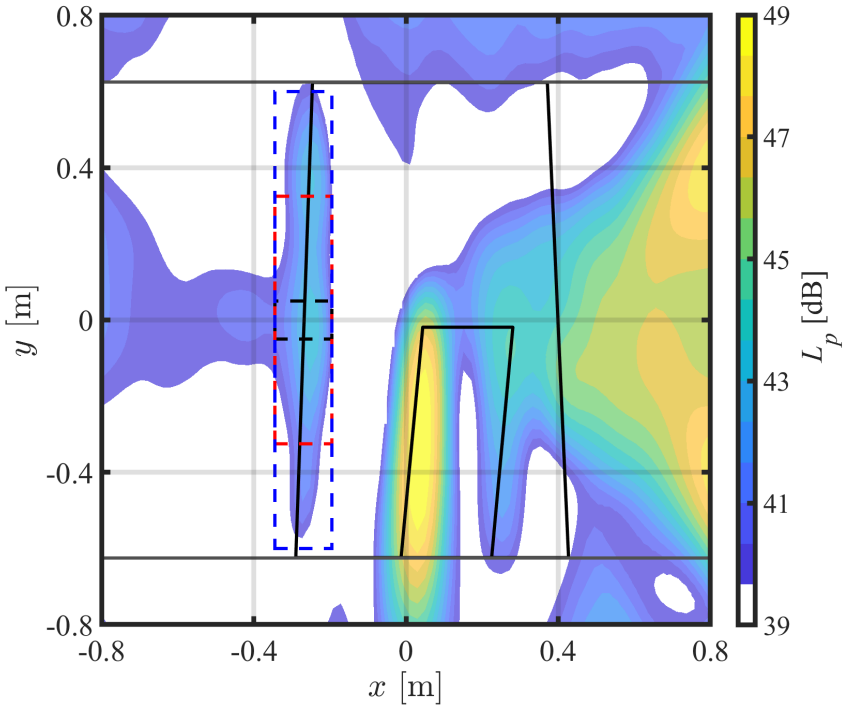

Figure 5.15: Wing Heatmap with Increasing Integrated Scangrids (f = [2000,7000] Hz)

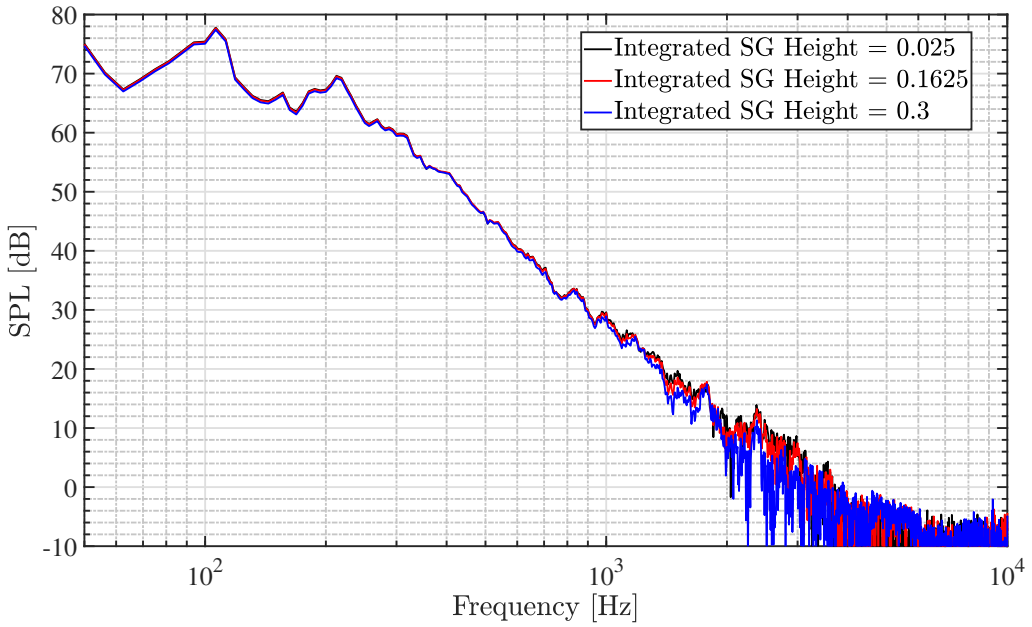

Figure 5.16: Wing Trailing Edge SPL For Varying Integrated Scangrid Sizes

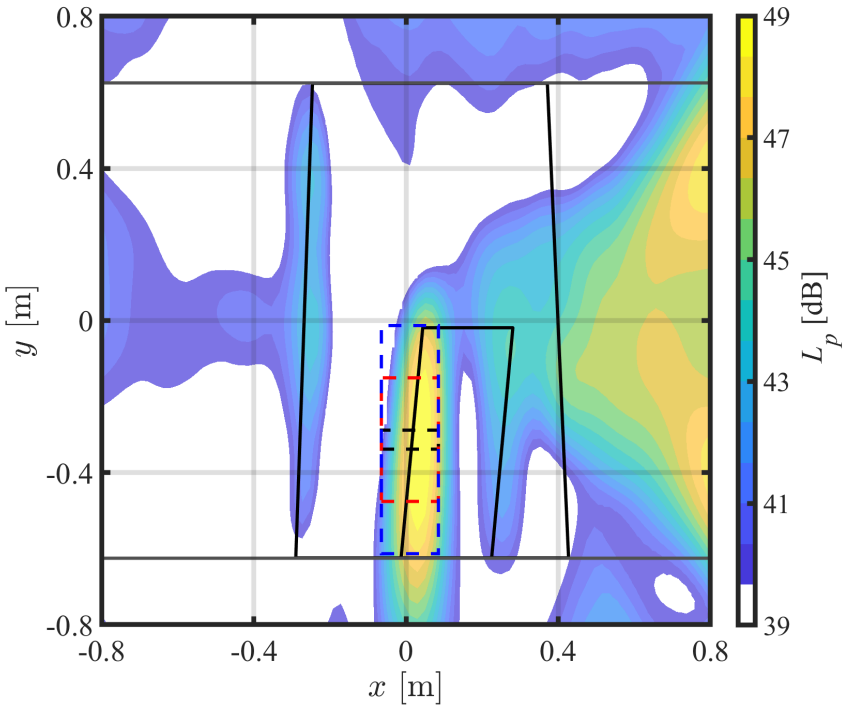

Figure 5.17: Strut Trailing Edge Heatmap with Increasing Integrated Scangrids (f = [2000,7000] Hz)

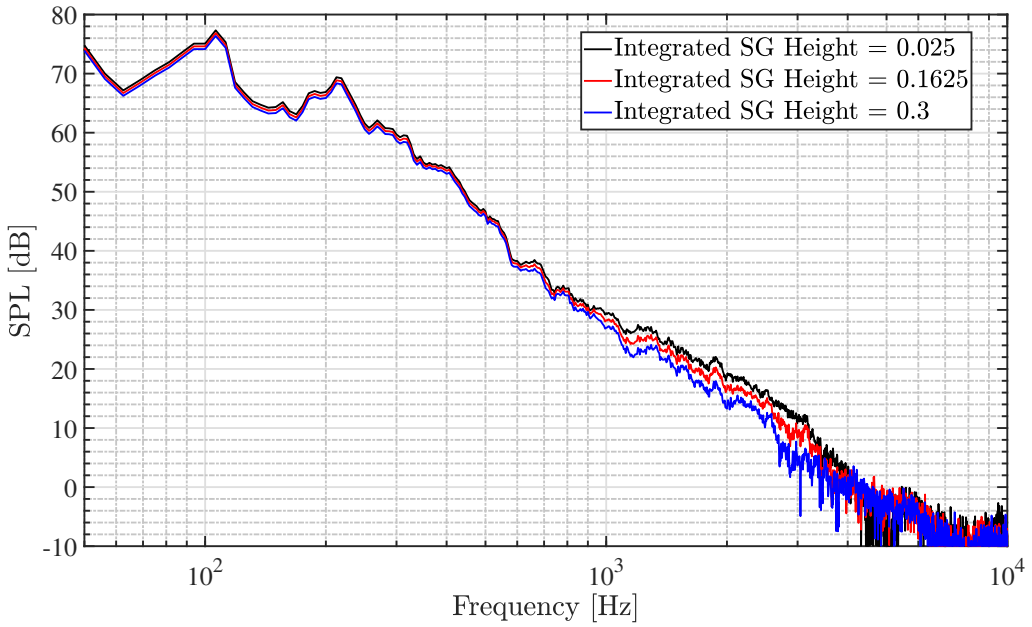

Figure 5.18: Strut Trailing Edge SPL For Varying Integrated Scangrid Sizes

Two key findings emerge from this analysis. Firstly, the spectral densities remain consistent within the 0–1000 Hz frequency range. Secondly, an increased integrated scan grid area corresponds to a slight decrease in SPL values. This outcome is unexpected, as an expanded scan grid would typically capture a larger area, leading to a constant or increased contribution from noise sources. This unexpected reduction is likely attributable to the monopole assumption employed in the scangrid integration computation, which becomes invalid when the noise source extends beyond the scan grid boundaries, this effect has been researched by [8] and gives light to potential further improvement for the beamforming analysis. Furthermore, the nature of the lack SPL variations for the differing integrated scangrids suggests the presence of a dominant noise source under 1kHz that overshadows other potential contributors. This hypothesis can be further substantiated by beamforming targeted sections of the previously observed unchanging low broadband frequency hump.

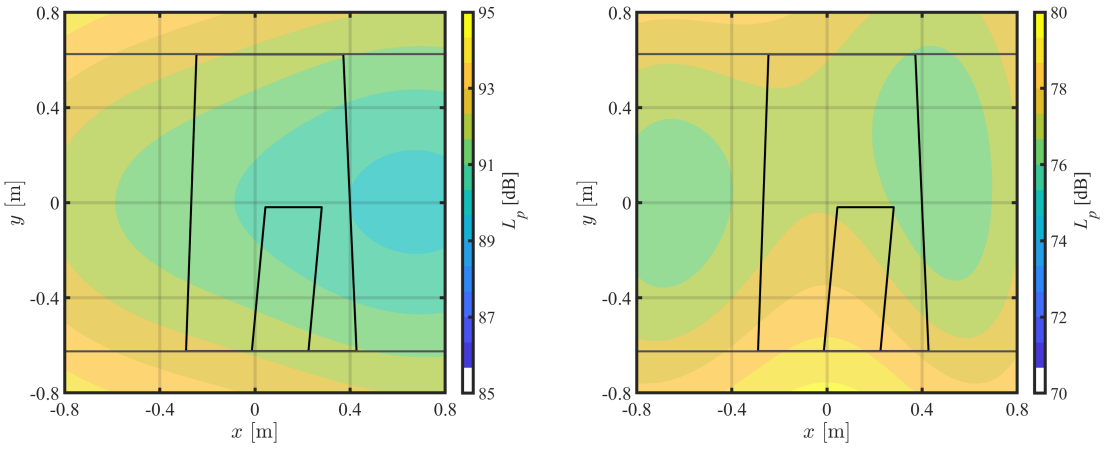

(a) Diffusor Noise Effects (f = [100,1000] Hz)

(b) Wall Reflection Noise Effects (f = [300,1000] Hz)

Figure 5.19: Beamformed Sound Source Heatmaps for Diffusor and Reflection Effects

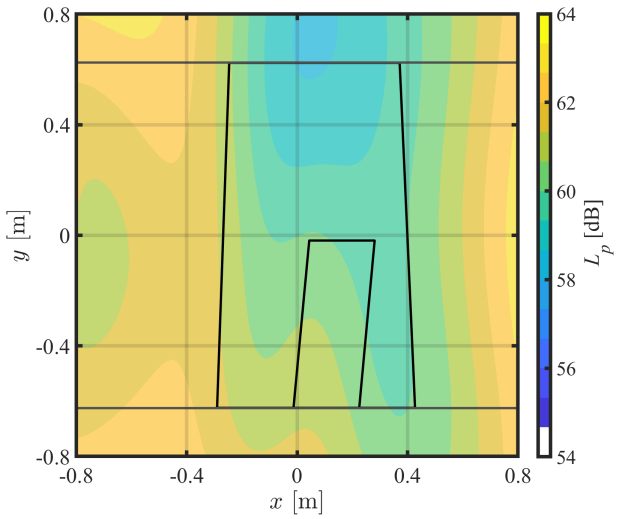

Figure 5.20: Inlet Noise Effects (f = [600,1000] Hz)

The figure above reveals the presence of three dominant noise sources. First, the Figure 5.19a shows the diffuser emerges as the primary noise source in the low-frequency range, representing the most potent contributor across the entire frequency domain. This observation underscores the inadequacy of the melamine panels on the diffuser side in mitigating the back-propagation of noise. Second, in the 300 Hz to 1000 Hz range, Figure 5.19b, where the noise sources extend beyond the black lines that signify the wind tunnel ceiling and floor, are patterns indicative of reflections present in the test section and shows that the test section walls might be the dominant noise source in this frequency regime. When sound waves interact with reflective surfaces, such as the walls, ceiling, or the wind tunnel floor, they produce mirror-image sources that appear as real noise sources in the beamforming map and potentially percieved to be located outside the test section. This can also be attributed to the insufficiency of the acoustic lining in reducing wall reflections. Lastly, Figure 5.20 shows the tunnel inlet is identified as a noise source at the higher end of the dominant noise spectrum (600-100Hz). The inlet is not lined with melamine or any other acoustic absorbent materials, and this source could also be linked to the rotation of the tunnel fans.

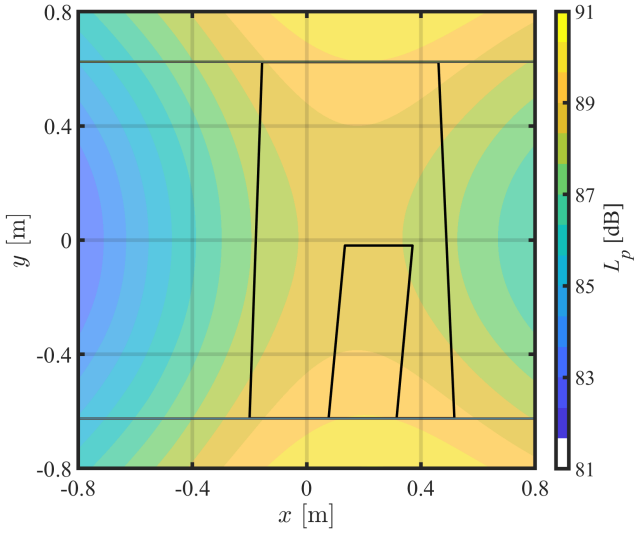

Figure 5.21: FW-H Beamforming (f = [200,1000] Hz)

Figure 5.21 illustrates the impact of excluding the diffuser and inlet from the numerical model. The numerical results indicate that, in the low-frequency range, the outlet or inlet has no significant effect on the noise prediction. However, since the noise sources extend beyond the tunnel walls, as previously discussed, this may suggest the presence of mirror sources caused by wall reflections. Although the tunnel walls are not directly sampled as noise sources, the noise emitted by the strut-braced wing—primarily junction noise in the context of the FW-H analogy—is reflected off the walls and subsequently reaches the array.

Going back to Figure 5.19, the ineffectiveness of the melamine panels in adequately dampening noise in the diffuser and mitigating wall reflections raises questions regarding the performance of the foam. [5] provides the reflection coefficient of the melamine foam as follows:

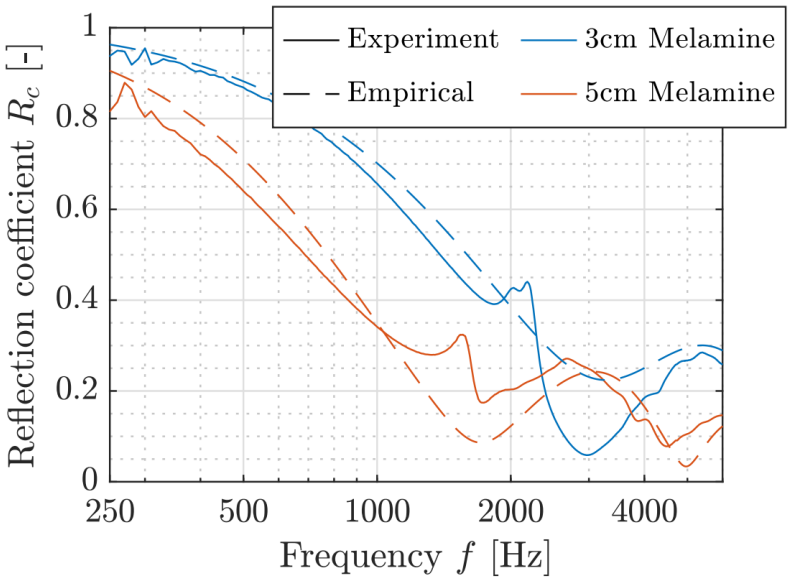

Figure 5.22: Reflection Coefficient of Melamine Foam [5]

Figure 5.22 presents the reflection coefficient of the melamine foam. Ideally, the acoustic foam should exhibit a reflection coefficient close to zero, indicating that most of the incident sound energy is absorbed, thereby minimizing reflections. Conversely, a reflection coefficient close to one would indicate that all incident sound energy is reflected, with none being transmitted into the foam. Figure 5.22 shows that the melamine foam is highly reflective in the frequency range dominated by wind tunnel noise (100–1000 Hz). This explains why, despite the presence of acoustic lining, it was not possible to isolate noise sources outside the test section. Additionally, it provides insight into why strut noise was only observed above 2 kHz, as discussed in Section 5.6.2, and why wing noise was detected primarily at higher frequencies rather than in the low-frequency range.

In summary, the beamforming analysis revealed notable discrepancies between the experimental and numerical results. The experimental model identified the strut trailing edge as the dominant noise source, with no significant noise originating from the junction. In contrast, the numerical model detected the junction as the primary noise source, failing to identify the trailing edges of either the wing or the strut as contributors. These discrepancies may be attributed to the errors discussed in Section 3.3.4.

Additionally, attempts to isolate the noise contributions from the wing and strut trailing edges highlighted that the dominant noise source in the sub-1 kHz frequency range originated from the diffuser, tunnel wall reflections, and inlet. Combined with the reflection coefficient data for melamine foam presented in Figure 5.22, this suggests that the acoustic lining may be ineffective in the low-frequency region. The CFD model, which does not account for the diffuser and inlet, did not exhibit these phenomena, further emphasizing the importance of these elements in the experimental setup.

6

Conclusion & Future Work

6.1. Conclusion

The resurgence of interest in strut-braced wings within the aerospace industry underscores the limitations of current CFD software in accurately predicting the unsteady flow phenomena characteristic of a strut-braced wing, particularly in junction regions where complex interactions between the wing and strut occur. Moreover, computational aeroacoustic analysis presents additional challenges, as precise noise generation and propagation predictions are crucial for accurate acoustic characterization. This thesis has demonstrated the practical applications of a LBM solver in addressing the challenges of predicting a model strut-braced wing's aerodynamic and aeroacoustic properties. It has been shown that the LBM solver's capabilities vary significantly between steady-state and unsteady results.

Examining the numerical results, the LBM solver showed varying success in replicating the steady experimental results. The static pressure distribution results showed that the solver reproduced the interference effects of the strut at various spanwise locations. The wake rake results were also in good agreement. The numerical model had a similar velocity deficit distribution to the experimental results; however, it overpredicted the velocity deficit in certain spanwise locations.

There were also parts of the steady state results where the CFD model struggled to reproduce experimental results. Some of these discrepancies could be attributed to simulation setup errors. However, specific issues were also identified in the numerical model. Firstly, though the IR and oil flow results showed good agreement with the Skin friction and LIC images in reproducing the effects of the leading edge horseshoe vortex and the corner vortex wake. However, discrepancies in the boundary layer transition between the numerical model and experimental outcomes were also revealed. At a zero degree angle of attack, transition to a turbulent boundary layer occurred downstream of the transition trips, whereas, in the experimental setup, the transition was induced by the trips. At six degrees, the transition location in the numerical model differed from that in the wind tunnel tests and occurred before the trips.

A second issue with the numerical model was its inability to trigger the VLES turbulence model near the wing's trailing edge or downstream of the trips. By remaining in the Subgrid scale model, the simulation lacked the unsteady flow features that can generate surface pressure fluctuations, which are critical contributors to the noise of a strut-braced wing. Furthermore this issue might have been a source for the discrepencies in the wake rake results as wake dissipation was not being accurately resolved.

Regarding unsteady measurements, the LBM solver demonstrated difficulty in accurately predicting unsteady pressure fluctuations in the junction region. The Taipro MiniP sensors revealed significant deviations between the numerical and experimental spectral densities, particularly in the leading edge horseshoe vortex region. The numerical model indicated a laminar boundary layer, contrasting with the turbulent boundary layer observed in the experimental data. Moreover, OSPL results showed that the CFD model predicted significantly higher acoustic intensity than the experimental model, which directly influenced the perceived sound strength in the junction region. The numerical simulation overpredicted

pressure fluctuations near the horseshoe vortex and corner separation, leading the beamforming analysis to identify the junction as a primary acoustic source incorrectly. In contrast, the experimental results detected no noise contribution from the junction, identifying the strut trailing edge as the dominant noise source—a feature the numerical model failed to capture.

Several conclusions can also be drawn from the experimental setup. Despite lining the test section and the diffuser with melamine panels, the test section walls and diffuser emerged as the most significant noise sources detected by the microphone array, with the diffuser contributing the most. This noise interference made it challenging to visualize the noise from the wing's trailing edge and junction. Additionally, as discussed in Section 4.1, setup errors during the wind tunnel testing introduced discrepancies between the numerical and experimental cases, which caused limitations for both steady and unsteady measurements.

6.2. Recommendations for Future Work

The LBM model's ability to predict the unsteady effects of junction flow is limited; however, specific recommendations can be made to understand better and mitigate these errors.

Firstly, the beamforming script and the FW-H model can be further developed to reduce numerical errors inherent in the method. Specifically, a tailored Green's function could be introduced, which, as discussed in Section 2.2.4, may eliminate noise sources originating from the test section walls (which are relevant for the CFD model), diffuser, and inlet. These are sources that Section 5.6.3 have shown as significant noise sources in both experimental and, to a lesser extent, numerical results. This would also allow for a larger frequency domain to be analysed, as it will not be dominated by tunnel-induced noise. Which might help better identify the noise of the wing trailing edge.

Furthermore, improvements to the numerical setup are necessary. Further research is required to investigate the reasons behind the failure of the boundary layer to transition despite the presence of transition strips. Additionally, the VLES model did not adequately transition to the unsteady model. While refining the numerical mesh might seem a plausible solution, this would substantially increase computational cost, rendering acoustic analysis less practical. Therefore, exploring alternative methods for triggering the VLES model may be more effective, such as increasing the height of the transition strips to enhance turbulence levels and force the turbulence model to transition, as observed in the junction region. This approach could achieve the desired flow characteristics with minimal additional computational expense.

Additionally, the absence of key physical features in the CFD simulations - specifically, the acoustic lining in the wind tunnel—introduces further inaccuracies for the direct noise computation and the FW-H analogy. The direct noise computations were excluded from the beamforming analysis, as there was no option to isolate the wing and strut as the sampled source (as is possible with the FW-H analogy), and the lack of acoustic lining means the anechoic properties of the wind tunnel test section are not accurately reproduced. Consequently, the test section walls exert a disproportionately large influence on the noise reaching the array (especially in the medium to high frequency regime where the melamine panels were observed to work best). By applying the acoustic lining to the walls, the CFD setup is more in line with the experimental setup, and the direct noise computations can be considered when comparing the CFD and experimental acoustic noise. However, as long as the inlet and diffuser function as noise sources in the experimental setup, accurately replicating the acoustic environment of the test section in PowerFLOW remains infeasible.

Finally, [12] discusses the influence of airfoil profiles on the acoustic performance of strut-braced wings, noting that variations in airfoil cross-sections can significantly impact noise generation. Although the current wind tunnel model is designed with a modular strut component, allowing for the insertion of different strut geometries, further investigation into the role of airfoil cross-section on acoustic behaviour is warranted. While [12] highlights the impact of airfoil geometry, the underlying mechanisms remain unexplained, indicating a potential area for future research.

References

[1] L. Bowen A. Çelik and M. Azarpeyvand. “Unsteady aerodynamic response of a NACA0012 in smooth and turbulent flows”. In: *AIAA AVIATION 2020 FORUM*. ”American Institute of Aeronautics and Astronautics Inc. (AIAA)”, June 2020. DOI: 10.2514/6.2020-2600.

[2] A. Septiyan et al. “Analysis of aerodynamic characteristics using the vortex lattice method on twin tail boom unmanned aircraft”. In: *AIP Conference Proceedings* 2226.1 (Apr. 2020), p. 020003. ISSN: 0094-243X. DOI: 10.1063/5.0002337. eprint: https://pubs.aip.org/aip/acp/article-pdf/doi/10.1063/5.0002337/13150176/020003_1_online.pdf. URL: https://doi.org/10.1063/5.0002337.

[3] E. Sticchi et al. “Aerodynamic Noise Prediction of Strut-Braced Wing Aircraft”. English. In: *30th AIAA/CEAS Aeroacoustics Conference (2024)*. 30th AIAA/CEAS Aeroacoustics Conference, 2024. 2024. DOI: 10.2514/6.2024-3012.

[4] H. F. Mourão Bento et al. “Lattice Boltzmann very large eddy simulations of a turbulent flow over covered and uncovered cavities”. In: *Physics of Fluids* 34 (Oct. 2022), p. 105120. DOI: 10.1063/5.0100001.

[5] H. F. Mourão Bento et al. “Wall treatments for aeroacoustic measurements in closed wind tunnel test sections”. English. In: *AIAA AVIATION 2023 Forum*. United States: American Institute of Aeronautics and Astronautics Inc. (AIAA), 2023. DOI: 10.2514/6.2023-4162.

[6] R. Merino-Martínez et al. “A Review of Acoustic Imaging Methods Using Phased Microphone Arrays”. In: *CEAS Aeronautical Journal* 18.4-5 (2019), pp. 444–469. DOI: 10.1177/1475472X19852945. eprint: https://doi.org/10.1177/1475472X19852945. URL: https://doi.org/10.1177/1475472X19852945.

[7] R. Merino-Martínez et al. “Assessment of the accuracy of microphone array methods for aeroacoustic measurements”. In: *Journal of Sound and Vibration* 470 (2020), p. 115176. ISSN: 0022-460X. DOI: https://doi.org/10.1016/j.jsv.2020.115176. URL: https://www.sciencedirect.com/science/article/pii/S0022460X20300079.

[8] R. Merino-Martínezet al. “Integration methods for distributed sound sources”. In: *International Journal of Aeroacoustics* 18.4-5 (2019), pp. 444–469. DOI: 10.1177/1475472X19852945. eprint: https://doi.org/10.1177/1475472X19852945. URL: https://doi.org/10.1177/1475472X19852945.

[9] T. Krüger et al. *The lattice Boltzmann method principles and practice*. Springer International Publishing, 2018.

[10] Y. Dazhi et al. “Viscous flow computations with the method of lattice Boltzmann equation”. In: *Progress in Aerospace Sciences* 39 (2003), pp. 329–367. URL: https://api.semanticscholar.org/CorpusID:53501349.

[11] Y. Ding et al. “Experimental investigation of the flow characteristics and noise generation at the wing–wall junction”. In: *Journal of Aerospace Engineering* 34.5 (Sept. 2021). DOI: 10.1061/(asce)as.1943-5525.0001303.

[12] Y. Ding et al. “Investigation of the mean pressure field in the wing-wall junction region”. In: *International Journal of Heat and Fluid Flow* 94 (2022), p. 108942. ISSN: 0142-727X. DOI: https://doi.org/10.1016/j.ijheatfluidflow.2022.108942. URL: https://www.sciencedirect.com/science/article/pii/S0142727X22000170.

[13] Y. F. Hwang et al. “Comparison of semi-empirical models for turbulent boundary layer wall pressure spectra”. In: *Journal of Sound and Vibration* 319.1 (2009), pp. 199–217. ISSN: 0022-460X. DOI: https://doi.org/10.1016/j.jsv.2008.06.002. URL: https://www.sciencedirect.com/science/article/pii/S0022460X08005506.

[14] J. Fleming et al. “An experimental study of a turbulent wing-body junction and wake flow”. In: *Experiments in Fluids* 14.5 (Apr. 1993), pp. 366–378. DOI: 10.1007/bf00189496.

[15] *ANSYS Fluent User’s Guide*. Section 7.3.2, Using Flow Boundary Conditions. ANSYS, Inc. 2024.

[16] D. Arumuga Perumal and A. K. Dass. “A Review on the development of lattice Boltzmann computation of macro fluid flows and heat transfer”. In: *Alexandria Engineering Journal* 54.4 (2015), pp. 955–971. ISSN: 1110-0168. DOI: https://doi.org/10.1016/j.aej.2015.07.015. URL: https://www.sciencedirect.com/science/article/pii/S1110016815001362.

[17] T. J. Barber. “An Investigation of Strut-Wall Intersection Losses”. In: *Journal of Aircraft* 15.10 (1978), pp. 676–681. DOI: 10.2514/3.58427. eprint: https://doi.org/10.2514/3.58427. URL: https://doi.org/10.2514/3.58427.

[18] A. L. Braslow and E.C. Knox. *Simplified Method for Determination of Critical Height of Distributed Roughness for Boundary-layer Transition at Mach Numbers from 0 to 5*. Technical notes. National Advisory Committee for Aeronautics, 1958. URL: https://books.google.nl/books?id=DtZCAQAAIAAJ.

[19] *CFD Module User’s Guide*. COMSOL Multiphysics® v. 6.2, pp. 75-84. COMSOL AB. Stockholm, Sweden, 2023.

[20] M. Roger D. Casalino and G. Chiocchia. “Analytical and Numerical Methods in Vortex-Body Aeroacoustics”. PhD thesis. s.n., 2002, pp. 141–142.

[21] Y. Ding. “Aerodynamic and Acoustic Characteristics of Wing-Body Junction Flows”. PhD thesis. UNSW Sydney, 2023.

[22] M. Drela. *AVL (Athena Vortex Lattice)*. http://web.mit.edu/drela/Public/web/avl/. 2000.

[23] M. Drela. *MSES Multi-Element Airfoil Design/Analysis Software - Summary*. Tech. rep. Cambridge, MA, USA: Massachusetts Institute of Technology, 1994. URL: http://web.mit.edu/drela/Public/web/mses/mses.pdf.

[24] M. Escudier and T. Atkins. *static-pressure tapping*. 2019. DOI: 10.1093/acref/9780198832102.013.6124. URL: https://www.oxfordreference.com/view/10.1093/acref/9780198832102.001.0001/acref-9780198832102-e-6124.

[25] J. FLEMING, R. SIMPSON, and W. DEVENPORT. “An experimental study of a turbulent wing-body junction and wake flow”. In: *30th Aerospace Sciences Meeting and Exhibit*. Springer, 1992. DOI: 10.2514/6.1992-434. eprint: https://arc.aiaa.org/doi/pdf/10.2514/6.1992-434. URL: https://arc.aiaa.org/doi/abs/10.2514/6.1992-434.

[26] R.C.K. Leung G.C.Y. Lam and S.K. Tang. “Aeroacoustics of duct junction flows merging at different angles”. In: *Journal of Sound and Vibration* 333.18 (2014), pp. 4187–4202. ISSN: 0022-460X. DOI: https://doi.org/10.1016/j.jsv.2014.04.045. URL: https://www.sciencedirect.com/science/article/pii/S0022460X14003319.

[27] J. Guerrero. *Length Scales in Turbulent Flows: From Kolmogorov Scales to Taylor Microscales to Integral Scales. Energy Cascade. Law of the Wall. Near Wall Treatment. Turbulence and CFD Models: Theory and Applications*. Lecture. Genova, Italy. Feb. 2021.

[28] B. K. Hazarika and Rishi S. Raj. *An investigation of the flow characteristics in the blade endwall corner region*. 1987. URL: https://api.semanticscholar.org/CorpusID:107336654.

[29] D. Herrmann. “A Study of the Suitability of PowerFLOW as an Educational Engineering Design Tool for Undergraduate Students.” PhD thesis. University of Stuttgart, 2007.

[30] S. Elaskar L. F. Gutiérrez-Marcantoni and J. P. Tamagno. “The energy equation for modeling reacting flows on RANS, LES and DES approaches”. In: *Revista Facultad De Ingenieria-universidad De Antioquia* (2022). DOI: 10.17533/udea.redin.20220578.

[31] M. Giles M. Drela and W. T. Thompkins. “Newton Solution of Coupled Euler and Boundary-Layer Equations”. In: *Numerical and Physical Aspects of Aerodynamic Flows III*. Ed. by T. Cebeci. New York, NY: Springer New York, 1986, pp. 143–154. ISBN: 978-1-4612-4926-9.

[32] W. Merzkirch and K. Gersten. *Techniques of flow visualization*. AGARD, 1987.

[33] S. Ölçmen and Semih M. “An experimental study of a three-dimensional pressure-driven turbulent boundary layer /”. In: *Journal of Fluid Mechanics* (Jan. 1996).

[34] E. P. Gross P. L. Bhatnagar and M. Krook. “A Model for Collision Processes in Gases. I. Small Amplitude Processes in Charged and Neutral One-Component Systems”. In: *Phys. Rev.* 94 (3 May 1954), pp. 511–525. DOI: 10.1103/PhysRev.94.511. URL: https://link.aps.org/doi/10.1103/PhysRev.94.511.

[35] S. Park and G. C. Lauchle. “Wall pressure fluctuation spectra due to boundary-layer transition”. In: *Journal of Sound and Vibration* 319.3 (2009), pp. 1067–1082. ISSN: 0022-460X. DOI: https://doi.org/10.1016/j.jsv.2008.06.030. URL: https://www.sciencedirect.com/science/article/pii/S0022460X08005956.

[36] B. W. Pomeroy and M. S. Selig. “Design of Airfoils to Mitigate Wake Bursting”. In: *55th AIAA Aerospace Sciences Meeting*. 2017. DOI: 10.2514/6.2017-1210. eprint: https://arc.aiaa.org/doi/pdf/10.2514/6.2017-1210. URL: https://arc.aiaa.org/doi/abs/10.2514/6.2017-1210.

[37] S. B. Pope. *Turbulent Flows*. Cambridge University Press, 2000.

[38] T. Praisner and C. Smith. “The Dynamics of the Horseshoe Vortex and Associated Endwall Heat Transfer—Part I: Temporal Behavior”. In: *Journal of Turbomachinery-transactions of The Asme - J TURBOMACH-T ASME* 128 (Oct. 2006). DOI: 10.1115/1.2185676.

[39] N. van de Wyer R. Zamponi and C. Schram. “An Improved Regularization of the Generelized Inverse Beamforming Applied to a Benchmark Database”. In: *7th Berlin Beamforming Conference* (Mar. 2018), pp. 5–6.

[40] N. van de Wyer R. Zamponi and C. Schram. “Benchmark Assessment of an Improved Regularization Technique for Generalized Inverse Beamforming”. In: *2018 AIAA/CEAS Aeroacoustics Conference*. ”American Institute of Aeronautics and Astronautics Inc. (AIAA)”, June 2018. DOI: 10.2514/6.2018-4106. eprint: https://arc.aiaa.org/doi/pdf/10.2514/6.2018-4106. URL: https://arc.aiaa.org/doi/abs/10.2514/6.2018-4106.

[41] D. Ricot S. Marié and P. Sagaut. “Comparison between lattice Boltzmann method and Navier–Stokes high order schemes for computational aeroacoustics”. In: *Journal of Computational Physics* 228.4 (2009), pp. 1056–1070. ISSN: 0021-9991. DOI: https://doi.org/10.1016/j.jcp.2008.10.021. URL: https://www.sciencedirect.com/science/article/pii/S002199910800538X.

[42] F. Scarano. *Experimental Aerodynamics February 2013 F. Scarano Aerospace Engineering Department*. 2013.

[43] J. Selle. “Study on the effectiveness of turbulator tape on boundary-layer transition”. PhD thesis. University of California at Davis, 1999.

[44] W. Shao and J. Li. “Review of Lattice Boltzmann Method Applied to Computational Aeroacoustics”. In: *Archives of Acoustics* vol. 44.No 2 (2019), pp. 215–238. DOI: 10.24425/aoa.2019.128486. URL: http://journals.pan.pl/Content/112086/PDF/aoa.2019.128486.pdf.

[45] R. L. Simpson. “JUNCTION FLOWS”. In: *Annual Review of Fluid Mechanics* 33.1 (Jan. 2001), pp. 415–443. DOI: 10.1146/annurev.fluid.33.1.415.

[46] P. Spalart. “Detached-Eddy Simulation”. In: *Annual Review of Fluid Mechanics* 41 (Jan. 2009), pp. 181–202. DOI: 10.1146/annurev.fluid.010908.165130.

[47] C. K. W. Tam. “4.2 Group Velocity and Dispersion”. In: *Computational Aeroacoustics - A Wave Number Approach*. Cambridge University Press, 2012. ISBN: 978-0-521-80678-7. URL: https://app.knovel.com/hotlink/khtml/id:kt00UBITK2/computational-aeroacoustics/group-velocity-dispersion.

[48] M. C. Teixeira. “Incorporating Turbulence Models into the Lattice-Boltzmann Method”. In: *International Journal of Modern Physics C* 9.8 (Sept. 1998), pp. 1159–1175. DOI: 10.1142/S0129183198001060.

[49] W. Timmer. “Two-Dimensional Low-Reynolds Number Wind Tunnel Results for Airfoil NACA 0018”. In: *Wind engineering 32(6), 525-537* 32 (Dec. 2008). DOI: 10.1260/030952408787548848.

[50] R. Wagner and V. Nedzelnitsky. “Effect of Power Line Interference on Microphone Calibration Measurements Made at or Near Harmonics of the Power Line Frequency”. In: *Journal of Research of the National Institute of Standards and Technology* 112 (Mar. 2007), p. 107. DOI: 10.6028/jres.112.008.

[51] V. Yakhot and S. A. Orszag. “Renormalization group analysis of turbulence. I. Basic theory”. In: *Journal of scientific computing* 1.1 (1986), pp. 3–51.

A

CATIA Macro User Guide

This appendix chapter provides a user guide for the CATIA macro developed to facilitate the implementation of wing trips. Designed and refined over the course of this thesis, the macro is intended to be a tool that streamlines the creation of boundary layer transition trips that conform on wing surfaces, regardless of variations in shape, sweep, twist, or airfoil section. Its primary objective is to offer an efficient and repeatable workflow for future wing design studies, ensuring the consistent application of transition elements across various aerodynamic configurations. The macro was developed using the CATIA 3DEXPERIENCE R2024 platform.

A.1. Drawing a Spline on a Wing Surface at a Specified Chordwise Location

To construct a spline on the wing surface at a specified chordwise percentage, the process begins with a wing geometry as below.

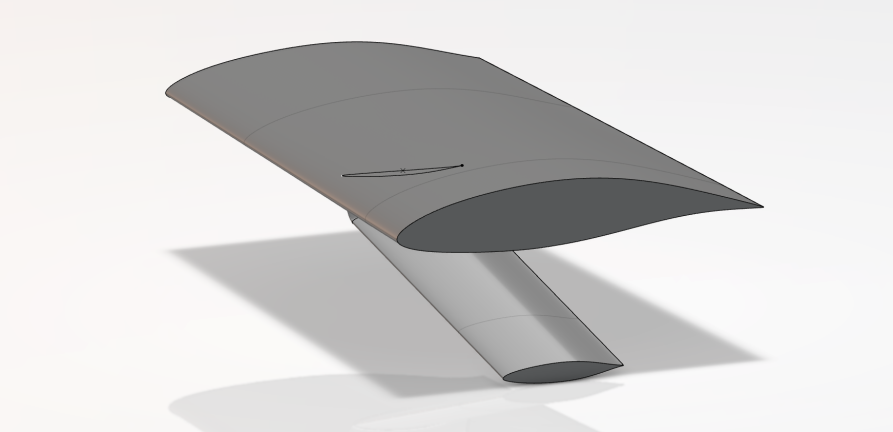

Figure A.1: Initial Wing

The process starts using the Part Design toolbox. The first step involves creating the chord line, a straight line that intersects both the leading and trailing edges of the wing. To accomplish this, points must be defined at each edge. However, in cases where the trailing edge is thick, it is necessary to define a midpoint at the center of the trailing edge using the ”Make Point” tool, as illustrated below.

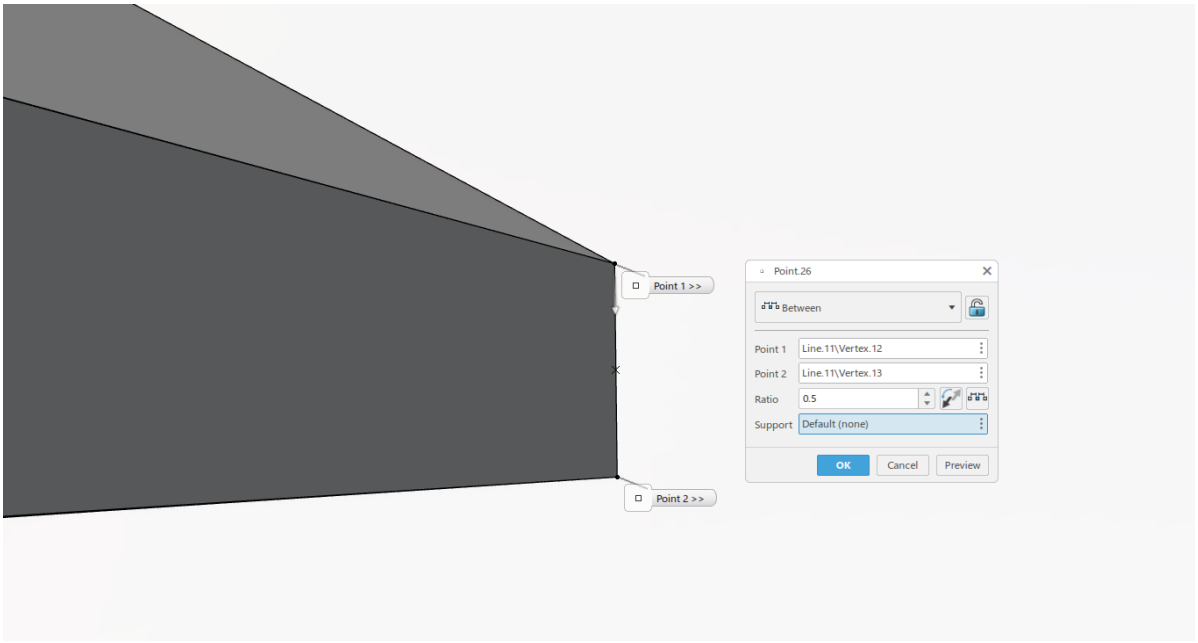

Figure A.2: Creating Trailing Edge Midpoint

After defining points on both the leading and trailing edges, the chord line is created by connecting these points, as demonstrated below.

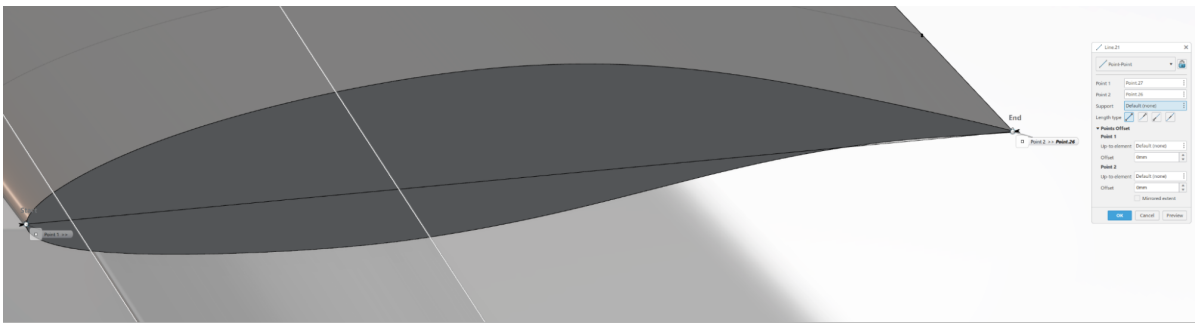

Figure A.3: Creating a Centerpoint for Trailing Edge

Next, a point is defined along the chord line at the desired chordwise location. In this case, the point is placed at 1.617% of the chord length.

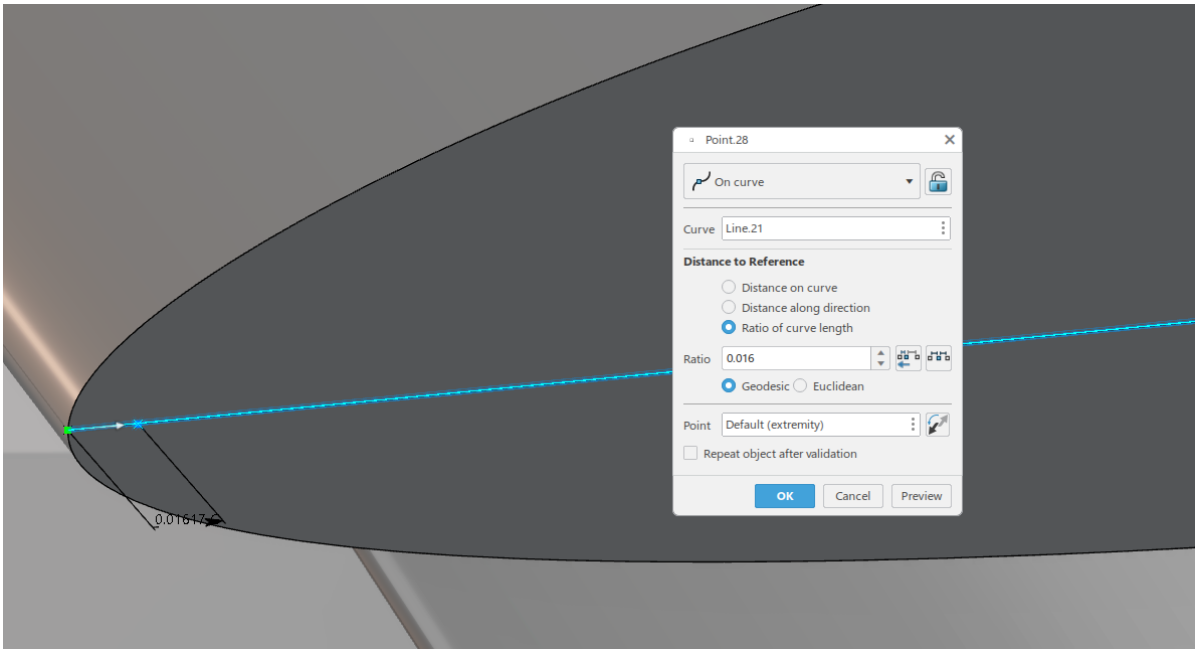

Figure A.4: Drawing Chordline

A line is then defined perpendicular to the chord line, extending until it intersects with the upper wing surface. This process also generates the intersection point between the profile line of the wing root airfoil and the chordline.

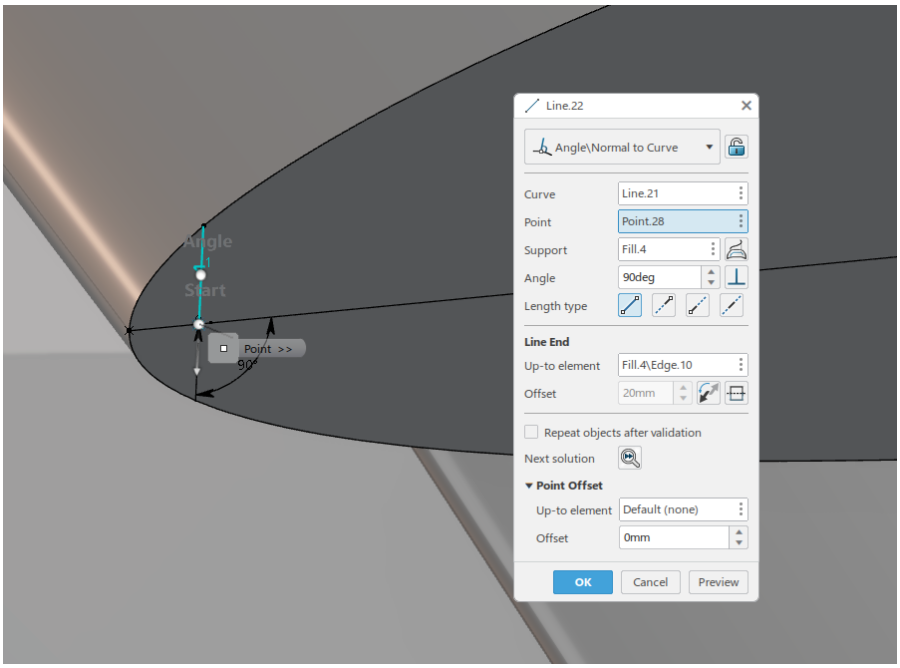

Figure A.5: Extending Chordwise Location to Wing Surface

The same procedure is repeated on the opposite side of the wing, resulting in two points on the wing surface along a given percentage of the chord. Using the ”Spline” command (which is found in the Generative Shape Design Toolbox), a spline is then generated to connect these points, ensuring it conforms to the wing surface by ticking the ”geometry on support”, as illustrated below.

Figure A.6: Creating Spline on Wing Surface

A.2. Applying Macro to Spline

Starting with the previously created spline, the next step involves opening the ZigZag-Mustafa A.1 file using the search bar, which opens a seperate window that houses the macro. Going back to the original window that has the wing and splice, the "Instantiate from Selection" command is then selected. Following this, select the Design Sequence.2 branch within the ZigZag-Mustafa window to initiate the macro.

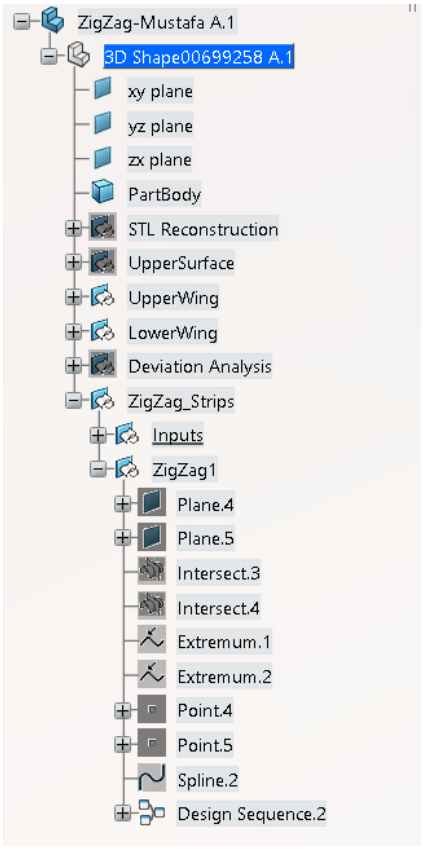

Figure A.7: Design Tree of Macro After Application

After applying the macro on the wing, the tool will request geometric inputs. The spline should be used as the defining curve, and the wing surface should be selected as the supporting surface. Once the design sequence is completed, the trip should become visible. The Inputs section in the design tree allows adjustments to the trip's height, wavelength, and thickness. However, in some cases, the zigzag trip may not protrude outward from the wing surface as intended and may instead recess into

the surface, as illustrated below.

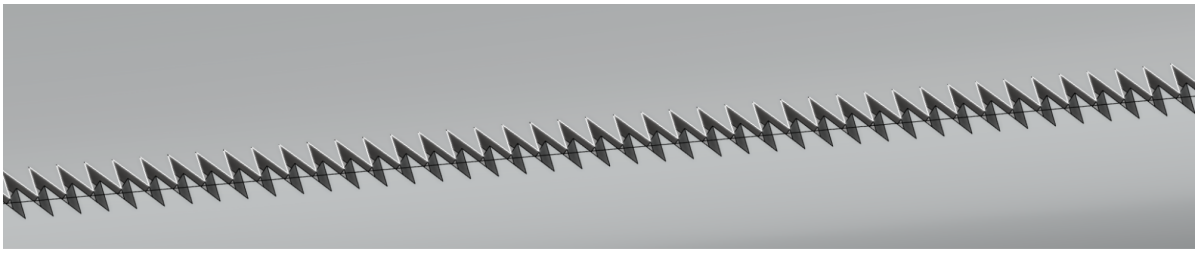

Figure A.8: Recessed Trip

In such cases, navigate to the Inputs section of the design sequence and set the Split Orientation parameter to false. This adjustment ensures the trip protrudes correctly from the wing surface, resulting in the final trip configuration as shown below. From there, the strip can be selected and exported, it will retain its location and orientation when exported.

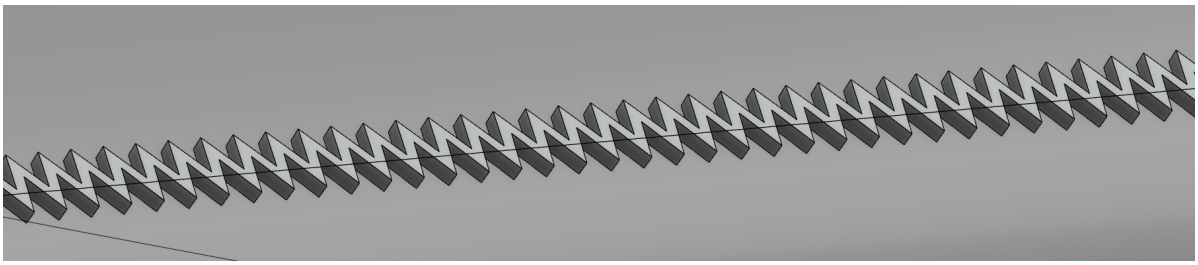

Figure A.9: Final Trip